MOVPE growth and characterization of quantum structures based on III-V semiconductors

by

Shreyashkar Dev Singh

Enrolment No: PHYS03200704010

Raja Ramanna Centre for Advanced Technology,

Indore - 452013

A thesis submitted to the
Board of Studies in Physical Sciences

In partial fulfillment of requirements
For the Degree of
DOCTOR OF PHILOSOPHY
of
HOMI BHABHA NATIONAL INSTITUTE

February 2012

HOMI BHABHA NATIONAL INSTITUTE

Recommendations of the Viva Voce Board

As members of the Viva Voce Board, we certify that we have read the dissertation prepared by **Shreyashkar Dev Singh** entitled **"MOVPE growth and characterization of quantum structures based on III-V semiconductors"** and recommend that it may be accepted as fulfilling the dissertation requirement for the Degree of Doctor of Philosophy.

Chairman	: **Dr. S. M. Oak**	date: 14.9.2012
Member	: **Dr. S. K. Deb**	date : 14.9.2012
Member	: **Dr. L. M. Kukreja**	date : 14.9.2012
Technical Advisor	: **Dr. T. K. Sharma**	date . 14.9.2012
Advisor	: **Dr. Aparna Chakrabarti**	date : 14.9.2012
External Examiner	: **Prof. B. M. Arora**	date : 14.9.2012

Final approval and acceptance of this dissertation is contingent upon the candidate's submission of the final copies of the dissertation to HBNI.

We hereby certify that we have read this dissertation prepared under our direction and recommend that it may be accepted as fulfilling the dissertation requirement.

Date : 14.9.2012

Place : RRCAT, Indore

Aparna Chakrabarti
(guide)

STATEMENT BY AUTHOR

This dissertation has been submitted in partial fulfillment of requirements for an advanced degree at Homi Bhabha National Institute (HBNI) and is deposited in the Library to be made available to borrowers under rules of the HBNI.

Brief quotations from this dissertation are allowable without special permission, provided that accurate acknowledgment of source is made. Requests for permission for extended quotation from or reproduction of this manuscript in whole or in part may be granted by the Competent Authority of HBNI when in his or her judgment the proposed use of the material is in the interests of scholarship. In all other instances, however, permission must be obtained from the author.

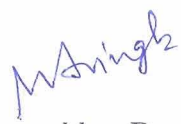

(Shreyashkar Dev Singh)

DECLARATION

I, hereby declare that the investigation presented in the thesis has been carried out by me. The work is original and has not been submitted earlier as a whole or in part for a degree / diploma at this or any other Institution / University.

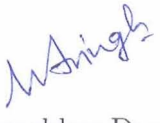

(Shreyashkar Dev Singh)

This thesis is dedicated to

my grandfather

&

my grandmother

ACKNOWLEDGEMENTS

I am thankful to my thesis advisor Dr. Aparna Chakrabarti for her guidance, valuable suggestions and encouragement throughout the course of this work.

I gratefully acknowledge my thesis technical advisor Dr. Tarun Kumar Sharma for his kind guidance, valuable discussions/suggestions, encouragement and motivation throughout the course of this thesis. His keen interest and prompt response towards the scientific problems as well as interpretation of results helped me to complete this thesis in time. I would also like to acknowledge him for teaching me the basics of MOVPE growth and optical characterization techniques without which the thesis could not have been completed.

I am extremely grateful to the members of my Ph.D. advisory committee, Dr. S. M. Oak, Dr. S. K. Deb, and Dr. L. M. Kukreja, for their comments and valuable discussions/suggestions.

Dr. Tapas Ganguli and Dr. V. K. Dixit are acknowledged for stimulating discussions, help in analysis of results and support throughout this work as well as for teaching me the basics of high resolution X-ray diffraction and electrical measurements. The knowledge gained from them has enhanced my understanding towards these techniques, which was needed to complete this thesis. I am also thankful to them for boosting me throughout this work.

It is the support from Shri U. K. Ghosh and Shri Alexander Khakha which helped me to grow the samples by MOVPE technique that are investigated in this thesis. I am thankful to Shri Shailesh Kumar Khamari for his help in making Schottky and Ohmic contacts required for electrical measurements. It is my pleasure to acknowledge Shri Sanjay Porwal for performing optical measurements and Shri Ravi Kumar for performing HRXRD measurements on the samples investigated in this thesis.

I would like to thank Dr. A. K. Srivastava and Shri Puspen Mondal for TEM char-

acterization of the samples and Shri Mahendra Babu for the tedious job of preparing the cross-sectional TEM samples. I am also thankful to Dr. C. Mukharjee for characterizing the samples through AFM technique.

I should mention at this point that I have been given the preference whether it is optical, electrical, HRXRD, TEM or AFM laboratory, which led to completion of the thesis in time. I am extremely grateful to the persons responsible for the respective laboratories.

I acknowledge Dr. Shailendra Kumar, Dr. Suparna Pal and Shri Ravindra Jangir for fruitful discussions and support. I am thankful to Shri Jayaprakash G. and Shri Himanshu Srivastava for encouraging, motivating and keeping me at right track for completion of the thesis.

I am also thankful to all the staff members of Semiconductor Laser Section, Solid State Laser Division and Indus Synchrotron Utilization Division for providing their help by which I have been benefited in one way or the other.

I gratefully acknowledge Prof. K. C. Rustagi, presently at IIT Bombay for teaching me several basics of semiconductor physics at the early stage of my carrier.

My thanks are due to Shri R. B. Tokas and Shri A. Poswal, Applied Spectroscopy Division, BARC who have helped me by sending the soft copies of some of the research papers that were not available at RRCAT.

I would like to thank Dr. J. Jayabalan, Shri M. A. Manekar, Dr. S. Rajmohan, and Shri S. P. Ram for their help in writing the thesis in LaTex software.

Last but not the least I would like to express my sincere gratitude to my parents for their encouragement, never ending love, and affection which provided me the required energy to finish this work. I am thankful to my wife “Parul” for her care, understanding and for sparing her time needed to complete the thesis. I thank my son “Parth” and daughter “Nehal” for providing a cheerful atmosphere at home and

sparing their playing time. I also thank my childhood friends Ashish, Vishal, and Babboo for motivating me all throughout.

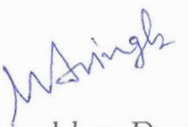

Shreyashkar Dev Singh

CONTENTS

SUMMARY

Quantum structures like quantum wells (QWs), quantum wires, and quantum dots (QDs) are of current interest because opto-electronic devices utilizing these structures have shown better device properties as compared to the bulk structures. For example, 1) QW based diode lasers have lower threshold current density and show room temperature operation [1]; 2) two dimensional electron gas (2DEG) formed at the hetero-junctions is characterized by a very high mobility of electrons and thus is the building block of high speed electronics [2, 3]; 3) infrared photodetectors utilizing QDs show normal incident absorption, lower dark current as well as high temperature operation [4]. Quantum structures can have type-I or type-II band alignment. For type-I QW systems, both type of carriers (electrons and holes) are confined in the QW region, which leads to an increased overlap of electron and hole wave functions and hence these structures show high radiative recombination efficiency. Thus, quantum structures based on type-I band alignment systems such as GaAs/AlGaAs, InAs/GaAs, and InAs/InP are commonly used in the development of efficient light emitting devices like light emitting diodes and laser diodes [5]. On the other hand, for type-II systems like InP/GaAs, GaSb/GaAs, and SiGe/Si, only one type of carrier is confined in the well region, while the other carrier is in the barrier region. These structures suffer from poor overlap of electron and hole wave functions and hence can not efficiently be used as light emitters. This is the reason that the type-II quantum structures are less explored as compared to type-I systems. However, type-II structures exhibit interesting physical phenomenon of Aharonov-

Bohm oscillations [6] in their optical spectrum and also have found applications in photodetectors, optical memory devices, and solar cells [7]. Ultrathin QWs with typical thickness of 1-2 monolayers (MLs) have been studied due to their unique electronic and optical properties leading to their use in the optoelectronic devices [8].

The issue of type-II band alignment for InP/GaAs hetero-structure has been addressed by several groups, where it is understood that the electrons (holes) are confined in the conduction (valance) band of InP (GaAs), respectively [9]. However, there are some interesting signatures of type-II band alignment phenomenon those are normally seen in the photoluminescence (PL) measurements, which seem to be missing for this material combination. For example, the blue shift in PL measurements has been found to increase linearly with the cube root of excitation power which further increases with the QW thickness [7, 10]. Recently, the type-II band alignment between InP and GaAs has again been ascertained on the basis of significantly reduced exciton binding energy for InP/GaAs QDs as observed in magneto PL measurements [11]. However, QD structures grown using Stranski-Krastanov growth technique possess undesirable size, compositional and interfacial inhomogeneities leading to several complications. In view of this, pseudomorphically grown QW structures are more attractive. It is to be noted that, there is no direct evidence of carrier accumulation in InP/GaAs QWs which are normally seen in the capacitance-voltage (C-V) measurements. Carrier distribution characteristics play a very important role in determining the optimum performance of the optoelectronic devices [12]. Temperature dependent C-V measurements have been used to distinguish whether the observed carrier distribution profile is due to the carriers confined in band offset systems or due to the doping inhomogeneities [13]. Band offset at

hetero-junctions is an important physical parameter, which controls the electronic states in the hetero-structures as well as important properties of several optoelectronic devices like semiconductor diode lasers, inter-subband transitions based infrared detectors, and solar cells. C-V is one of the commonly used techniques to measure the band offset at hetero-junctions. However, the band offset for InP/GaAs material system is not yet measured by this technique. Furthermore, temperature dependent PL is not only used to investigate the carrier phonon interaction but also to provide useful information about the luminescence loss mechanism, which is very necessary from the point of view of device operation.

There exist many reports, on the growth and characterization of strained layer superlattice structures based on other material combinations such as InAs/GaAs, InAs/InP etc., showing key fundamental physical properties and interesting applications in several opto-electronic devices [14]. However, detailed studies on the growth and characterization of InP/GaAs based type-II superlattice structures are needed before their possible utilization in the opto-electronic devices. Therefore, in this thesis ultrathin QWs and superlattice structures based on InP/GaAs material combination leading to type-II band alignment are grown by using metal organic vapor phase epitaxy (MOVPE) technique. Their structural, optical and electrical properties are investigated in depth by using cross-sectional transmission electron microscopy (TEM), high resolution X-ray diffraction (HRXRD), atomic force microscopy (AFM), PL, photoreflectance (PR), electroreflectance (ER), surface photovoltage (SPV), and C-V measurements.

Chapter 1 deals with i) a brief introduction about the quantum structures like QWs, superlattices and QDs, ii) a classification of the type-I and type-II band align-

ment systems, iii) a brief description of the interesting properties of type-II systems, iv) a discussion on the temperature dependence of the transition energy of the quantum structures. Following this, we summarize the available results in the literature on InP/GaAs type-II material system and in that light we present the motivation of carrying out the research work leading to the present thesis.

Chapter 2 describes the MOVPE technique used for the growth of InP/GaAs type-II ultrathin QWs and superlattice structures. Several aspects of MOVPE growth technique like growth process, precursors, and safety aspects are discussed in detail. This **Chapter** also provides the information about the basic principle of the characterization techniques such as TEM, HRXRD, AFM, C-V, PL, PR, ER and SPV, which are used to study the structural, electrical and optical properties of the quantum structures. In addition, physical properties of the quantum structures which can be measured using these techniques are also discussed in this **Chapter**.

The issue of type-II band alignment for InP/GaAs heterostructure is addressed in **Chapter 3** by means of simple layer architecture of ultrathin QWs. For such study, InP/GaAs ultrathin QWs of varying well width are grown by using MOVPE technique on nominally (0 0 1) oriented n^+-GaAs substrate. HRXRD and cross-sectional TEM measurements confirm high crystalline and interfacial quality of the grown InP/GaAs ultrathin QWs. Intense PL from the QWs is observed at low temperatures, which red shifts with QW thickness suggesting that the observed PL originates from the recombination of carriers in the ultrathin QWs. In addition, the observed PL is determined to be of excitonic nature for all the ultrathin QWs on the basis of linear relationship between integrated PL intensity and the laser excitation power in the intensity dependent PL measurements. Specific signatures of the radiative re-

combination in QWs, especially the cube root dependence of blue shift in the lowest excitonic transition energy on excitation power, observed in PL measurements indicate that the observed luminescence originates from spatially separated electrons and holes. Such a blue shift is seen to increase with the QW thickness further confirming a type-II band alignment. A direct evidence of electron confinement in the conduction band of InP is provided by the C-V measurements, where a well defined peak in the carrier depth profile for the ultrathin QW having largest well width is observed at around the geometrical position of the QWs and the peak gradually disappears when the thickness of ultrathin QW is reduced.

Investigations on the conduction band offset and quantum states for InP/GaAs type-II ultrathin QWs through temperature dependent C-V measurements are presented in **Chapter 4**. We observe a well-defined peak in the apparent carrier density (ACD) profile for the InP/GaAs ultrathin QWs at low temperatures in the vicinity of QWs. ACD peak value is found to decrease with the reduction in QW thickness. Apart from this, ACD peak value decreases and its width increases with rise in temperature. These observations confirm that peak in ACD profile is related to two dimensional electrons occupying the quantum states formed in the ultrathin QWs. It is also noted that the peak position of ACD profile does not show appreciable shift with temperature. This is attributed to the small temperature dependence of the Debye length, because of the relatively high doping density in the barrier region of InP/GaAs ultrathin QWs. Self-consistent solution of Schrodinger and Poisson equations is used to determine the value of conduction band discontinuity (ΔE_c) for InP/GaAs hetero-junction by simulating the C-V profile. The determined value of ΔE_c for strained InP/GaAs hetero-junction from the C-V measurements is consistent

with the reported value of ΔE_c from x-ray photoemission spectroscopy.

Chapter 5 describes the temperature dependence of transition energies and luminescence loss mechanism from InP/GaAs type-II ultrathin QWs using temperature dependent PL measurements. Near room temperature PL has been observed for 1.43 MLs thick InP/GaAs ultrathin QW. Ground state (GS) transition energy shifts to lower energy with temperature and its temperature dependence has been analysed by using Bose-Einstein empirical relation. Fitting parameters of the Bose-Einstein empirical relation for ultrathin QWs show that the temperature dependence of transition energy is similar to the band gap variation of GaAs barrier layer material. In addition to this, PL quenching mechanism from these ultrathin QWs is investigated by determining the activation energies from Arrhenius-like plot of integrated PL intensity. On the basis of the values of activation energies, it is inferred that the thermal escape of carriers from these ultrathin QWs into the GaAs barrier layer is mainly responsible for the PL quenching with temperature. This fact is also supported by the observation that the PL intensity related to the GaAs barrier layer increases with temperature.

Initial stages of strain relaxation for InP/GaAs type-II QW superlattice structures have been investigated in **Chapter 6**. For this study, several InP/GaAs QW superlattice structures of varying well width, barrier layer thickness and different number of period are grown by using MOVPE technique. Their structural properties and surface morphologies have been investigated through HRXRD, TEM and AFM techniques. Observation of Zeroth (S_0) as well as first order (S_{-1}, S_1) superlattice peaks and interference fringes between them in the rocking curve data from (0 0 4) symmetric reflection for the superlattice structures having relatively

thick GaAs barrier layers (45Å) confirm high crystalline and interfacial quality of the grown superlattice structures. These superlattice structures are fully strained as determined from the reciprocal space map (RSM) of (2 2 4) asymmetric reflection in the HRXRD measurements, thus confirming the pseudomorphic growth of the superlattice structures. On the other hand, for thin GaAs barrier layers (15 Å), interfacial and crystalline qualities of the superlattice samples are poor. This is reflected by relatively large width of S_0 superlattice peak and disappearance of interference fringes around it in the rocking curve measurements of (0 0 4) symmetric reflection. RSM of (2 2 4) asymmetric reflection from these superlattice structures show partial strain relaxation. Further, partially relaxed superlattice structures do not show the presence of dislocations and formation of QD structures as observed from cross-sectional TEM measurements. On the other hand, they show thickness undulations in barrier layers, which degrade their surface morphology. Additionally, a direct correlation has been found between the surface morphology obtained from AFM measurements and the strain status of the superlattice samples determined from the HRXRD experiments, where the strained superlattice samples show smooth surface morphology, while the surfaces of partially relaxed samples show undulations and average surface roughness is found to increase with the QW thickness.

Optical properties of fully strained and partially relaxed InP/GaAs type-II superlattice structures are investigated in the **Chapter 7**. In particular, effect of built-in electric field on the temperature dependence of GS transition energy for highly strained InP/GaAs type-II QW superlattices has been studied by using PR measurements. The built-in electric field in the superlattice structures is determined from the Franz-Keldysh Oscillations (FKOs), which are observed in the above band

gap region of GaAs in the PR spectrum. It has been noted that the built-in electric field in InP/GaAs type-II superlattice structures considerably modifies the temperature dependence of the GS transition energy. For smaller values of electric field, GS transition energy follows the temperature dependence of band gap of GaAs barrier layer. This is expected because GaAs material is present in larger amount than InP in the superlattice structure and thus carriers spend most of their time in the GaAs portion of the superlattice structure. On the other hand, GS transition energy decreases at a faster rate than that of the GaAs material for larger values of built-in electric field. GS excitonic feature in PR spectra red shifts with QW thickness confirming that it originates from the superlattice structure. Broadening parameter is known to have an inhomogeneous and a homogeneous component where the inhomogeneous broadening is independent of temperature and the homogeneous broadening increases with temperature. It is seen that the inhomogeneous broadening dominates from 10-200 K, while above 200 K the temperature dependent homogeneous broadening governs the width of the superlattice feature. Further, it has been found that the width of the superlattice feature in the high temperature region is governed by the scattering of electrons by longitudinal optical phonons present in the InP/GaAs superlattice structure. It has also been noted that the direct modulation of built-in surface electric field is helpful in providing the information about superlattice feature for the case of partially relaxed superlattice strcutures as compared to the indirect manner of modulation of built-in surface electric field. Apart from the strong feature of GaAs barrier layer, a relatively weak feature associated with the superlattice structure is also noted in the room temperature SPS data of the fully strained superlattice samples. This feature gradually becomes stronger as the super-

alttice period is increased and finally it overshadows the GaAs barrier layer feature for the superlattice structure having a superlattice period of 30. A broad feature in the 920-1000 nm wavelength range is observed in the SPS data for the partially relaxed superlattice structures. Room temperature ER data of the partially relaxed superlattice structures show similar features in this wavelength range. Thus, it is confirmed that the broad feature observed in the SPS data is related to the partially relaxed superlattice structures.

Finally the thesis is concluded in **Chapter 8** with the summary of results for ultrathin QWs and superlattice structures based on InP/GaAs type-II system and a brief discussion on the scope for future work in this area.

LIST OF PUBLICATIONS

Journals

Included in the Thesis

[1] Observation of electron confinement in InP/GaAs type-II ultrathin quantum wells.

S. D. Singh, V. K. Dixit, S. Porwal, Ravi Kumar, A. K. Srivastava, Tapas Ganguli, T. K. Sharma, and S. M. Oak.

Appl. Phys. Lett., ***97****, 111912 (2010).*

[2] Temperature dependence of the photoluminescence from InP/GaAs type-II ultrathin quantum wells.

S. D. Singh, S. Porwal, K Alexander, V. K. Dixit, A. K. Srivastava, and S. M. Oak.

J. Phys. D: Appl. Phys, ***43****, 455410 (2010).*

[3] Conduction band offset and quantum states probed by capacitance-voltage measurements for InP/GaAs type-II ultrathin quantum wells.

S. D. Singh, V. K. Dixit, Shailesh K. Khamari, Ravi Kumar, A. K. Srivastava, Tapas Ganguli, and S. M. Oak.

J. Appl. Phys., ***109****, 073702 (2011).*

[4] Effect of built-in electric field on the temperature dependence of transition energy for InP/GaAs type-II superlattices.

S. D. Singh, S. Porwal, A. K. Srivastava, T. K. Sharma, and S. M. Oak.

J. Appl. Phys., ***110****, 123523 (2011).*

[5] Elastic relaxation induced barrier layer thickness undulations in InP/GaAs type-II quantum well superlattice structures.

S. D. Singh, Ravi Kumar, C. Mukherjee, Puspen Mondal, A. K. Srivastava, Tapas Ganguli, T. K. Sharma, and S. M. Oak.

Semicond. Sci. Technol., ***27****, 105031 (2012).*

[6] Signature of optical absorption in highly strained and partially relaxed InP/GaAs type-II quantum well superlattice structures.

S. D. Singh, S. Porwal, T. K. Sharma, and S. M. Oak.

J. Appl. Phys., ***112****, 093505 (2012).*

Not included in the Thesis

[7] Temperature dependence of the lowest excitonic transition for an InAs ultrathin quantum well.

S. D. Singh, S. Porwal, T. K. Sharma, and K. C. Rustagi.

J. Appl. Phys., ***99****, 063517 (2006).*

[8] Spectroscopic investigations of MOVPE-grown InGaAs/GaAs quantum wells with low and high built-in strain.

T. K. Sharma, **S. D. Singh**, S. Porwal, and A. K. Nath

*J. Crystal Growth, **298**, 527 (2007).*

[9] Comparative study on passivation of $GaAs_{0.86}P_{0.14}/Al_{0.6}Ga_{0.4}As$ near-surface quantum well.

Suparna Pal, **S. D. Singh**, S. W. D'Souza, S. R. Barman, and S. M. Oak.

*J. Vac. Sci. Technol. A, **28**, 1319 (2010).*

[10] Determination of band offsets in strained $InAs_xP_{1-x}/InP$ quantum well by capacitance voltage profile and photoluminescence spectroscopy.

V. K. Dixit, **S. D. Singh**, S. Porwal, Ravi Kumar, Tapas Ganguli, A. K. Srivastava, and S. M. Oak.

*J. Appl. Phys., **109**, 083702 (2011).*

In Edited Proceedings

Included in the Thesis

[1] Structural, optical and electrical properties of MOVPE grown InP/GaAs type-II ultrathin quantum well.

S. D. Singh, V. K. Dixit, S. Porwal, Ravi Kumar, Shailesh K. Khamari, A. K. Srivastava, Tapas Ganguli, and S. M. Oak.

International Conference on Physics of Emerging Functional Material (PEFM-10), BARC, Mumbai, AIP Conf. Proc. 1313, 250 (2010).

[2] Quantum states probed by temperature dependence capacitance-voltage measurements for InP/GaAs type-II ultrathin quantum well.

S. D. Singh, V. K. Dixit, Shailesh K. Khamari, Tapas Ganguli, and S. M. Oak.

DAE-Solid State Physics Symposium, AIP Conf. Proc. 1349, 1109 (2011).

Not included in the Thesis

[3] Impact of growth parameters on the structural properties of InP/GaAs type-II quantum dots grown by metal-organic vapour phase epitaxy.

S. D. Singh, T. K. Sharma, C. Mukharjee, and S. M. Oak.

International Workshop on Physics of Semiconductor Devices, IEEE, 04472543 (2007).

[4] Studies on GaAs/AlGaAs based (p and n-type) Quantum Well Infrared Pho-

todetector Structures grown using MOVPE.

V. K. Dixit, **S. D. Singh**, T. K. Sharma, Tapas Ganguli, Ravindra Jangir, Suparna Pal, B. Q. Khattak, A. K. Srivastava, Himanshu Srivastava and S. M. Oak.

International Workshop on Physics of Semiconductor Devices, IEEE, 04472517 (2007).

[5] Blue shift in $GaAs_{0.86}P_{0.14}/Al_{0.6}Ga_{0.4}As$ Near Surface Quantum Well.

Suparna Pal, **S. D. Singh**, S. Porwal, and S. M. Oak.

DAE-Solid State Physics Symposium, AIP Conf. Proc. 1349, 1079 (2011).

In Conference Proceedings

Included in the Thesis

[1] Structural and optical properties of metal organic vapour phase epitaxy grown InP/GaAs type-II ultrathin quantum well.

S. D. Singh, V. K. Dixit, S. Porwal, Ravi Kumar, A. K. Srivastava, Tapas Ganguli, and S. M. Oak.

DAE-BRNS National Laser Symposium, RRCAT, 2010.

LIST OF ABBREVIATIONS

Abbreviations

MOVPE : Metal organic vapour phase epitaxy

MBE : Molecular beam epitaxy

LPE : Liquid phase epitaxy

HRXRD : High resolution X-ray diffraction

TEM : Transmission electron microscopy

AFM : Atomic force microscopy

PL : Photoluminescence

PR : Photoreflectance

ER : Electroreflectance

SPS : Surface photovoltage spectroscopy

CV : Capacitance-voltage

ECV : Electrochemical capacitance-voltage

QW : Quantum well

MQW : Multiple quantum well

QD : Quantum dot

RSM : Reciprocal space map

RLP : Reciprocal lattice point

GS : Ground state

FWHM: Full Width at half maximum

2D : Two dimensional

3D : Three dimensional

FKOs : Franz-Keldysh oscillations

DOS : Density of states

CBM : Conduction band minimum

VBM : Valence band maximum

ML : Monolayer

ACD : Apparent carrier Distribution

FCD : Free carrier distribution

EFA : Envelop function approximation

LO : Longitudinal optical

TMGa : Trimethyl gallium

TMIn : Trimethyl indium

RTA : Rapid thermal annealing

FDM : Finite difference method

FDLL : First derivative of Lorentzian function

LIST OF FIGURES

Figure

LIST OF TABLES

Table

Chapter 1

Introduction

1.1 III-V semiconductors

Most of the III-V based compound semiconductors are potential candidates for light emitting applications predominantly due to their direct band gap nature as compared to naturally occurring elemental semiconductors such as Si and Ge, which have indirect band gap. Direct and indirect band gap nature of the semiconductor materials has been elaborated in Fig. 1.1 through energy versus wave vector ($E - k$) diagram [16]. For the direct band gap semiconductors, both conduction band minimum (CBM) and valence band maximum (VBM) occur at k=0 (Γ point) in the band structure and photon (marked as $h\nu$) is efficiently emitted when electron in the CBM recombine with the hole in VBM as shown in Fig. 1.1(a). Such efficient recombination is possible in the direct band gap semiconductors because both energy and momentum are easily conserved in this process as the momentum of photon is negligible in comparison to that of electrons and holes and thus emission process involves a transition without any change in k value. Therefore, optical transitions for a direct band gap semiconductor have shorter radiative life time (10^{-8} - 10^{-9} sec), which makes them very efficient light emitters. On the other hand, CBM

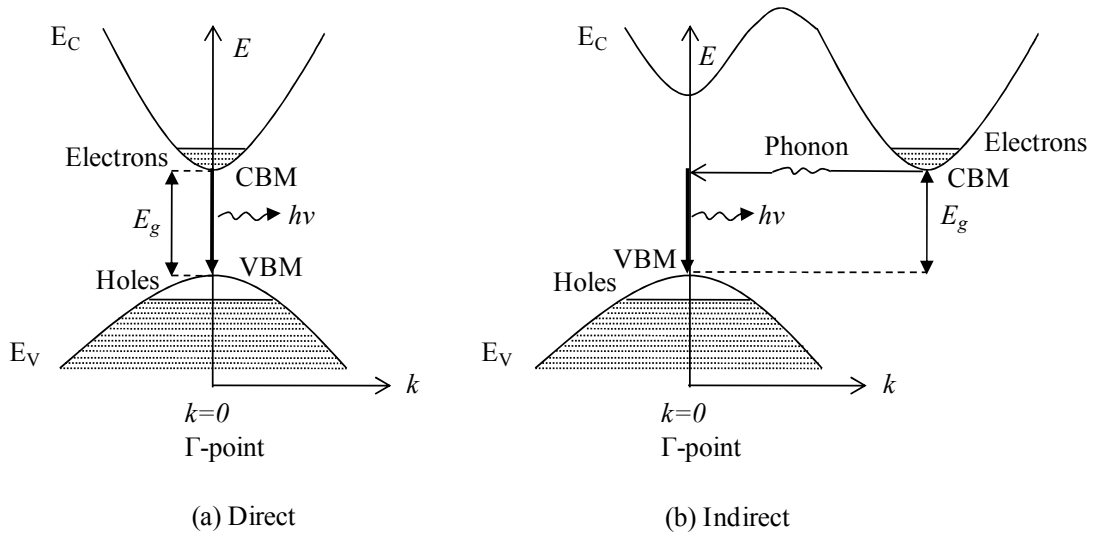

Figure 1.1: $E - k$ diagram for (a) direct (b) indirect band gap semiconductors indicating the light emission process.

and VBM occur at different k values in the $E - k$ diagram for indirect band gap semiconductors as shown in Fig. 1.1(b). Recombination of the electron from CBM to the hole in VBM involves a phonon transfer for the conservation of the momentum, which is a second order process having a relatively small transition probability [16]. This results in the larger radiative life times and thus makes them poor light emitters. III-V compound semiconductor materials are composed of various permutations of group-III elements i.e. B, Ga, Al, In and group-V elements i.e. As, P, Sb, N. Some important binary semiconductors are GaAs, AlAs, InAs, InP, GaP, GaSb, InSb etc. III-V semiconductors generally have Zinc Blende crystal structure [17], which consists of two face centered cubic (fcc) unit cells displaced by one fourth of the lattice constant along the body diagonal as depicted in Fig. 1.2. The lattice has two atom per basis and the coordinates of the two atoms are (000) and $(\frac{a}{4}\frac{a}{4}\frac{a}{4})$, where a is the lattice constant. If the two atoms are same as in case of elemental

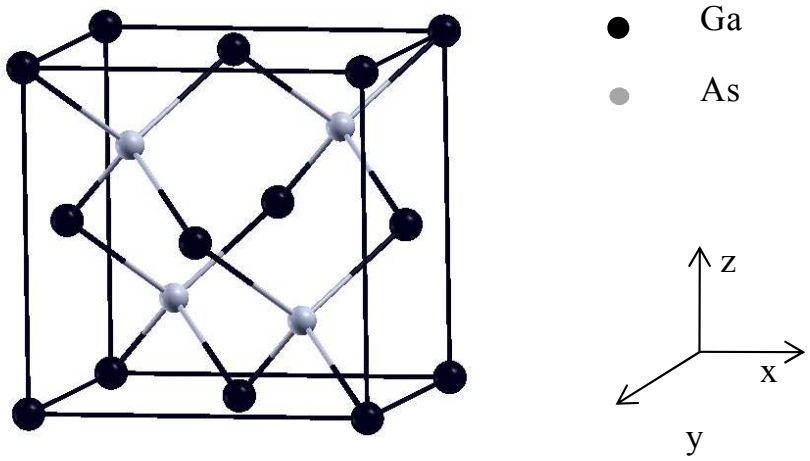

Figure 1.2: Zinc Blende crystal structure of GaAs, where Ga and As sub lattices are displaced by one fourth of lattice parameter along the body diagonal. The underlying Bravais lattice is fcc with a two atom basis, with positions of atoms (000) and $(\frac{a}{4}\frac{a}{4}\frac{a}{4})$, where a is the lattice constant.

semiconductors (Si, Ge), then the resulting crystal structure is called Diamond. It is noted from Fig. 1.2 that each As atom has four Ga atoms as nearest neighbour arranged in a tetrahedron configuration. Figure 1.3 depicts the relationship between lattice constant and band gap of the binary III-V semiconductors at 0 K. Indirect band gap binary meterials are AlP, GaP, and AlAs, while GaAs, InP, InAs, GaSb, and InSb materials have direct band gaps. Wavelength ranges of 0.57-0.62 μm on GaP substrate [18–22], 0.7-1.7 μm on GaAs substrate [23–29], and 1.2-2.2 μm on InP substrate [30–32] have been covered by either the quantum structures of III-V binary semiconductors or their respective ternary/quaternary alloys. These semiconductor materials show large carrier mobility, excellent radiative recombination efficiency, efficient light absorption and easier n as well as p-type doping, which led to their potential use in several optoelectronic devices like light emitting devices, laser diodes, infrared photo detectors, solar cells, and optical memory devices.

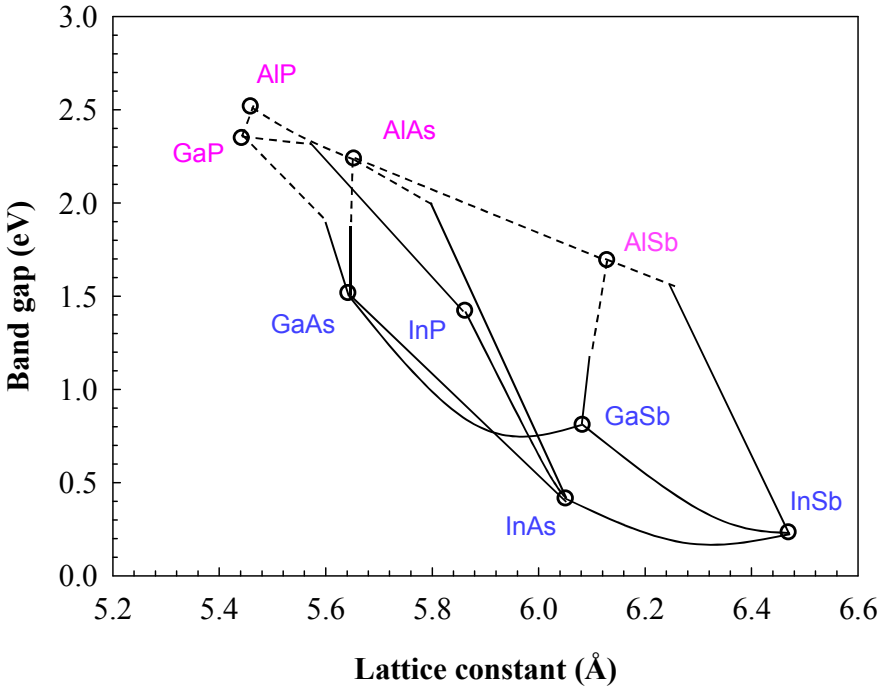

Figure 1.3: Lattice constants and band gaps of binary III-V semiconductors. Range of band gaps achievable by alloy formation is also indicated by dotted (indirect band gap) and solid lines (direct band gap). Values of lattice constants and band gaps are taken at 0 K.

1.2 Quantum structures

Quantum structures are characterized by a parameter known as de-Broglie wavelength of carriers in the material, which is given by the following equation [33]

$$\lambda = \frac{h}{\sqrt{3m^* k_B T}} \tag{1.1}$$

where, h is Plancks constant, m^* is the effective mass of the carrier in material, k_B is the Boltzmann constant and T is the temperature. Values of de-Broglie wavelength of electrons for GaAs and InP materials at room temperature are 24 nm and 22 nm respectively. Quantum structure is formed when thickness of the bulk material is restricted below the de-Broglie wavelength along any one or more of the three directions (x, y, and z) [33]. If the thickness (L_w) of a lower band gap semiconductor

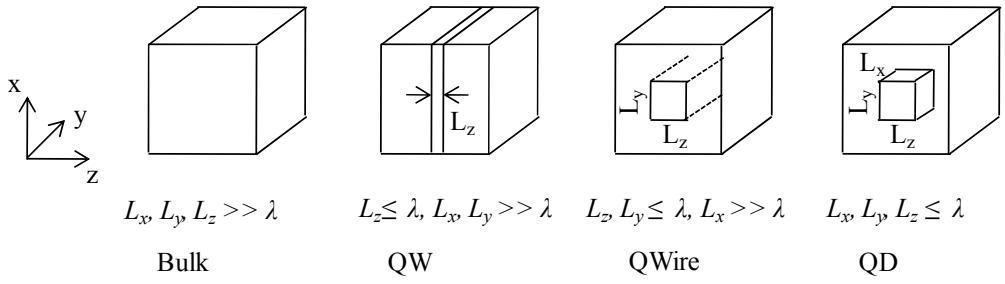

Figure 1.4: Schematic representation of bulk and quantum structures.

material sandwiched between two higher band gap material is restricted below the value of de-Broglie wavelength along one direction (z) as shown in Fig. 1.4, then the resulting quantum structure is called QW. The quantum structure is termed as quantum wire (QWire) or QD depending on whether the thickness of the material is restricted below the de-Broglie wavelength along two directions (z, y) or along all the three directions (x, y, z) as shown in Fig. 1.4. Formation of the QW results in the reduction of degree of freedom for the charge carriers (electrons and holes) in a direction (z) along which the thickness is kept below the de-Broglie wavelength, that is generally the growth direction. Thus, the energy of charge carriers is quantized along the growth direction and its value is determined by the thickness of well material and the height of potential energy barrier presented by the surrounding barrier material as shown in Fig. 1.5(a), where a schematic representation of the quantized energy levels alongwith potential energy barrier has been drawn for a QW structure. Potential energy barrier is different for the different charge carriers. In case of electrons, potential energy barrier height is equal to the conduction band discontinuity (ΔE_C) that confines electrons in the conduction band. Similarly, it is the valence band discontinuity (ΔE_V) which confines holes in the valence band.

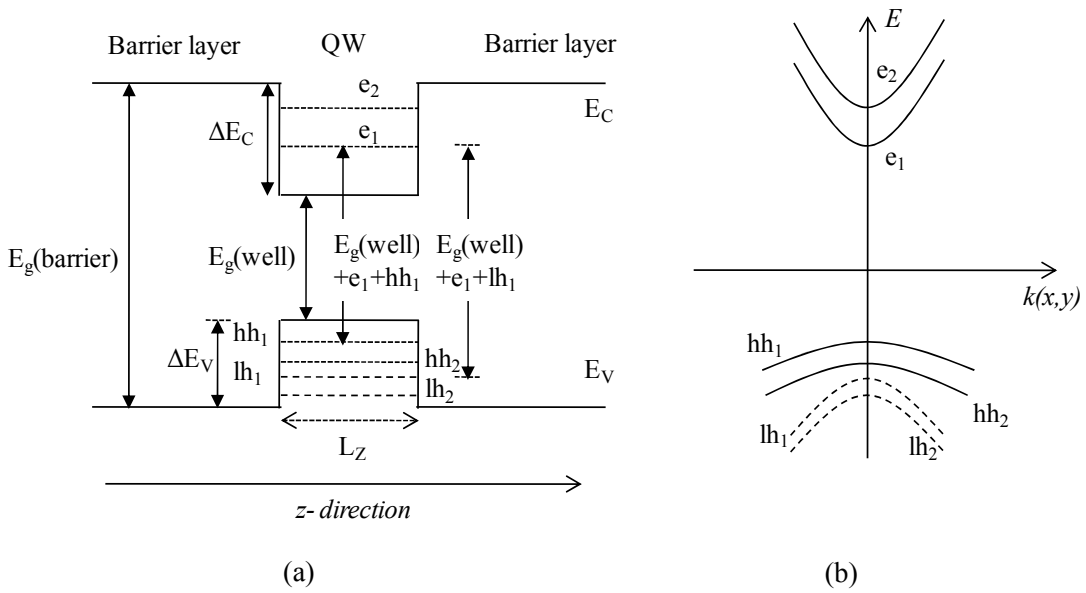

Figure 1.5: (a) Band diagram for a QW structure along with confined energy levels of electrons (e_1, e_2), heavy hole (hh_1, hh_2), and light hole (lh_1, lh_2). Conduction (ΔE_C) and valence (ΔE_V) band discontinuities are also indicated. z is growth direction, which is also the direction of confinement. (b) $E-k$ diagram for a QW structure showing electron and hole sub band dispersion in (x, y) plane.

Energy of confined carriers in the QW is written as [17, 34]

$$E\left(n, k_x, k_y\right) = E_n + \hbar^2/2m^*_{e,h}\left(k_x^2 + k_y^2\right) \tag{1.2}$$

where, E_n is the n^{th} quantized eigen energy value of the z-component of Hamiltonian, $\hbar$ is the Planck's constant, $m^*_{e,h}$ is the effective mass of electron or hole, and k_x, k_y are the components of the crystal momentum along the directions where the motion of electrons and holes is free. Value of E_n is designated by e_1, e_2 for electrons; by hh_1, hh_2 for heavy hole; and by lh_1, lh_2 for light holes. Thus, according to equation 1.2, each confined energy level corresponds to subband in the $E-k$ diagram as shown in Fig. 1.5(b). It is to be noted that there is no allowed energy level below e_1 for electron; above hh_1 for heavy hole; and above lh_1 for light hole in a QW structure. Hence, the

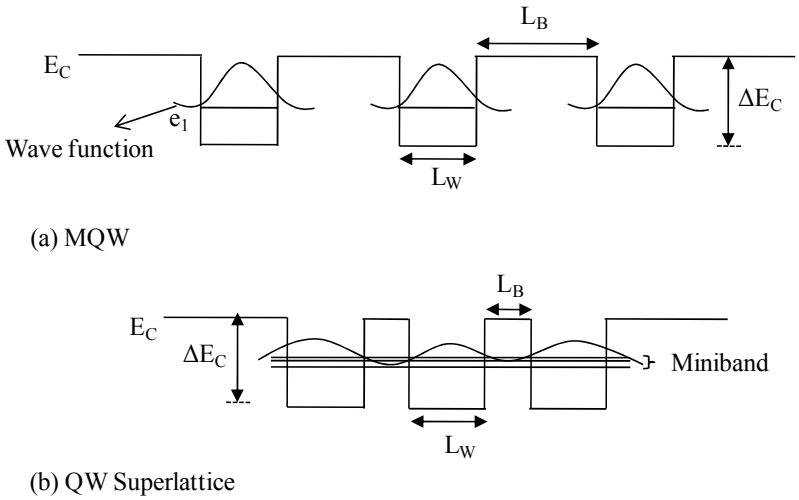

Figure 1.6: Schematic representation of conduction band of (a) multiple quantum well and (b) superlattice structures. L_B and L_W are the thickness of the barrier and quantum well respectively. ΔE_C is the conduction band discontinuity. e_1 is the confined electronic energy level position. Wave function of the electron is shown. Miniband formation in superlattice structure has also been illustrated.

resultant lowest band gap in the QW structure increases from its bulk value (E_g(well)) by an amount equal to $e_1 + hh_1$ as shown in Fig. 1.5(a). In addition, higher energy transitions are also possible in the QW structure as indicated by arrows in Fig. 1.5(a). Another important quantum structure investigated in the literature is a superlattice structure [35], which is an artificially created periodic structure in which a QW structure is repeatedly grown several times as shown schematically in Fig. 1.6. If thickness of the barrier layer between two adjacent QWs is sufficiently large such that the electronic wave functions of individual QWs do not overlap, then the resulting structure is called multiple quantum well (MQW) as shown in Fig. 1.6(a). Energy level of the carrier in each QW is not affected and it has the same value as in case of isolated QW. However, if the barrier thickness between the QWs is relatively thin so that there is sufficient overlap of the electronic wave functions of individual QWs, then

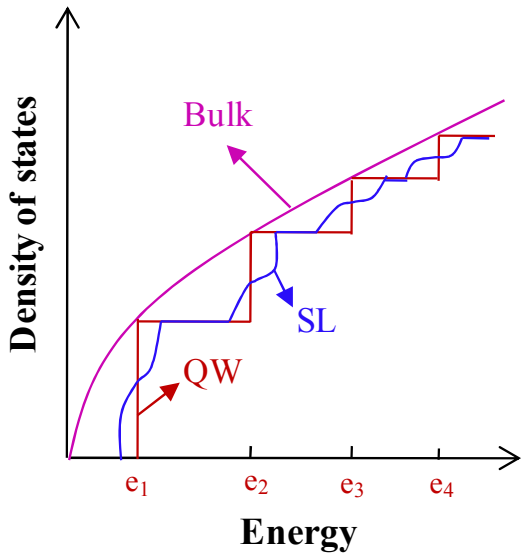

Figure 1.7: Schematic representation of density of states for bulk and quantum structure such as quantum well and superlattice.

the resulting structure is termed as superlattice structure as depicted in Fig. 1.6(b). Thus, the energy level structure of carriers in QWs is not identical to isolated QW but it splits and forms a miniband as illustrated in Fig. 1.6(b). We mentioned above that the eigen energy value of carrier for a quantum structure depends on the barrier height and the size of the quantum structure. Therefore, advantage of a quantum structure over its bulk counterpart is that the emission wavelength from it can be tuned over a wide range of wavelength just by changing the size of the quantum structure and composition of the barrier material. Further, density of states (DOS), defined as the number of electronic states per unit energy range, for the quantum structure is drastically different than that of the bulk structure. Figure 1.7 depicts the schematic representation of the DOS for the bulk as well the quantum structures like QW [17,35,36] and superlattice [35], where it begins at the bottom of conduction band and increases with the square root of energy for the bulk structure. On the

contrary, for a QW structure, it has a step like behavior starting at e_1 with a value of $m_e^*/\pi\hbar^2$ and does not change with energy until a second subband appears at e_2, where it jumps and becomes constant until another subband appears as shown in Fig. 1.7. The sharp step rise of the DOS observed in a QW is smoothed out in the superlattice structure due to the miniband formation [35, 36]. The modified DOS is responsible for the several advantages of the quantum structures over the bulk structures such as carriers are distributed within a small energy range that results in the emission of photons with narrow line width and lower threshold current density for the diode lasers.

It is the development of modern epitaxial growth techniques like molecular beam epitaxy (MBE) [37–39] and metal organic vapor phase epitaxy (MOVPE) [40–43], which provided the precise control over thickness and composition of the semiconductor materials and led to the realization of nano meter scaled objects popularly known as quantum structures. The possibility of artificially tailoring the electronic structure and optoelectronic properties by utilizing MBE and MOVPE epitaxial growth techniques is one important aspect of current research work. Further, there is recent interest on the controlled introduction of highly strained 1-2 monolayer (ML) thick ultrathin layers as an attractive potential for the charge carriers (electrons and holes) in a host material [44–50]. This has shown unique optical and electronic properties as well as potential device applications, which is also the theme of the present thesis. Furthermore, use of quantum structures in optoelectronic devices have provided several revolutionary results as compared to their bulk counterparts, for example; 1) QW based diode lasers have lower threshold current density as well as efficient room temperature operation; 2) two dimensional electrons gas (2DEG) formed at

the hetero-junctions is characterized by a very high mobility of electron which is the building block of high speed electronics [2, 3]; 3) infrared photo detectors utilizing QDs have shown normal incidence light absorption, lower dark current, and higher temperature operation [4]. These infrared photodetectors are used in night vision cameras and thermal imaging devices. Irrespective of numerous technological innovations, intensive research work on the optoelectronic properties of quantum structures is still continuing.

1.3 Band alignment in quantum structures

Optoelectronic properties of quantum structures mainly depend on the band alignment between material systems which are constituting the hetero-junctions. Band alignment, relative position of conduction and valence bands, is determined mostly by electron affinities (χ) of two different semiconductors that are brought together to form the hetero-junction as shown in Fig. 1.8 [17]. Electron affinity for a semiconductor is the energy difference between vacuum level and the conduction band edge. It can lead to different types of band alignment depending upon the value of χ of the semiconductors, which are combined to form the hetero-structure. However, in some cases band alignment based on electron affinity model does not work well, because of subtle charge sharing effects that occur across atoms at the hetero-junction. In view of this, several theories have been developed to predict general trend of the band alignment [17]. But, these theories are quite complex. For commonly known InAs/GaAs hetero-structure, band alignment is such that there is a potential well for electron and hole and both carriers are localized in the lower band gap material (InAs material in this case) as illustrated in Fig. 1.8(a). This

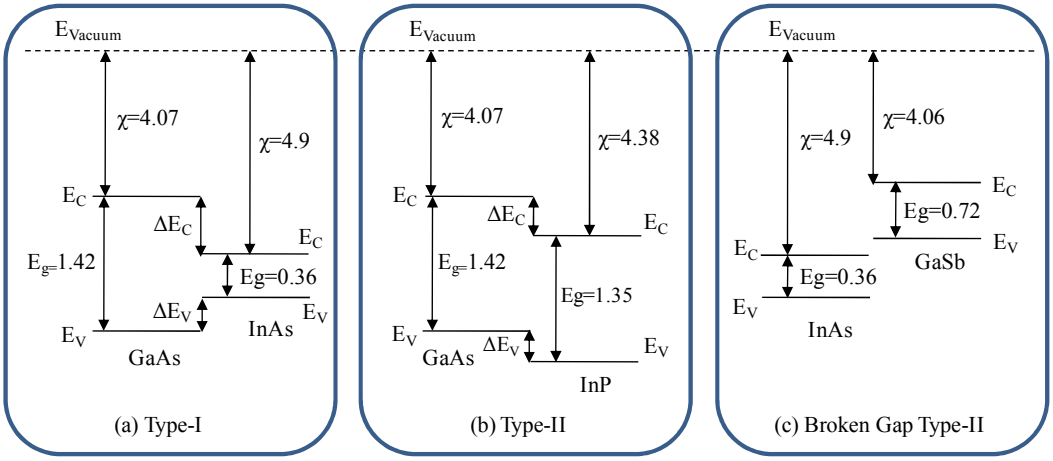

Figure 1.8: Schematic representation of (a) type-I and (b) type-II (c) broken gap type-II band alignment hetero-structures. All values are given in the unit of eV.

leads to better overlap of electron and hole wave functions resulting in the efficient recombination of carriers. Such type of band alignment is designated as type-I and is efficiently used in the light emitters [17]. InAs/InP, InP/AlAs, GaAs/AlGaAs are another examples of type-I band alignment material systems [17]. On the other hand, the band alignment for several hereto-structures is such that there is potential well for one type of carrier inside one material, while at the same time there is a potential barrier for the other type of carrier inside the same material as drawn in Fig. 1.8(b). Such type of band alignment is termed as type-II and this leads to the localization of electrons and holes in different materials. For example, electrons are localized in InP material, while holes are localized in the GaAs material in case of InP/GaAs type-II hetero-junction. Several other material systems which have type-II band alignmnet are GaSb/GaAs, InP/GaP, SiGe/Si [17]. Finally, it is possible to have a situation for type-II band alignment where both conduction and valence bands of one material are well above the conduction band of the other material as shown

in Fig. 1.8(c). This type of band alignment is called broken gap type-II. InAs/GaSb falls in this category [17]. It is to be noted that quantum structures based on type-II band alignment suffer from the poor overlap of electron and hole wave functions due to spatially separated electrons and holes and are not suitable for the light emitters. However, type-II band alignment systems with novel device designs have found potential applications in some optoelectronic devices such as near and mid IR diode lasers [51], photodetectors [7], optical memory devices [52], and solar cells [53] and show some interesting fundamental properties as discussed below.

1.4 Interesting properties of type-II band alignment systems

As mentioned above in the previous section that electrons and holes are localized in different materials in a type-II band alignment hetero-junction and InP/GaAs is one of them. Band alignment for InP/GaAs QW structure has been drawn in Fig. 1.9 for a real situation, where electrons are confined in InP QW region while holes are confined in a triangular potential formed at the InP/GaAs interface in the valence band. The triangular potential is created due to the band bending around the interface region because of the transfer of electrons from GaAs barrier region into the InP QW, which has the lower potential energy for electrons. Hence, transition observed in PL measurements originates from the recombination of spatially separated electrons and holes as indicated by the arrow in Fig. 1.9. It can be noted from the same figure that the transition energy of a type-II band alignment structure can have values lower than the band gap of QW material [54, 55]. On the other hand, transition energy for a type-I band alignment structure is always greater than the band gap of the QW material [54] as can be seen from Fig. 1.5. Thus, the measured

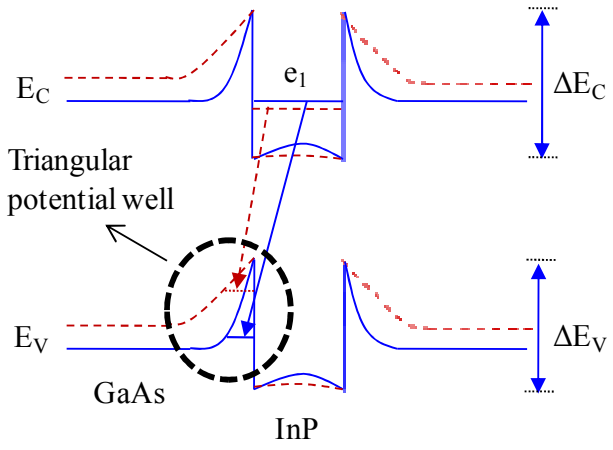

Figure 1.9: Band diagram of a InP/GaAs Type-II quantum well structure. Electron is confined in InP QW with e_1 as the confined energy level. Hole is localized in GaAs barrier and is confined in a triangular potential formed at the InP/GaAs heterojunction in the valence band. Situation for the low and high laser power has been drawn by dotted and solid line respectively. Type-II transition observed in the PL measurements is also indicated by the arrow.

value of transition energy can provide a first indication of type-II transition. Further, it has been noted that the transition energy blue shifts with laser excitation power (P) in PL measurements and follows a cube root behavior ($P^{1/3}$) [56–58], which can be understood in the following way. The electron and hole densities (n, p), generated in a thin layer by a photon flux (I), are given by the following relation [56–58]

$$np = n^2 = \frac{\alpha I \left(L_B + L_W\right)}{\gamma} \tag{1.3}$$

where, α is the absorption coefficient, L_B is the barrier layer thickness, L_W is the QW thickness, and γ is the radiative recombination coefficient. Strongly localized electrons and holes near the InP/GaAs interface form a charged plane and correspondingly produce an approximately triangular potential well with an electric field of strength [56–58]

$$F = \frac{2\pi e n}{\epsilon_0} \propto I^{1/2} \tag{1.4}$$

The ground state energy of hole confined in the triangular potential well formed at the interface region is written as

$$E_0 = CI^{1/3} = C\,(P/A)^{1/3} = C^*\,(P)^{1/3} \tag{1.5}$$

where,

$$C^* = \left(\frac{9\pi}{8}\right)^{2/3}\left(\frac{\hbar^2}{2m_h^*}\right)^{1/3}\left(\frac{2\pi e^2}{\epsilon_0}\right)^{2/3}\left[\alpha\frac{(L_B + L_W)}{\gamma A}\right]^{1/3}, \tag{1.6}$$

P is the laser excitation power and A is area of spot of the laser beam. It is thus noted that the strength of electric field (equation 1.4), steepness of the triangular potential well (Fig. 1.9), increases as the laser power in the PL measurements is increased, which leads to an increase in the ground state energy of holes confined in the triangular potential. Hence, transition energy of a type-II transition in PL measurements blue shifts linearly with the cube root of the laser excitation power [56–58] as evident from the equation 1.5. Furthermore, it has been shown by Baier et al. [10] through theoretical calculations that such blue shift further increases with the QW thickness for type-II QWs. The transition energy of a type-I transition does not show any shift with increase in the laser excitation power. Therefore, a blue shift in transition energy linearly varying with the cube root of laser power which further increases with the QW thickness is considered to be the finger prints of a type-II band alignment phenomenon.

Apart from this, type-II band alignment systems have also shown some fundamental property like topological quantum effect, popularly known as the Aharonov-Bohm effect [59], which manifests the electromagnetic potentials in the quantum domain. It was proposed by Aharonov and Bohm that if a charged particle is allowed to circulate in a confined magnetic field, then there exist effects of the vector potential on

the charged particles moving outside. After circulation, particle wave function acquires a phase which is proportional to the magnetic flux contained within the closed path. Hence, all observable phenomena depend upon the flux ϕ through the excluded region, and are shown to be periodic with period $\phi_0 = hc/e$. This oscillatory characteristic is the signature of Aharonov-Bohm effect. First conclusive experimental evidence of the Aharonov-Bohm effect was reported by Tonomura et al. [60] by using magnetic fields shielded from an electron wave. Investigations and applications of Aharonov-Bohm concepts in condensed matter have been carried out in metals and superconductors. With the advances in growth techniques and lithography process, it is possible to observe the Aharonov-Bohm effect in the magneto transport properties of semiconductor quantum rings within the available experimental range of magnetic fields [61, 62]. Additionally, possibility of the Aharonov-Bohm effect to occur for an exciton placed in a magnetic field was predicted on the basis that the electron and the hole move around with different ringlike trajectories [63]. Following this, Aharonov-Bohm effect for compound semiconductor quantum structures like InGaAs/GaAs patterned quantum rings [64], and InAs/InP quantum tubes [65] has been reported recently. The other possibility of observing the Aharonov-Bohm oscillations (Aharonov-Bohm effect) in the optical spectra of a neutral excitation is in case of type-II QDs [6], where the confinement of one carrier is in the QD region and other carrier is in the barrier region surrounding it that naturally creates a ringlike geometry as schematically shown in Fig. 1.10. In this case, the carrier outside the QD region is bound to one that is confined in the QD through coulomb attraction. Spatial separation of electron and hole in such a structure produces a polarization of exciton and thus leads to the observation of Aharonov-Bohm oscillations

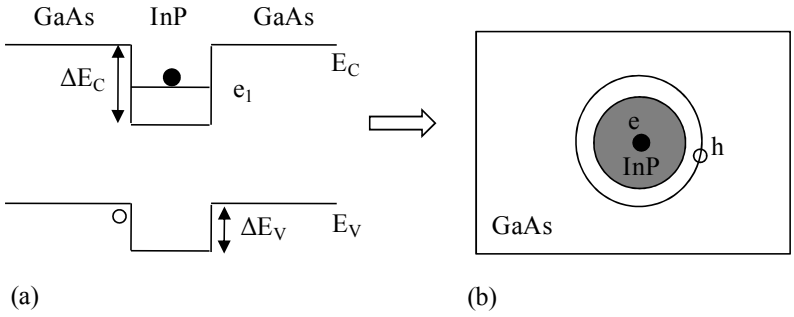

Figure 1.10: (a) Schematic band diagram of a InP/GaAs Type-II QD structure. Electron is confined in InP QD with e_1 as the confined energy level and hole is localized in GaAs barrier indicating the spatial separation of electron and hole. (b) Top view of the QD plane indicating that hole is confined in a ringlike geometry bounded by electron through Coulomb attractive potential.

in the energy of those carriers which are confined in the ringlike orbit around the QD. The Aharonov-Bohm effect in the magneto-optical properties of InP/GaAs [6], ZnTe/ZnSe [66], and Ge/Si [67] type-II QDs have been recently shown.

There are several advantages of type-II systems reported in the literature, which led to their potential application in various optoelectronic devices. Use of type-II system has eliminated the possibility of CHHS Auger process, where conduction to heavy hole (CH) recombination is followed by heavy hole to split off hole (HS) absorption, which is believed to be the main reason of non-radiative decay in mid infrared diode lasers [68, 69]. Additionally, the type-II band alignment introduces larger band discontinuities at the hetero-junctions. InGaAs/GaPAsSb QWs were proposed in 1.3-1.55 μm wavelength region [70]. An improved design consisting of InGaAsN/GaAsSb QWs having strain compensation, strong carrier confinement and large electron-hole wave function overlap has also been reported for 1.55 μm wavelength region [71–74]. For mid infrared wavelength range, InAs/InGaSb QWs

have been found suitable for diode lasers [68,69]. Alternatively, InAsN/GaAsSb QWs on InP substrate have also been reported in similar wavelength range [75]. In addition to this, advantage of type-II QWs have also been realized in III-nitride systems, which are used for the visible diode lasers and light emitting diodes [76, 77]. Conventional type-I InGaN/GaN QWs used for the visible region suffer from the reduced overlap of electron and hole wave functions due to large spontaneous and piezoelectric fields resulting in the poor optical gain from the QW. However, type-II band alignment system based on InGaN/GaAsN and InGaN/GaSbN material combinations with significantly enhanced overlap of electron and hole wave functions has been recently reported, which show improved optical gain and radiative recombination rate [76,78]. Apart from the above mentioned use, type-II systems have also found potential applications in optical memory devices [52], photodetectors [7], and solar cells [53].

1.5 Temperature dependence of the ground state transition energy

Temperature dependence of the band gap (transition energy) for the bulk semiconductors (quantum structures) has been found to provide useful information about the electron-phonon interaction [79]. Most of the semiconductors exhibit decrease in their band gap energy with an increase in temperature [79]. This reduction is attributed to three distinct effects. First of them is related to the thermal expansion of lattice with temperature, which can be obtained experimentally from the pressure dependence of the band gap energy and theoretically by calculating the band structure as a function of lattice constant. The other two terms are related to the electron-phonon interaction and those are the Debye Waller term and self-energy correction term known as Fan's term. Fan [80] presented a calculation of the elec-

tron self-energy correction due to the phonon considering first-order electron-phonon interaction in second order perturbation theory. Brooks and Yu [79] showed that the Debye Waller term stems from the second-order electron-phonon interaction to all higher orders. However, these theoretical calculations are not simple considering the presence of many distinct phonon types with their own dispersions, within any bulk semiconductor, and these couple to the valence and conduction band states through many different mechanisms (for example : deformation potential and lattice polarization) [81]. Hence, temperature dependence of the band gap energy is still usually analyzed by using simple empirical relation given by Varshni [82]

$$E_g(T) = E_g(0) - \frac{\alpha T^2}{\beta + T} \tag{1.7}$$

where, α and β are the constants. $E_g(0)$ is the band gap energy at 0 K. Bose-Einstein empirical relation has also been suggested to describe the temperature dependence of the band gap energy of the semiconductors, which has the following form [83–85]

$$E_g(T) = E_g(0) - a_B \left[1 + \frac{2}{exp(\theta_{BE}/k_B T) - 1}\right] \tag{1.8}$$

where, $E_g(0)$-a_B is the band gap energy at 0 K, a_B is the strength of electron-phonon interaction and θ_{BE} is the mean phonon temperature. It has been found that Varshni and Bose-Einstein empirical relations not only describe the temperature dependence of the band gap of bulk semiconductors but it has also been reported that these relations describe quite well the temperature dependence of the transition energy of the quantum structures like QWs [8], superlattices [86], and QDs [87]. However, it has been found that the temperature dependence of the band gap in low temperature region is described well by Bose-Einstein empirical relation as compared to Varshni relation [88]. Therefore, in this thesis, temperature dependence of the transition

energy of the InP/GaAs based quantum structures has been analyzed by using Bose-Einstein empirical relation. In addition to the change in band gap of semiconductors, line width (Γ) of the optical transitions has been found to increase with temperature. Temperature dependent line width can be written as [89–92]

$$\Gamma(T) = \Gamma_0 + \Gamma_{ac}T + \frac{\Gamma_{ep}}{exp(E_{LO}/k_BT) - 1} \tag{1.9}$$

where, Γ_0 is the temperature independent inhomogeneous broadening, which contains the information about interface roughness, alloy clusterings, well width fluctuations and strain inhomogeneity. Value of this parameter is a prime indication of the crystalline quality of the grown structure and a lower value of Γ_0 means a better crystalline quality of the structure. Γ_{ac} is the strength of electron-acoustic phonon interaction, while Γ_{ep} is the strength of electron-optical phonon interaction. E_{LO} is the longitudinal optical (LO) phonon energy. Last two terms of equation 1.9 are the temperature dependent homogeneous line width, which arise due to electron-phonon interaction. In equation 1.9, the second and third terms give acoustic phonon and optical phonon contribution to the homogeneous line width, respectively. It has been found that interaction of acoustic phonon with electron varies linearly with temperature and is significant in the intermediate temperature range (20-100 K) [89–92]. Line width is dominated by the scattering of electrons with the LO phonons in the high temperature region ($\geq$100 K), where their population density ($[exp(E_{LO}/k_BT) - 1]^{-1}$) increases exponentially with temperature [89–92].

1.6 Motivation of the present thesis

Growth of $In_xGa_{1-x}As/InP$ superlattice structures using MBE technique on (0 0 1) oriented InP substrate was reported by Gershoni et al. [93, 94], which started

work on GaAs/InP based quantum structures. The structure consisted of 10 numbers of $In_xGa_{1-x}As$ QW of width ranging from 20 to 100 Å with InP barrier layers of thickness ∼300-400 Å. They showed a change in band alignment from type-I to type-II in $In_xGa_{1-x}As/InP$ material system as x was changed from x=1 (InAs) to x=0 (GaAs) with type conversion occurring at x=0.20. Their result of change in band alignment was based on the observation of disappearance of excitonic feature in photocurrent measurements as the value of x was changed from x=1 to x=0, which was explained in terms of reduced overlap of wave functions of electrons and holes due to confinement of these carriers in different materials. Then, the growth of single GaAs QWs of 18 and 28 Å well width with InP barrier layers on InP substrate was reported by MOVPE technique and it was shown from the cathodoluminescence that the critical thickness of GaAs on InP is around 30 Å [95]. A change in band alignment from type-II to type-I was shown by studying the pressure dependent PL measurements and the type conversion occurred at pressure around 64-75 kbar depending on the QW thickness [96,97]. Apart from this, Raman, photoluminescence excitation, photoconductivity, and modulated reflectance measurements were also reported on these thin GaAs/InP QWs indicating the presence of heavy hole states in highly strained GaAs/InP QWs [98, 99]. Above mentioned work is related to the quantum structures of GaAs/InP material system grown on InP substrates. However, quantum structures of InP/GaAs material systems were not explored till the year 2001, when growth of InP QDs with GaAs barrier layers on (0 0 1) GaAs substrate was reported through MOVPE technique by Wang et al. [100]. In addition to wetting layer peak at around 830 nm, they have also observed QD related feature at around 986 nm at 10 K in PL measurements. Transition energy from the QD structure

was lower than the band gap of bulk InP, which indicated that the recombination is related to spatially separated electron and hole pair implying type-II band alignment. It was also noted that the transition energy of the QD structure blue shifted with an increase in laser excitation power, which was explained in terms of dipole layer formation caused by spatial separation of electrons confined in InP regions and holes confined in the nearby GaAs region surrounding InP QDs that further supported the type-II nature of InP/GaAs hetero-junction. On the other hand, Nakaema et al. [101] have concluded from micro PL measurements that the observed blue shift of InP QD transition energy with laser excitation power is due to filling of higher energy states rather than the dipole layer formation at the InP/GaAs interface as suggested by Wang et al. [100]. Some fundamental property like Aharonov-Bohm effect was also reported by Ribeiro et al. [6], where they observed oscillatory behavior in their ground state energy in magneto PL measurements. Similar magneto PL measurements showed that exciton g factor for InP/GaAs QDs is independent of the QD transition energy, which was attributed to the weak confinement of holes in type-II InP/GaAs QDs [102]. Thereafter, several studies have been reported dealing with the structural and optical properties of the InP QDs with GaAs barrier layers on GaAs substrate [103–107]. Resonant x-ray scattering was applied to obtain lattice parameter profiles and concentration maps of quaternary alloy regions inside InP/GaAs QDs [107]. It was found that as growth temperature rises, InP QDs present a drastic increase in interdiffusion of substrate atoms, changing from strained to highly Ga interdiffused and nearly strain-free for growth temperature near the In atom desorption limit. Decay time of the optical emission from InP/GaAs QDs has been measured by using time resolved PL measurements in literature [108, 109] and

it was found that the uncapped QDs present relatively long emission decay times (4-14 ns), while QDs covered with a GaAs layer present much shorter lifetimes($\sim$1 ns).

Hence, the issue of type-II band alignment for InP/GaAs hetero-structure has been addressed by several groups as mentioned above, where it is understood that the electrons (holes) are confined in the conduction (valence) band of InP (GaAs), respectively [9, 11, 100, 103]. However, there are some interesting signatures of type-II band alignment phenomenon those are normally seen in the PL measurements, which seem to be missing for this material combination. For example, the blue shift in PL measurements has been found to increase linearly with the cube root of excitation power which further increases with the QW thickness [7, 10]. Recently, the type-II band alignment between InP and GaAs has again been ascertained on the basis of significantly reduced exciton binding energy for InP/GaAs QDs as observed in magneto PL measurements [11]. However, QD structures grown using Stranski-Krastanov growth technique possess undesirable size, compositional and interfacial inhomogeneities leading to several complications. In view of this, pseudomorphically grown QW structures are more attractive. Ultrathin QWs with typical thickness of 1-2 MLs have been studied due to their unique electronic and optical properties leading to their use in the optoelectronic devices [8]. It is noted that, there is no direct evidence of carrier accumulation in InP/GaAs QWs which are normally seen in the C-V measurements. Carrier distribution characteristics play a very important role in determining the optimum performance of the optoelectronic devices [12]. In addition to this, temperature dependent C-V measurements have been used to distinguish whether the observed carrier distribution profile is due to the carriers

confined in band offset systems or due to the doping inhomogeneities [13]. Moreover, band offset at hetero-junctions is an important physical parameter, which controls the electronic states in the hetero-structures as well as important properties of several optoelectronic devices like semiconductor diode lasers, infrared detectors based on inter-subband transitions, and solar cells. Further, C-V is one of the commonly used techniques to measure the band offset at hetero-junctions. However, the band offset for InP/GaAs material system is not yet measured by this technique. Furthermore, temperature dependent PL is not only used to investigate the carrier phonon interaction but also to provide useful information about the luminescence loss mechanism, which is very necessary from the device operation point of view. There exists several reports dealing with the optical properties of InP/GaAs type-II QDs, where the signature of InP/GaAs ultrathin QW, known as a wetting layer in the QD structures, has been observed in the low-temperature PL spectra. However, we do not find any study discussing the optical properties of InP/GaAs ultrathin QWs alone (which means no QDs exist in the same structure). Therefore, a separate study of structural, optical, and electrical properties for InP/GaAs ultrathin QWs is desirable, that can provide help in developing better understanding of the optical properties for the QD structures. In addition, there exist many reports, on the growth and characterization of strained layer superlattice structures based on other material combinations such as InAs/GaAs, InAs/InP etc., showing key fundamental physical properties and interesting applications in several opto-electronic devices [14]. However, detailed studies on the growth and characterization of InP/GaAs based type-II superlattice structures are missing in the literature and these are needed before their possible utilization in the opto-electronic devices. Therefore, in this thesis ultrathin QWs and

superlattice structures based on InP/GaAs material combination leading to type-II band alignment are grown by using MOVPE technique. Their structural, optical and electrical properties are investigated in depth by using cross-sectional transmission electron microscopy (TEM), high resolution X-ray diffraction (HRXRD), atomic force microscopy (AFM), PL, photoreflectance (PR), electroreflectance (ER), surface photovoltage spectroscopy (SPS), and C-V measurements.

Chapter 2

Growth and Characterization techniques

2.1 Introduction

This chapter describes the MOVPE growth process and various characterization techniques that are used to grow and study the structural, optical, and electrical properties of InP/GaAs based type-II ultrathin QWs and superlattice structures. First, a brief discussion about various epitaxial growth techniques is presented, which is followed by a brief description of MOVPE growth technique alongwith its precursors and safety aspects. Thereafter, characterization techniques in which basic principal of the technique alongwith the details of the experimental setup and the properties of the quantum structures that can be measured by using the corresponding technique are described.

2.2 Epitaxial growth techniques

Epitaxial growth of a layer on a substrate corresponds to a well defined relationship between the orientation of the crystal planes of the grown layer and the substrate. This is possible when there exists a matching of symmetry between the

crystal planes of the layer and the substrate. There are several techniques like liquid phase epitaxy (LPE) [110, 111], MBE [37–39], and MOVPE [40–43] that are commonly used for the growth of epitaxial layers on suitable substrates. Each technique has it's own strength and weakness. Experimental setup of LPE, being the oldest among the epitaxial growth techniques, is very simple, where a III-V semiconducting epitaxial layer is grown on a substrate from a supersaturated solution of group-III rich element. High quality III-V epitaxial layers are grown using LPE [111]. However, this technique has some limitations when it comes to the growth of quantum structures like QWs having thicknesses lesser than 10 nm. MBE [40–43] is conceptually very simple technique, where elemental sources are evaporated at a controlled rate onto a heated substrate under ultra high vacuum (ultimate vacuum $\sim 10^{-11}$ mbar) conditions. In the ultra high vacuum environment, growth of an atomic layer can be very well controlled using in-situ monitoring technique like reflection high energy electron diffraction. It is to be noted that quantum size effect was demonstrated firstly by MBE grown QWs. Additionally, highly strained InAs/GaAs ultrathin QWs of very good quality have been reported by using this technique [112, 113]. This technique has produced high quality of arsenide based QWs [112,113], and QDs [114]. However, for phosphide based quantum structures, this technique has shown problems. On the other hand, MOVPE technique has been found successful in producing high quality epitaxial layers as well as quantum structures based on arsenides and phosphides. MOVPE has been very successful in producing device quality QW structures leading to the commercialization of number of devices like light emitting diodes [115], laser diodes [116], photodetectors [117], HEMT and solar cells [53]. InAs/GaAs ultrathin QWs have been grown by using this technique [8, 118–121]. Hence, InP/GaAs based

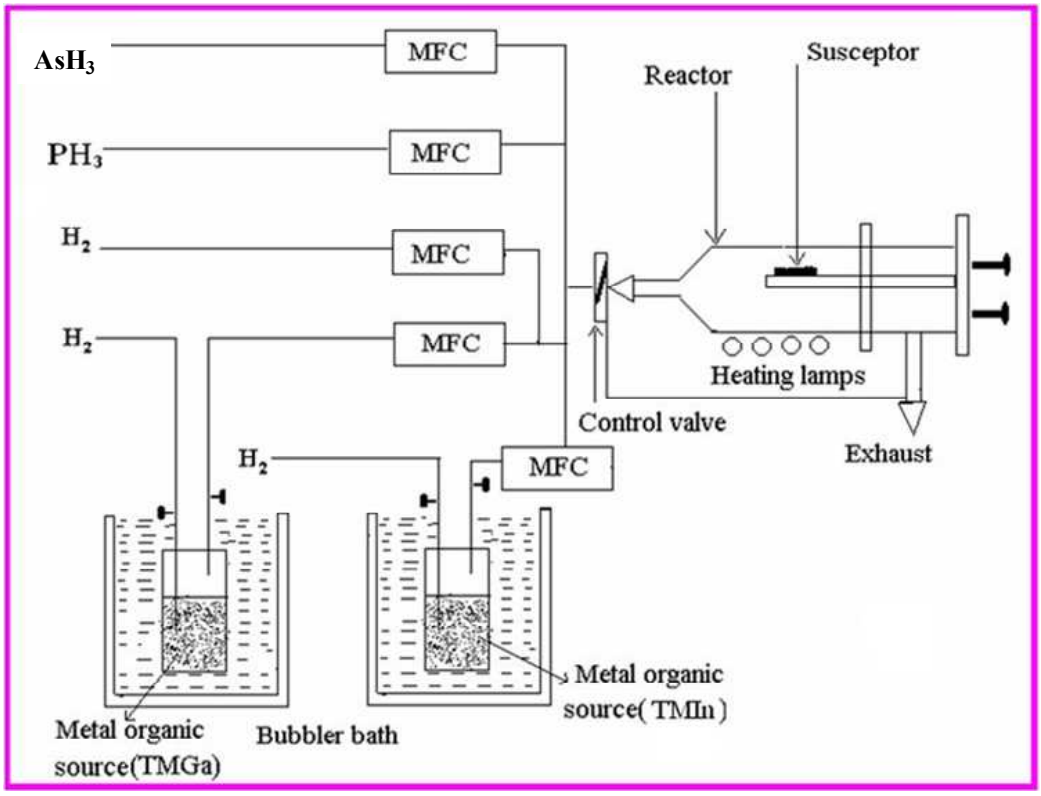

Figure 2.1: Schematic of the MOVPE growth system.

ultrathin QWs and superlattice structures studied in the present thesis are grown by using MOVPE technique. In view of this, a brief description of the technique alongwith its operational principle is given in the next section.

2.2.1 MOVPE growth process

MOVPE has been identified as an important epitaxial crystal growth technique to produce high quality opto-electronic devices based on the quantum structures of III-V semiconductors [40–43]. In addition, MOVPE is also found suitable for the large scale production of opto-electronic devices, thus making it highly suitable for the industrial use. MOVPE growth process of the epitaxial layers is quite complex [43]. In general, the epitaxial layer is formed from the precursor compounds that include

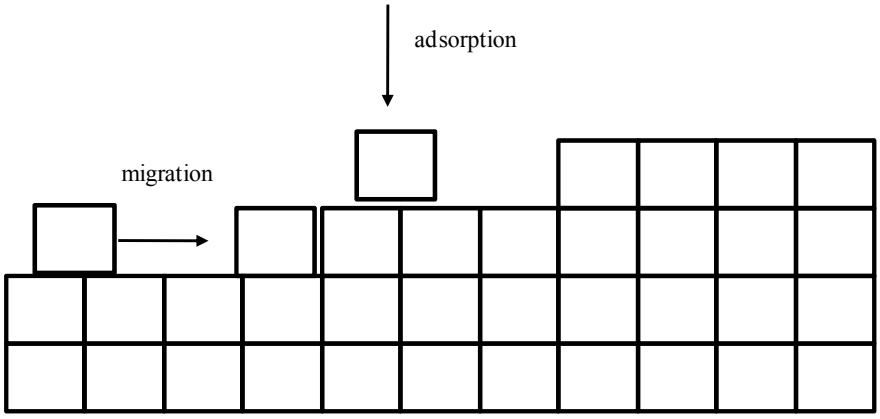

Figure 2.2: Schematic of the step flow growth showing that atoms are adsorbed on the surface and then they migrate to the step edges.

metal organics in the vapour phase and may also include hydrides in form of gases. The precursors are transported into the reactor, generally made of quartz, with the help of a carrier gas (generally hydrogen) as schematically shown in Fig. 2.1. The precursors arrive at the surface of a heated substrate inside a quartz reactor to provide the metal atoms through the pyrolysis that are subsequently adsorbed on the surface of the substrate/growing layer [43]. The adsorbed atoms are mobile and can migrate across the layer surface until they are incorporated into the growing layer. In reality, no macroscopic crystal surface is atomically flat over the entire area and have atomic terraces bounded by the step edges. Under typical MOVPE growth conditions, adsorbed atoms are preferentially incorporated at the step edges as schematically shown in Fig. 2.2. Epitaxial growth is driven by the thermodynamics at the vapour/solid interface. The system strives to reduce the difference in the chemical potentials [43, 122]

$$\Delta\mu = \mu_v - \mu_s \tag{2.1}$$

where, μ_s, and μ_v are the chemical potentials of the solid and vapour respectively. However, other factors are also involved, which are related to the kinetics of surface diffusion, surface reactions and hydrodynamics of mass transport to the growing surface. Three growth regimes [43] have been classified on the basis of the growth temperature (T) as schematically drawn in Fig. 2.3. At low temperatures (T$<550^0$C), the growth rate increases with temperature and is controlled by the kinetics. Decomposition of the group-III precursors is believed to be the growth limiting factor at low temperature. In the temperature range of 550-750^{0}C, mass transport which is the diffusion of the reactants through the boundary layer is the limiting factor. In this growth regime, the growth rate is very weakly dependent on the temperature and only depends on the group-III flow rate. This is the reason why mass transport region is generally used for the epitaxial growth. The growth rate again decreases with temperature in high temperature region (T$>750^0$C), which happens either due to the thermal decomposition of the group-III element from the surface (desorption process) or due to the depletion of reactants from the gas stream. MOVPE growth is performed by keeping the over pressure of group-V element because they are highly volatile [43]. Thus, the growth rate in MOVPE is determined by the supply of group-III elements under normal operating conditions.

The typical precursors for the group-III elements are trimethyl gallium (TMGa), trimethyl aluminum (TMAl), and trimethyl indium (TMIn), while arsine (AsH_3), and phosphine (PH_3) are used for the group-V elements. Following are the requirements for the precursors for MOVPE growth technique [43].

1) Precursors should be sufficiently volatile at room temperature so that it can allow the acceptable growth rates.

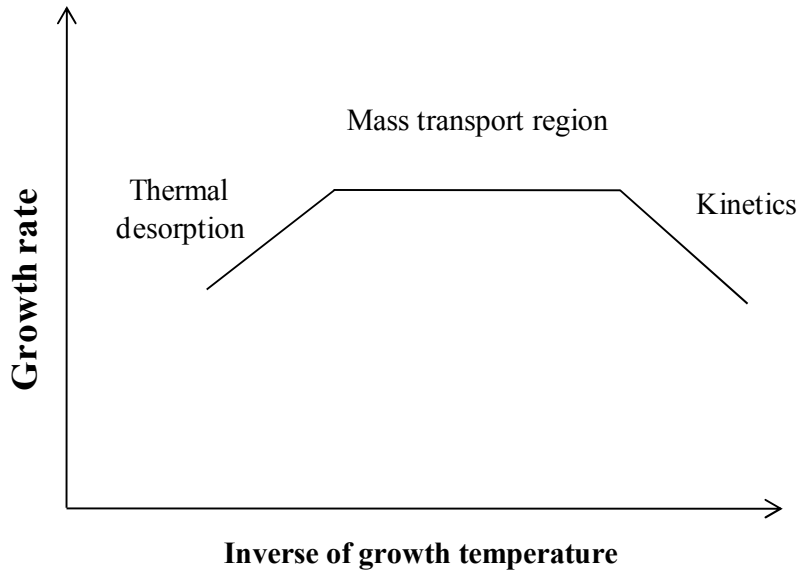

Figure 2.3: Graph between MOVPE growth rate and inverse of growth temperature indicating the three growth regions.

2) They should pyrolyze at low temperature.

3) Precursor molecule should not take part in the parasitic gas reaction that may deplete the nutrients from the vapour.

4) Precursor should be available in very high purity to produce high quality epitaxial layers.

5) Precursor should be less hazardous.

It is known that the precursors (AsH_3 and PH_3) used in the MOVPE growth are highly toxic materials and thus, this technique requires safety precautions in the laboratory. This is the reason why TBAs [123, 124] and TBP [125, 126] are used as an alternative precursor materials in place of AsH_3 and PH_3. The advantage with TBAs and TBP are that they are not only less toxic but also they pyrolyze at lower temperatures as compared to the conventionally used hydride (AsH_3 and PH_3) materials.

2.3 High Resolution X-Ray Diffraction

X-ray diffraction is a powerful characterization tool to determine crystal structure and crystalline quality of the materials [127]. However, resolution of X-ray system is an important issue in characterization of several systems such as 1) in case of single crystals, where full width at half maximum (FWHM) of X-ray rocking curves are of the order of ∼5-10 arcsecs; 2) in case of nearly lattice matched systems such as GaAs/$Al_xGa_{1-x}As$, where the separation of the diffraction angles for (0 0 4) reflection are in the range of ∼370×x arc sec (x is the Al composition in $Al_xGa_{1-x}As$ material), and 3) in case of QWs and superlattice structures, where the period of interference fringes are of the order of several tens of arcsecs. Hence, very high resolution (∼5-10 arc secs) is required in this technique, which is provided by a high resolution X-ray diffraction (HRXRD) system: we have used PANalytical X'PERT diffractometer with CuKα_1 X-rays (λ=1.54056 Å). In this system, a fixed X-ray

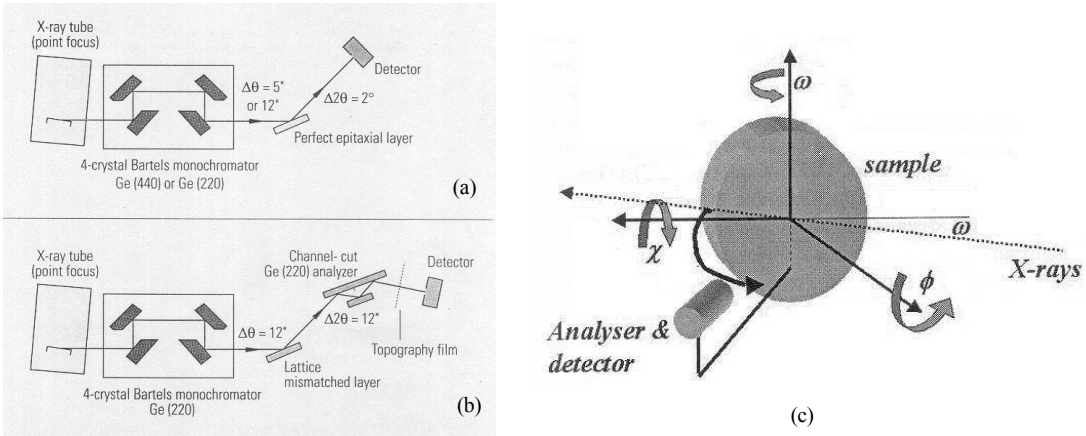

Figure 2.4: (a) Schematic of the rocking curve geometry and (b) triple axis scan geometry alongwith the monochromator details. (c) Schematic of the geometry of the sample mounting illustrating possible angles of rotation for the sample.

tube with a Cu anode is used to generate the X-rays. The beam passes through a four bounce monochromator as schematically shown in Fig. 2.4(a). The resulting beam becomes monochromatic, containing only CuKα_1 X-rays, and is collimated to $\sim$12/$\sim$5 arcsec if we use Ge(2 2 0) or Ge(4 4 0) reflections for monochromatization. The beam falls on the sample and gets diffracted to be detected by the detector. This is the geometry of the rocking curve measurements as shown in Fig. 2.4(a). If there is a three bounce channel cut analyzer in between sample and detector, then the geometry is referred to triple axis geometry as shown in Fig. 2.4(b). This geometry is primarily used for an accurate determination of 2θ values and reciprocal space map (RSM), which is defined later. The sample is mounted vertically on a cradle, known as goniometer, which provides x, y and z linear motions as well as various angles (ω, χ, ϕ, and θ) to the sample as shown in Fig. 2.4(c). Figure 2.5(a) shows the reciprocal lattice space diagram around the reciprocal lattice point (RLP) of (0 0 4) reflection of the substrate, which is oriented along (0 0 1) direction. The directions of ω and $\omega/2\theta$ scans in the reciprocal space are also shown and it is noted that direction of both scans is perpendicular to each other. Thus, a series of ω and $\omega/2\theta$ scans are required to map the reciprocal space. Figure 2.5(a) shows the RLP of the substrate and epitaxial layer for (0 0 4) and (2 2 4) reflections. (0 0 1) and (1 1 0) directions are also indicated, which are perpendicular and parallel to surface of the substrate, respectively. $Q_\perp$ represents the component of the reciprocal lattice vector along (0 0 1) direction and $Q_{||}$ are the in plane component (along (1 1 0) direction) of the reciprocal lattice vector. The components of the reciprocal lattice vector of a RLP are calculated by using the following relations

$$Q_\perp = \frac{2}{\lambda} \sin\theta \cos\left(\omega - \theta\right) \tag{2.2}$$

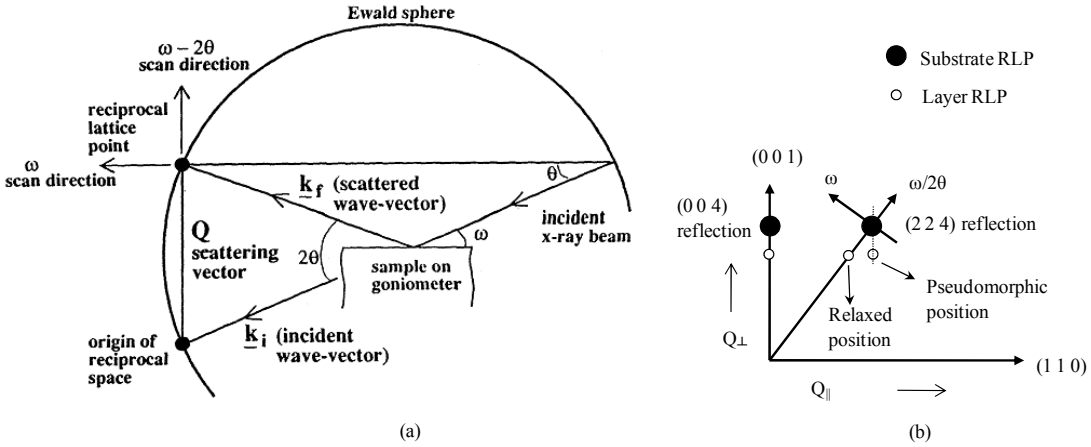

Figure 2.5: (a) Reciprocal lattice space diagram for (0 0 4) reflection alongwith the directions of ω and $\omega/2\theta$ scans. (b) Reciprocal lattice space diagram for (0 0 4) and (2 2 4) reflections of substrate and epitaxial layer. Perpendicular ($Q_\perp$) and parallel ($Q_{||}$) component of the reciprocal lattice vector are also indicated. Strained and relaxed position of the reciprocal lattice point for the epitaxial layer is marked.

and

$$Q_{||} = \frac{2}{\lambda} \sin\theta \sin\left(\omega - \theta\right), \tag{2.3}$$

where, λ is the wavelength of X-rays. The angles ω and θ are defined in Fig. 2.5(a). Thus, RLP for (0 0 4) reflection will have the contribution from perpendicular component of the lattice constant of the epitaxial layer. On the other hand, RLP for (2 2 4) reflection will have contribution from both perpendicular and parallel components of the lattice constant of the epitaxial layer. Hence, information about the strain status of the epitaxial layer is determined from the RLP of the (2 2 4) reflection. If the RLP of substrate and epitaxial layer both falls on a straight line parallel to the $Q_\perp$ axis, then the epitaxial layer is fully strained. If the layer RLP is shifted from this straight line, then it is relaxed as shown in Fig. 2.5. This procedure has been used to determine the strain status of the superlattice structures studied in this

thesis.

2.4 Transmission Electron Microscopy

Transmission Electron Microscopy (TEM) is a powerful tool for material characterization at the scale of lattice spacing owing to very small de-Broglie wavelength of electrons. In this technique, very high energy electrons (about hundreds of kV) are transmitted through a very thin sample (tens of nanometer). In their way through the sample, they get scattered by the sample in several ways. The spatial (imaging) and angular (diffraction) distribution of electron intensity is then displayed on the

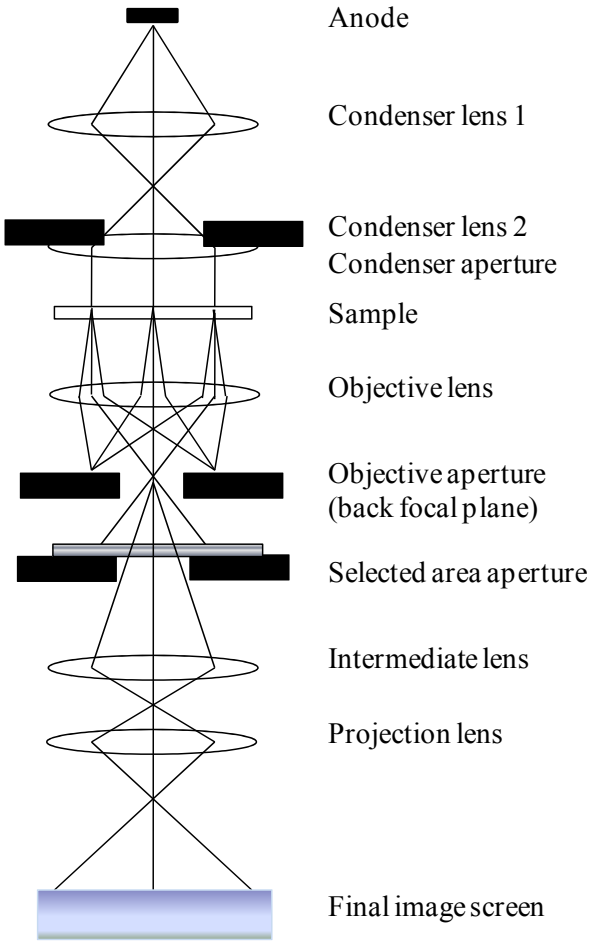

Figure 2.6: Schematic of the ray diagram for a transmission electron microscope in image mode.

screen to get the results.

Block diagram of the TEM microscope is schematically shown in Fig. 2.6. A stream of mono energetic electrons are produced by electron gun, which is focused to a small, thin, coherent beam by the use of condenser lenses 1 and 2. The first lens largely determines the spot size and the general size range of the final spot that strikes the sample. The second lens actually changes the size of the spot on the sample, thus changing it from a wide dispersed spot to a pinpoint beam. The beam is then restricted by the condenser aperture to knock out high angle electrons. The beam strikes the sample and parts of it is transmitted. This transmitted portion is focused by the objective lens into an image. Optional Objective and Selected Area metal apertures can restrict the beam and the Objective aperture enhances the contrast by blocking out high-angle diffracted electrons, while Selected Area aperture enables to examine the periodic diffraction of electrons by the ordered arrangements of atoms in portion of the sample selected in the aperture. The image is passed down the column through the intermediate and projector lenses, being enlarged all the way. The electrons strike the phosphor screen to produce the visible image. The darker areas of the image represent those areas of the sample that fewer electrons are transmitted through (they are thicker or denser). The lighter areas of the image represent those areas of the sample that more electrons are transmitted through (they are thinner or less dense). The information about the sample is obtained by analyzing and inspecting the image produced in different modes. Sample preparation for TEM imaging is a tedious job, because sample thickness should be around tens of nanometer so that electrons can transmit through the sample. Cross-sectional sample preparation scheme is illustrated sequentially in Fig. 2.7. First, samples are

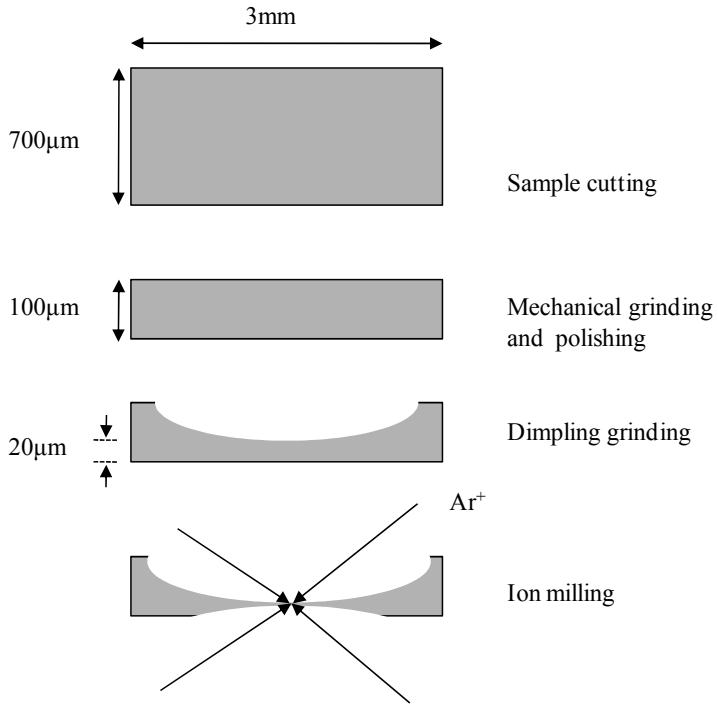

Figure 2.7: Schematic representation of steps used for the TEM sample preparation.

cut in a 3mm×700 μm size. Then, they are mechanically ground and polished so that thickness of the sample is ∼100 μm. Thereafter, sample is placed in the dimpling machine to dimple it upto ∼20 μm and polished with diamond paste. Finally, the sample is placed in the ion milling system to reduce the sample thickness in the nanometer range. TEM instrument used in this thesis work is a Philips CM200 TEM system, which is operated at 200 keV energy.

2.5 Atomic Force Microscopy

Atomic force microscopy (AFM) is a useful scanning probe microscopy technique, which is used to determine the surface morphology of the samples [128]. AFM instrument used in this thesis is a multimode scanning probe microscope (NT-MDT, SOLVER-PRO). The schematic diagram of AFM instrument is depicted in Fig. 2.8.

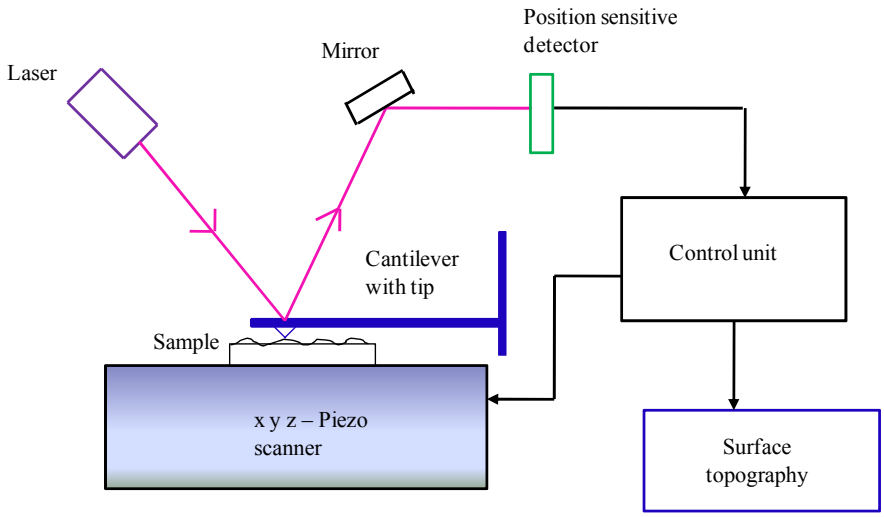

Figure 2.8: Block diagram of the atomic force microscopy setup.

Cantilever is thin enough so that there should be a measurable deflection of the cantilever caused by the interatomic forces between the tip and the sample surface. The deflection is measured by a laser light, which is reflected from the top side of the cantilever and the reflected laser light is detected by the position sensitive detector. The AFM is operated in the feedback mode, where the sample is moved in the vertical direction to keep the deflection of the cantilever constant. The movement of the sample, both in vertical and horizontal directions, is provided by the piezo-electric scanners, which is mounted on the sample stage. Figure 2.9 shows the variation of the interatomic forces with the distance between sample surface and the tip. Attractive Van der waal's forces dominate in the larger distance, while repulsive electrostatic forces dominate in the smaller distances. Operation with net repulsive force is known as contact mode, while operation with an attractive force is known as the non-contact mode in AFM measurements. Silicon cantilever tips having a radius of curvature of 10-40 nm, resonant frequency ∼170-210 kHz and spring constant ∼5.5 N/m are used

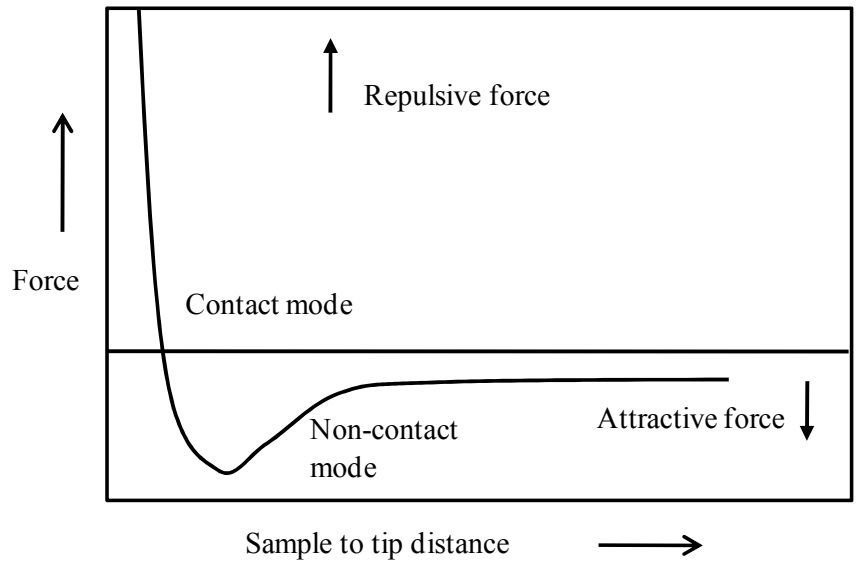

Figure 2.9: Schematic variation of interatomic forces with the distance between tip and sample surface. Region of contact and non-contact mode of operation of AFM is also indicated.

in non-contact mode for the AFM measurement used for the surface topography of the superlattice structures studied in the thesis.

2.6 Photoluminescence spectroscopy

Photoluminescence (PL) is an important but simple technique for the optical characterization of bulk semiconductors and their quantum structures [129]. In this technique, optical response from the semiconductor sample is analyzed by measuring the energy distribution of emitted photon after excitation of the sample by optical means. Experimentally, optical excitation of the semiconductor sample is done by using a pump beam (generally a laser light), which has the photon energy greater than the band gap of the semiconductor sample. Electrons (holes) are created in the conduction (valence) bands of the semiconductor through optical excitation. These excited electrons (holes) then quickly relax to the bottom (top) of the conduction

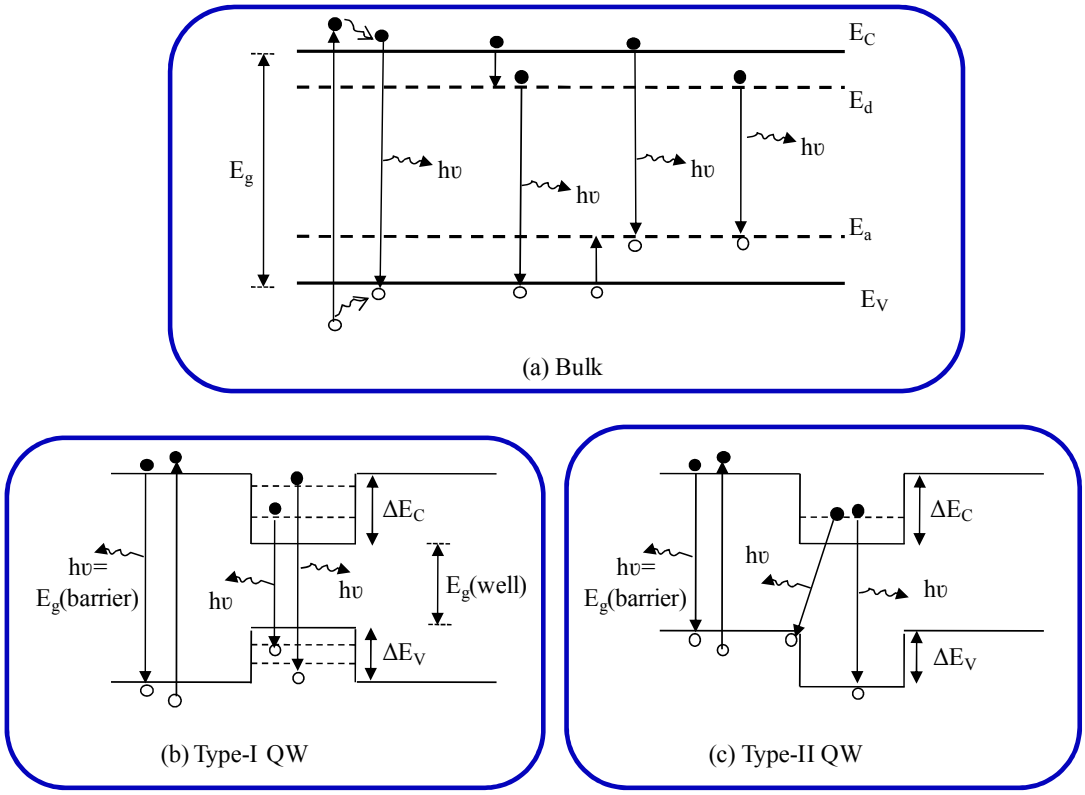

Figure 2.10: Schematic of photoluminescence process (a) bulk semiconductor (b) type-I QW and (c) type-II QW.

(valence) bands as schematically shown in Fig. 2.10(a). Thereafter, various transitions are possible and can be observed in the PL measurements such as; 1) band to band, 2) donor level to valence band, 3) conduction band to acceptor level, and 4) donor to acceptor level. The situation for the quantum structure like type-I and type-II QWs are schematically shown in Fig. 2.10(b) and Fig. 2.10(c), respectively. In type-I QW, electrons (holes) can move to the respective potential well after their relaxation to the conduction (valence) bands. Electrons and holes occupy different confined energy levels in the respective potential wells and in addition to the transitions mentioned for bulk structure, different transitions between confined levels of electrons and holes can be observed in PL experiments of a type-I QW structure.

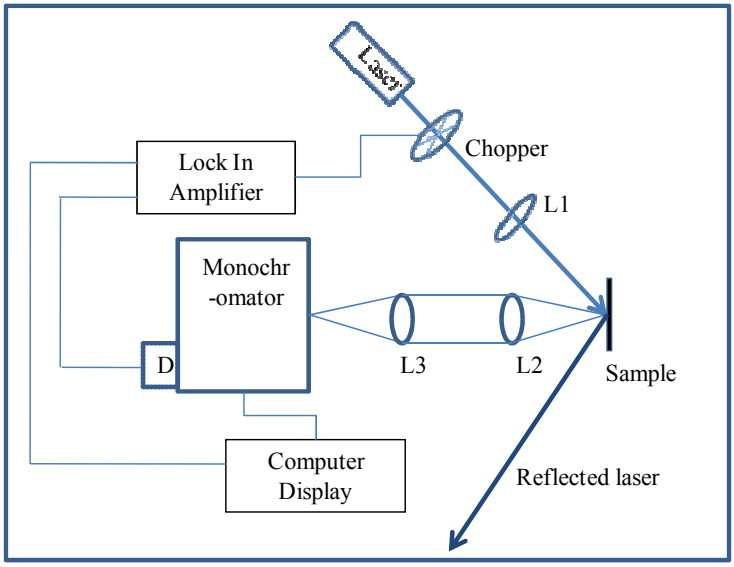

Figure 2.11: Schematic of the photoluminescence experimental setup. L_1, L_2, and L_3 are the focusing lenses and D is the photodetector.

On the other hand, electrons can move to the quantized levels in the potential well formed in the conduction band of a type-II QW as shown in Fig. 2.10(c), while holes are in the barrier region because of the formation of potential barrier for them. Hence, an indirect transition between the electron confined in the QW and the hole in the barrier region alongwith a direct transition between the electron confined in the QW and the free hole in the valence band of QW can be observed. The experimental setup for the PL spectroscopy is schematically shown in Fig. 2.11. PL is excited with a laser light, dispersed by a 1/4 m Sciencetech monochromator and detected by a Si photodiode. PL spectroscopy enables to determine the optical quality along with the band gap (quantized energy levels) of the bulk semiconductor(quantum structures). Usually, this technique provide the information about the lowest energy transition for the quantum structures.

2.7 Photoreflectance spectroscopy

Reflectivity spectra of bulk semiconductors (quantum structures) show broad features corresponding to their band gaps (quantized levels). Therefore, modulation spectroscopy (PR and ER) is generally used to study the band structures, which yields relatively sharp spectral features in their spectrum [130]. This helps in the accurate determination of the band structure of semiconductors (quantum structures). In PR measurements, change in reflectivity alongwith the reflectivity from the bulk semiconductors (quantum structures) is measured. Reflectivity is measured by using a light of variable wavelength known as the probe beam, while change in reflectivity is done by using a laser light having photon energy greater than the band gap of the semiconductor (quantum structure) known as the pump beam. The basic principle behind the PR experiment is schematically shown in Fig. 2.12.

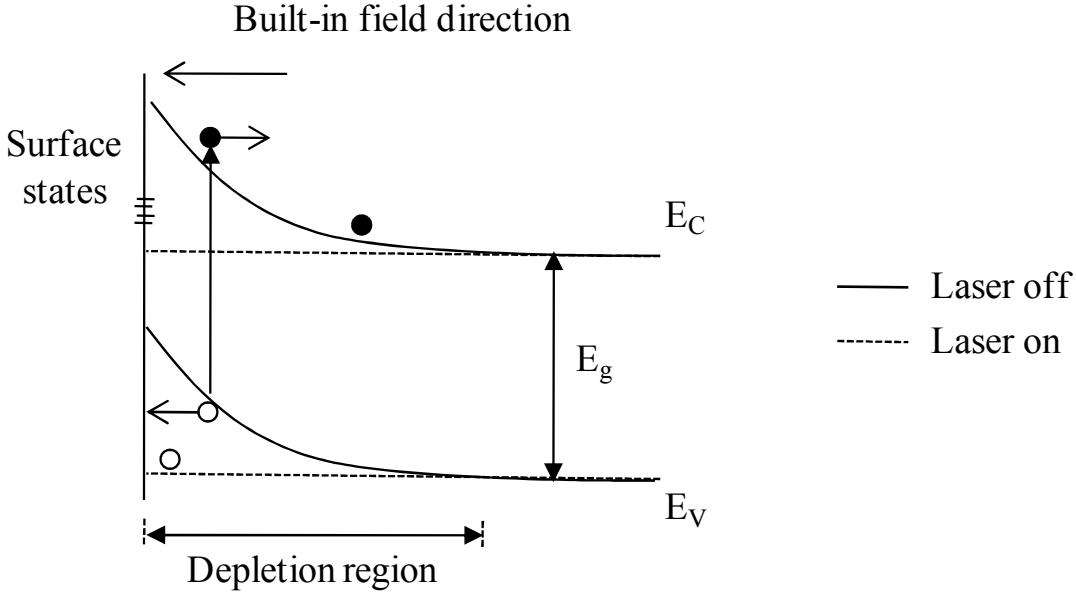

Figure 2.12: Schematic of the basic principle of the photoreflectance technique.

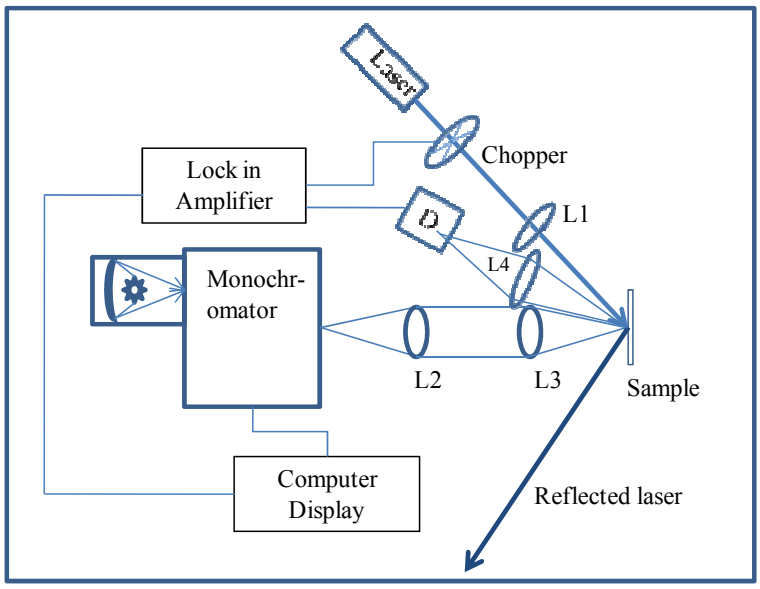

Figure 2.13: Schematic of the photoreflectance experimental setup. L_1, L_2, L_3 and L_4 are the focusing lenses and D is the photodetector.

There exist surface states on the surface of the semiconductors created by the dangling bonds. These surface states capture the free carriers near the surface of the semiconductors, that leads to the pinning of the Fermi level at some position. This causes the band bending at near the surface and creating a depletion region having a built-in surface electric field. When a pump beam falls on the sample surface, electron and hole pairs are generated in the conduction and valence bands by absorbing the laser light. These electrons and holes then get separated by the built-in surface electric field. As a result, one of the carriers move upto the surface and modulates the built-in surface electric field. Hence, periodic generation of electron and hole pairs by the pump beam provides the required periodic modulation of the built-in surface electric field, which changes the reflectivity of the sample that is measured in the PR measurements. The experimental setup for the PR measurements is schematically drawn in Fig. 2.13. Light from a 100 W quartz tungsten halogen (QTH) lamp

dispersed by a 1/4 m Sciencetech monochromator is used as the probe beam. The chopped laser beam of a He-Ne laser (pump beam) is used to modulate the built in surface electric field of the sample. Change in the reflectivity (ΔR) due to the modulation as a function of wavelength of probe beam is measured by using a lock-in amplifier at the chopping frequency of the pump beam (330 Hz). The dc part of the signal from Si photodiode, which is proportional to the reflectivity (R), is also extracted, and the final spectrum ΔR/R is obtained by dividing the ac signal by the dc signal.

PR measurements, being equivalent to absorption spectroscopic measurements, provide the information about the band gap and higher order band gaps of the bulk semiconductors. For the quantum structures, it not only determines the energy of ground state transition but also maps the higher energy transitions.

2.8 Electroreflectance spectroscopy

The basic principle for electroreflectance (ER) technique (being another form of modulation spectroscopy) is similar to the PR technique, where the change in reflectivity alongwith the reflectivity is measured. The only difference between the two measurements is the way by which the built-in surface electric field is modulated. In PR measurements, it is done by using pump beam of a laser light, which is an indirect way. On the other hand in ER measurements [130], it is done in a direct manner by applying an external AC bias to the sample, which modulates the surface electric field. The experimental set up is similar to PR setup except no laser light (pump beam) is used. The built-in surface electric field is modulated in a capacitive geometry under soft contact mode by placing the sample in a specially designed

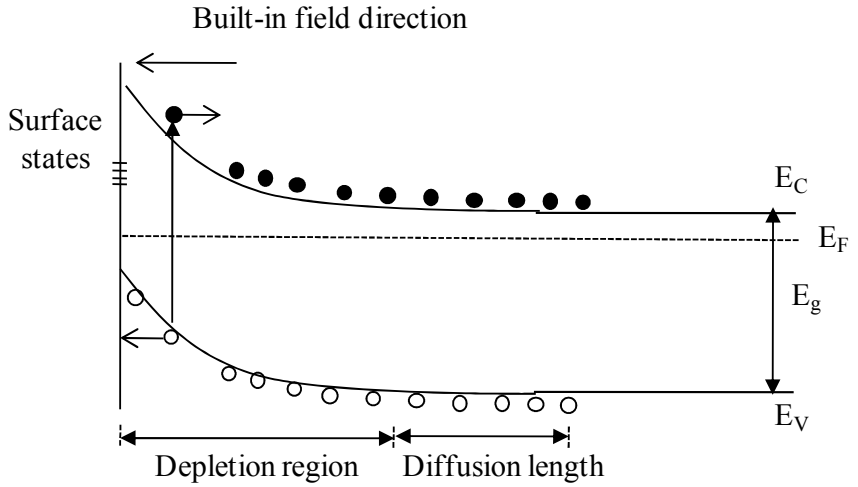

Figure 2.14: Schematic of the generation of photovoltage through various processes.

sample holder, which contains a indium tin oxide (ITO) coated transparent electrode.

2.9 Surface photovoltage spectroscopy

Surface photo voltage spectroscopy (SPS) [131, 132] is another form of absorption spectroscopy like PR and ER. The basic principle behind SPS technique is schematically shown in Fig. 2.14. It has been mentioned in the section describing PR technique that the surface of semiconductors has band bending leading to the depletion region and a built-in surface electric field associated with it due to the presence of surface states. When, a light of photon energy greater than the band gap of the semiconductor falls on it, electron and hole pairs are created in a region depending upon the penetration depth of the light in the semiconductor. Generated electron and hole pairs then get separated by the built-in surface electric field and change the surface potential. This change in surface potential is picked up in SPS technique. There several processes occur in the semiconductor after absorption of the light, which contribute in the SPS magnitude. 2) Electrons and holes generated

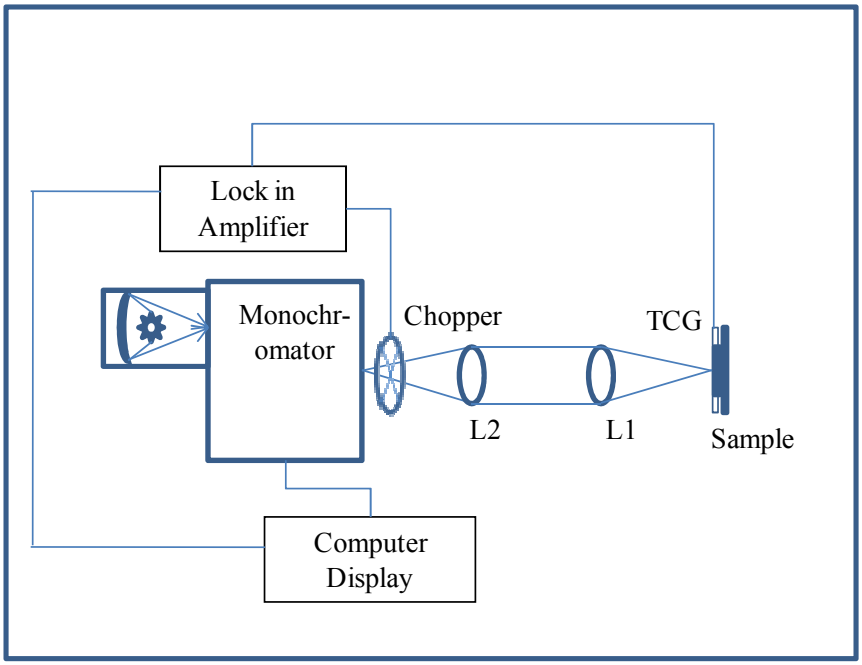

Figure 2.15: Schematic of the surface photovoltage experimental setup. L_1 and L_2 are focusing lenses.

within the diffusion length of the carriers from the edge of the depletion region may diffuse to the depletion region and are separated by the built-in electric field, 3) The electron and hole pairs generated in the zero electric field region (flat band condition) can also be separated due to the difference in their mobility and contribute in the SPS magnitude. This contribution is known as the Dember voltage. The experimental setup for SPS is schematically shown in Fig. 2.15, where the measurements are performed in the chopped light geometry under soft contact mode [132]. Periodic excess carrier generation and subsequent redistribution changes the surface potential, which is picked up by a transparent conducting glass (TCG) electrode. The TCG plate coated with indium-tin-oxide on the surface facing the sample is used as the second electrode as well as the window for the light. A 100 W quartz-tungsten-halogen lamp along with a 1/4 m SCIENCETECH monochromator is used as the

light source. The AC photo voltage signal is measured with a lock-in amplifier.

SPS technique is used to determine the band gap of the bulk semiconductors. In addition, it has been used to determine the ground as well as excited states of the quantum structures like thick QWs, QDs and even ultrathin QWs. Apart from this, SPS technique has been applied to determine the absorption co-efficient (α) of GaAs thick wafers [132, 133].

2.10 Capacitance-Voltage profiling

2.10.1 Theory

Studies on the capacitance associated with the depletion region of a Schottky barrier or an $p-n$ junction provide information of the concentrations and characteristics of electrically active centers in the near surface region of bulk semiconductors and their quantum structures [134]. Measurement of the depletion capacitance with applied voltage gives information about the fixed impurity and defect centers in semiconductors, in contrast to the carrier transport measurements (Hall measurements), which provide the information related to the density of free carriers and their mobility. Thus, capacitance-voltage and transport measurements give complementary information about the semiconductors. However, under some appropriate conditions as described in literature [134], the density obtained from the depletion capacitance measurements is equal to the free carrier density measured from the Hall measurements. In particular, depletion capacitance measurements provide information of the depth distribution of both shallow and deep impurity levels. On the other hand, transport measurements are unique in providing the mobility values [134]. Determination of the net dopant density from the measurement of the

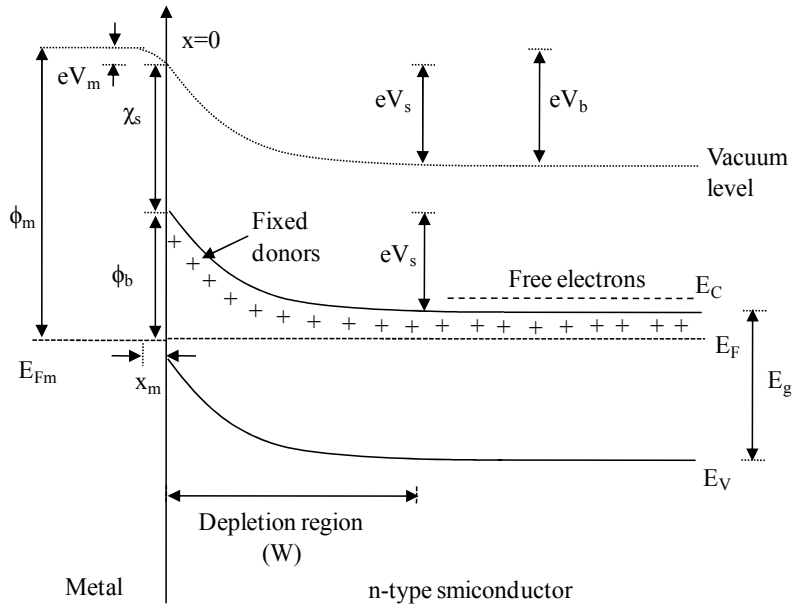

Figure 2.16: Schematic energy band diagram of a metal semiconductor Schottky junction.

capacitance associated with the depletion region of a metal semiconductor contact is described as follows. Real metal semiconductor contacts are generally described by Schottky model [134], which are characterized by a barrier height (ϕ_b) and have diode like characteristics. According to the Schottky model, the energy band diagram is constructed by reference to vacuum level, which is defined as the energy of an electron at rest outside the material. The material properties like work function of metal (ϕ_m) and electron affinity (χ_s) of semiconductor are defined as the energies required to remove one electron from the Fermi level of metal and conduction band of semiconductor, respectively, to the vacuum level. These are supposed to be the material properties, which are assumed to be constant in a given material right upto the interface and it is further assumed that the vacuum level is continuous across the interface. Hence, there must be a step between the Fermi level of metal and

conduction band of semiconductor because of the difference in the values of ϕ_m and χ_s as schematically shown in Fig. 2.16. This difference is known as the barrier height (ϕ_b) and is given by

$$\phi_b = \phi_m - \chi_s - eV_m \approx \phi_m - \chi_s, \tag{2.4}$$

because the band bending (eV_m) in the metal is very small due to the large electron density and can be neglected.

As we move away from the interface region (Fig. 2.16), the conduction band energy of the semiconductor changes such that it matches the bulk value E_C with respect to the Fermi level at large distances from the interface. The band bending results from the movement of free electrons, which leave behind a distribution of fixed ionized donor atoms with positive charge. The band bending region is called the depletion region (W), which is depleted from the free charge carriers and has only the density of non mobile ionized atoms. The region at which the band becomes flat and the associated electric field is zero is called the depletion edge. In metals, a neutralizing negative charge in the form of free electrons is accumulated at the contact region over a distance (x_m) known as the free carrier screening length. Since, electron density in the metals are quite large as compared to that in semiconductor, hence, $x_m << W$ and can be assumed that the potential drop across the metal contact (V_m) is small as compared to that in semiconductor (V_s). Thus, built-in voltage (zero bias band bending) can be written as

$$eV_b = eV_m + eV_s \approx eV_s = \phi_m - \chi_s - (E_C - E_F) \tag{2.5}$$

$$eV_b \approx \phi_b - (E_C - E_F)\,, \tag{2.6}$$

where e is the electronic charge.

The total band bending across the depletion region with the applied external reverse bias (V_a) is, therefore, equal to

$$V = V_b + V_a \tag{2.7}$$

The depletion width (W) can be calculated by knowing charge density ρ_x and solving Poisson's equation. For simplicity, it is assumed that the semiconductor has a constant doping density (N_d), which leads to the constant charge density in the depletion region

$$\rho(x) = eN_d^+ \tag{2.8}$$

where, N_d^+ is the density of ionized donor in the depletion region. The electrostatic potential, ϕ, is given by the Poisson's equation [134]

$$-\nabla^2\phi(x) = \nabla E(x) = \frac{\rho(x)}{\epsilon\epsilon_0} = \frac{eN_d^+}{\epsilon\epsilon_0}, \qquad 0 \leq x \leq W, \tag{2.9}$$

where, $E(x)$ is the electric field inside the depletion region. ϵ and ϵ_0 are the dielectric constant of the semiconductor and the permittivity of free space. Integration of above equation gives the electric field as

$$E(x) = E(0) + \frac{eN_d^+ x}{\epsilon\epsilon_0}, \qquad 0 \leq x \leq W, \tag{2.10}$$

and $E(x)$=0, for x<0 or x>W. Boundary condition of the zero electric field value at the depletion edge, W, leads to the determination of constant $E(0)$ and is found to be

$$E(0) = -\frac{eN_d^+ W}{\epsilon\epsilon_0}, \tag{2.11}$$

hence,

$$E(x) = \frac{eN_d^+}{\epsilon\epsilon_0}(x - W) \tag{2.12}$$

The above equation in terms of electrostatic potential can be written as

$$-\nabla\phi\left(x\right)=\frac{eN_{d}^{+}}{\epsilon\epsilon_{0}}\left(x-W\right). \tag{2.13}$$

Integration of above equation with the boundary condition, $\phi\left(0\right)=-V$, yields the following form of the electrostatic potential in the depletion region

$$\phi\left(x\right)=\frac{eN_{d}^{+}W}{\epsilon\epsilon_{0}}\left(x-\frac{x^{2}}{2W}\right)+V, \qquad 0\leq x\leq W. \tag{2.14}$$

Since, the potential is zero at the depletion edge, $\phi\left(x\right)=0$ at $x=W$ leads to the determination of the expression for the depletion width

$$W=\sqrt{\frac{2\epsilon\epsilon_{0}V}{eN_{d}^{+}}}. \tag{2.15}$$

The assumption of sharp depletion edge in the depletion approximation is not generally true. For a non-degenerate n-type semiconductor in the thermal equilibrium, the free carrier density n is given by the Boltzmann relation [134]

$$n=N_{C}exp\left(-\frac{E_{C}-E_{F}}{k_{B}T}\right), \tag{2.16}$$

where, k_B is the Boltzmann constant, T is the temperature, and N_C is the effective density of states in the conduction band. Hence, the charge density, earlier given by equation 2.8, can be written as

$$\rho\left(x\right)=e\left[N_{d}^{+}-n\left(x\right)\right]. \tag{2.17}$$

Using the first order approximation for $n(x)$ from equation 2.17, the charge density can be written as [134]

$$\rho\left(x\right)=eN_{d}^{+}\left[1-exp\left\{-\frac{1}{2}\left(\frac{W-x}{L_{D}}\right)^{2}\right\}\right], \tag{2.18}$$

where, L_D is the Debye length and is given by

$$L_D = \sqrt{\frac{\epsilon\epsilon_0 k_B T}{e^2 N_d^+}}. \tag{2.19}$$

It is noted from equation 2.17 that the free carrier density decreases approximately exponentially with the square root of the distance from W at a rate characterized by Debye length within the depletion region. Hence, Debye length is indicative of the abruptness of depletion edge and it represents the distance over which the free carriers redistribute themselves in the vicinity of a fixed charge. Thus, the free carrier density at a distance L_D and $3.03L_D$ from W is $n(x) = 0.61N_d^+$ and $n(x) = 0.01N_d^+$ respectively. This result indicates that the depletion region is depleted from the free carriers throughout its width except near the depletion edge. So, the requirement of the abruptness of depletion edge in depletion approximation is satisfied when the depletion width is much greater than the Debye length L_D.

The capacitance associated with the depletion region is known as the depletion capacitance as mentioned above. The depletion region of a Schottky barrier on a n-type semiconductor contains a distributed fixed charge density of ionized donor atoms. When the reverse bias is increased by a small amount ΔV, the depletion width increases causing an increase in the fixed charge per unit area ΔQ so that one can define a small signal capacitance associated with the depletion region as

$$C = A \lim_{\Delta V \to 0} \left(\frac{\Delta Q}{\Delta V} \right) = A \frac{dQ}{dV}, \tag{2.20}$$

where, A is the diode area. The incremental charge, dQ, stored in the increased depletion width, dW, is given by [135]

$$dQ = AeN_d^+ dW. \tag{2.21}$$

The change in voltage is determined from equation 2.15 as

$$dV = \frac{eN_d^+}{\epsilon\epsilon_0} W dW. \tag{2.22}$$

Thus, the capacitance is given by

$$C = \frac{dQ}{dV} = A\frac{\epsilon\epsilon_0}{W} = A\sqrt{\frac{\epsilon\epsilon_0 eN_d^+}{2V}}. \tag{2.23}$$

The depletion capacitance given by the above equation is similar to the expression for the capacitance of a parallel plate capacitor with the distance W and dielectric constant ϵ, although the charge is stored in the volume rather than on the edges of the depletion region. The expression for the depletion capacitance ca be rewritten as

$$\frac{1}{(C/A)^2} = \frac{2V}{\epsilon\epsilon_0 eN_d^+}. \tag{2.24}$$

Thus, if we plot $1/(C/A)^2$ versus V, then it will yield a straight line for the constant doping density. The slope of the linear line will give the doping density by the following relation

$$N_d^+ = \frac{2}{\epsilon\epsilon_0 e}\left[\frac{d\left(1/(C/A)^2\right)}{dV}\right]^{-1}, \tag{2.25}$$

and the intercept at the bias axis provides the information about the built-in voltage. The equation 2.25 remains valid for a non uniform doping density, because in the depletion approximation the charge fluctuations occur at the depletion edge. Hence, the doping profile can be obtained by measuring the capacitance as a function of reverse bias voltage and by using equation 2.25 alongwith

$$W = \frac{\epsilon\epsilon_0 A}{C}. \tag{2.26}$$

It is to be noted from the above discussion of the depletion approximation that the depth resolution of the capacitance-voltage profiling technique has a fundamental

limit of about $\pm L_D$. The detailed discussion about this technique, limitations and interpretations of the capacitance-voltage profiles can be found in the literature [134].

2.10.2 Experiment

In experiment, when a small ac voltage $V_{ac} = V_0 e^{i\omega t}$ is applied to a the depletion region, which is equivalent to a capacitor with capacitance C, then the current flow is given by

$$I_C = \frac{dQ}{dt} = C\frac{d}{dt}\left(V_{ac}\right) = i\omega C V_{ac}, \tag{2.27}$$

which can be written as

$$I_C = I_0 e^{i(\omega t + \pi/2)}, \tag{2.28}$$

where, $i = e^{i\pi/2}$ and $I_0 = CV_0\omega$. This tells that current is 90^0 out of phase with voltage. But in reality, there exists some leakage through the capacitor, which gives rise to the leakage current of the form

$$I_L = V_{ac}/R = V_{ac}G, \tag{2.29}$$

where, R is the resistance and G is the conductance. Hence, the total current is given by

$$I = I_C + I_L = \left(i\omega C + G\right) V_{ac} = Y V_{ac}, \tag{2.30}$$

where, $Y = (i\omega C + G)$ is called admittance. Thus, measurement of current and voltage with their respective phases determines the capacitance (imaginary part) and conductance (real part). So, every diode is represented by a junction capacitance (C), junction conductance (G) and a series resistance (R_s), which can be represented by the equivalent circuits as shown in Fig. 2.17. C_s and G_s are the capacitance and conductance when they are in series equivalent circuit, while C_p and G_p are

the capacitance and conductance when they are in parallel equivalent circuit. The capacitance meter assumes the device to be represented either in parallel or series equivalent circuit. Generally, series equivalent circuit is chosen if the device has larger impedance and if the device has low impedance, then parallel equivalent circuit is chosen. In our experiments, we have chosen parallel equivalent circuit because of the low impedance due to larger doping density in the barrier regions of ultrathin QWs. The details of the C-V experiments can be found in reference [136].

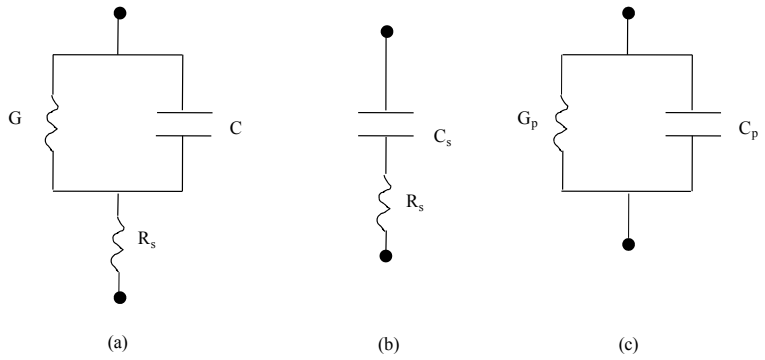

Figure 2.17: (a) Equivalent circuit of the actual device, (b) series equivalent circuit and (c) parallel equivalent circuit.

Chapter 3

Observation of electron confinement in InP/GaAs type-II ultrathin quantum wells

3.1 Introduction and background

Quantum structures based on type-II band alignment material systems such as InP/GaAs [100], ZnSTe/ZnTe [54], SiGe/Si [10] and GaSb/GaAs [7] have received much attention in the recent years due to their applications as photodetectors [7], optical memory devices [52], and solar cells [53]. Apart from these novel device applications, interesting physical phenomenon like Aharonov-Bohm oscillations in the optical spectrum due to the confinement of charge carriers in different regions has also been demonstrated [6]. Ultrathin QWs with typical thickness of 1-2 MLs have been also studied due to their unique electronic and optical properties leading to their use in the optoelectronic devices [8, 137].

The issue of type-II band alignment for InP/GaAs heterostructure has been addressed by several groups, where it is understood that the electrons (holes) are confined in the conduction (valence) band of InP (GaAs) [6, 9, 100, 103]. However, there are some interesting signatures of type-II band alignment phenomenon which

are normally seen in the PL measurements and seem to be missing for this material combination. For example, the blue shift in PL measurements is found to increase linearly with the cube root of excitation power which further increases with the QW thickness [7, 10, 138]. Recently, the type-II band alignment between InP and GaAs has been again ascertained on the basis of significantly reduced exciton binding energy for InP/GaAs QDs in magneto photoluminescence measurements [11]. However, QD structures grown using Stranski-Krastanov growth technique possess undesirable size, compositional and interfacial inhomogeneities leading to several complications. In view of this, pseudomorphically grown QW structures are more attractive. On the other hand, there is no direct evidence of carrier accumulation in InP/GaAs QWs which are normally seen in the C-V measurements [52, 139, 140]. In this chapter, we present detailed spectroscopic analysis, confirming the type-II band alignment between InP and GaAs, which is further supported by clear evidence of electron confinement in the InP/GaAs type-II ultrathin QWs from room temperature C-V measurements.

3.2 Experimental procedure

InP/GaAs ultrathin QWs with varying well width are grown in a horizontal MOVPE reactor (AIX-200) with a rotating substrate holder on nominally (0 0 1) oriented n^+-GaAs substrate at 50 mbar of reactor pressure. Trimethyl gallium (TMGa) and trimethyl indium (TMIn) are used as the precursors for group-III elements, while 100% arsine (AsH_3) and phosphine (PH_3) are used for group-V elements. 2% silane (SiH_4) diluted in hydrogen (H_2) gas is used for the n-type doping in the epitaxial layers. The flux of TMGa, TMIn, and SiH_4 are 2.065×10^{-5}, 4.965×10^{-6}, and

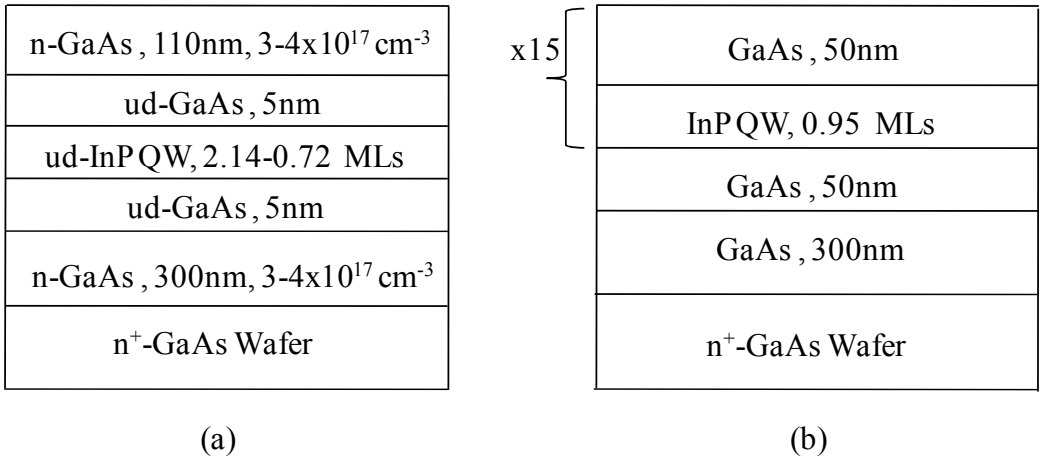

Figure 3.1: Schematic layer structure of (a) single quantum well (b) multiple quantum well.

2.647×10^{-7} mol/min respectively. The growth rate of GaAs barrier and InP QW layers are ∼2.5 Å/s and ∼0.4 Å/s respectively. The total gas flow of H_2 is about 8 litre/min. All the samples are grown at 600^0C with a V/III ratio of ∼100 for GaAs layers and ∼250 for InP ultrathin QW. The typical QW sample structure is shown in Fig. 3.1(a), which consists of ∼300 nm thick n-GaAs buffer layer, ∼5 nm unintentionally doped GaAs layer, unintentionally doped InP ultrathin QW of varying well width, ∼5 nm unintentionally doped GaAs layer and finally ∼110 nm thick n-GaAs cap layer. The layer structure of the studied QWs remains same for all the samples except that the QWs labeled as A, B, C and D have different thicknesses varying from ∼2.2 to 0.7 MLs as listed in Table 3.1. Buffer and cap layers of GaAs are doped with Si having a dopant density of $3\text{-}4\times10^{17}$ cm^{-3}.

In order to estimate the thickness of grown ultrathin QWs, a MQW sample is also grown. The layer structure for the MQW sample is also displayed in Fig. 3.1(b), which consists of 15 number of InP ultrathin QWs each seperated by ∼50 nm GaAs

Table 3.1

Sample	QW thickness (MLs)	GS transition energy, (eV) Exp.	GS transition energy, (eV) Calculated	FWHM (meV)
Sample A	2.14	1.403	1.5114	21
Sample B	1.43	1.424	1.5157	16
Sample C	0.95	1.466	1.5176	15
Sample D	0.72	1.482	1.5181	12

Table 3.1: Sample details indicating InP QW thickness, GS transition energies measured from PL experiments as well as calculated using envelop function approximation and FWHM of the QW transitions observed in PL measurements at 10 K.

barriers. All the layers in this sample are unintentionally doped. Structural properties like interfacial quality and thickness of ultrathin QWs have been estimated from HRXRD and TEM measurements of a MQW sample. Cross sectional TEM is carried out using Philips CM200 TEM operated at 200 kV. HRXRD measurements are performed by using a PANalytical X'PERT diffractometer with CuKα_1 x-rays (λ=1.54056 Å) and a four bounce hybrid monochromator. C-V measurements are performed at a measuring frequency of 4 KHz by using the depletion profile mode of an Accent Optical Technology PN4300 electro-chemical capacitance voltage (ECV) profiler. PL is excited with a diode laser beam (λ=808 nm), dispersed by a 1/4 m monochromator with a band pass of 4 nm and detected by a Si photodiode.

3.3 Structural properties

Figure 3.2(a) shows the HRXRD pattern of the MQW sample for (0 0 4) symmetric reflection. A clear observation of satellite peaks due to the periodicity of MQW structure confirms good crystalline and interfacial quality [141]. The thicknesses of QW and barrier layer are measured from HRXRD experiments by matching the measured diffraction pattern with the simulated one as shown in Fig.3.2(a) and are

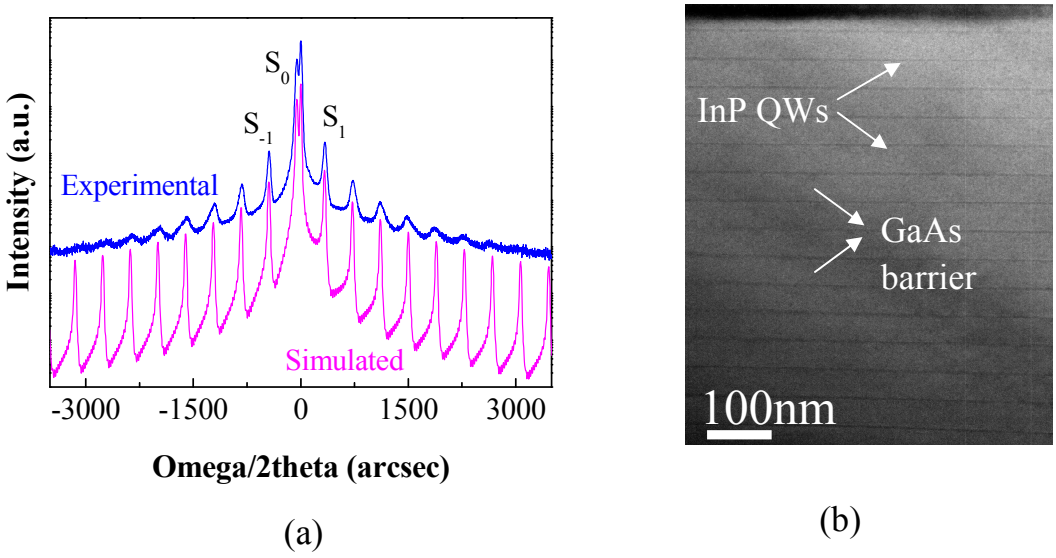

Figure 3.2: (a) Experimental as well as simulated HRXRD pattern for (0 0 4) symmetric reflection of the MQW sample. HRXRD patterns have been shifted in the vertical direction for clarity in viewing. (b) Cross-sectional TEM micrograph of the same sample.

found to be 0.28±0.01 nm (0.95±0.04 MLs) and 48.5 nm respectively. The simulation of HRXRD profile has been performed by using Epitaxy software. The interfacial quality and MQW period measured from the cross-sectional TEM micrograph corroborate with the HRXRD results as observed from Fig. 3.2(b). A pseudomorphic growth of the QW structures is therefore confirmed from the two measurements. Hence, the thicknesses of ultrathin QWs from the growth rate and time duration are estimated to be 2.14, 1.43, 0.95, and 0.72 MLs for samples A, B, C, and D, respectively, which is also listed in Table 3.1. Additionally, crystalline and interfacial qualities of the single ultrathin QWs can be analyzed from Fig. 3.3, which depicts the HRXRD pattern of the ultrathin QWs. We observe well defined Pendellösung fringes around the GaAs substrate peak for all the ultrathin QW samples, which arise due to the interference of x-rays diffracted from the GaAs cap layer and the

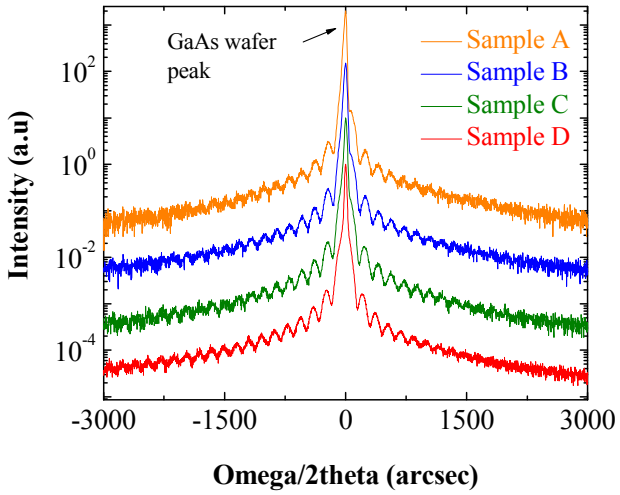

Figure 3.3: Experimental HRXRD pattern for (0 0 4) symmetric reflection of all ultrathin QW samples. Profiles have been shifted in the vertical direction for clarity in viewing.

substrate separated by InP ultrathin QW. Clear observation of Pendellösung fringes around the GaAs substrate peak indicates high crystalline and interfacial quality of the grown ultrathin QW samples [8, 142].

3.4 Type-II band alignment of InP/GaAs ultrathin QWs

Figure 3.4 shows 10 K PL spectra of InP/GaAs ultrathin QWs at 0.7 mW of the laser excitation power. Apart from the substrate related weak features at ∼1.52 eV and ∼1.50 eV, we also observe intense ultrathin QW features in 1.40-1.48 eV energy range. QW ground state transition energies obtained by fitting the PL spectra with a Gaussian function are 1.403, 1.424, 1.466, and 1.482 eV for samples A, B, C, and D, respectively. The transition energy increases from 1.403 to 1.482 eV with a decrease in QW thickness from 2.14 to 0.72 MLs. Another important observation is that the full width at half maximum (FWHM) of PL spectra decreases substantially with the decrease in size of ultrathin QWs as observed from Table 3.1. These are the unique

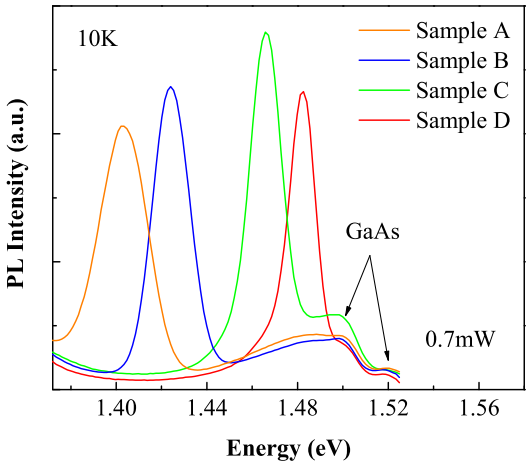

Figure 3.4: 10 K PL spectra for all the ultrathin QW samples.

characteristics of ultrathin QWs and are understood on the basis of presumption that such QWs are comprised of monolayer high islands with their lateral extent and separation lesser than the exciton radius for submonolayer coverage (<1 MLs) [143, 144]. When In coverage is increased above 1 ML, the islands first merge and form a continuous layer, subsequently the islands are formed again on top of the continuous layer for a fractional monolayer coverage [145, 146]. For all the samples, excitons experience an average QW thickness, which smoothly increases with the In coverage. Therefore, we observe a single PL peak (Figure 3.4) related to the average thickness of an ultrathin QW where the PL peak energy increases smoothly with decreasing QW size. The ground state transition energy for the ultrathin QWs have been calculated using envelop function approximation by assuming rectangular potential profile. The conduction band discontinuity of 0.18 eV has been taken as estimated from the capacitance-voltage measurements (**chapter 4**). We find a large difference between the calculated and experimentally measured ground state transition energies. It

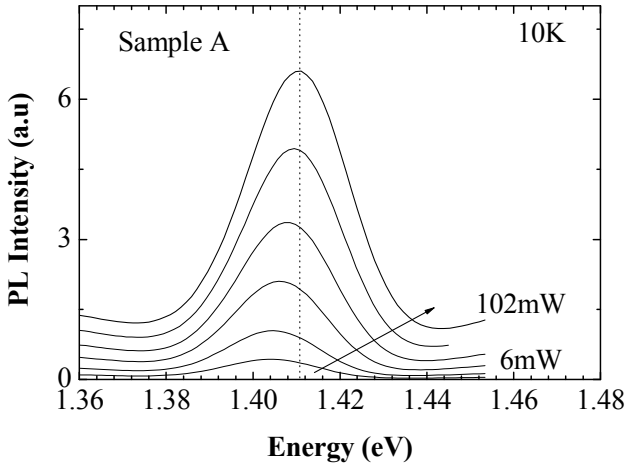

Figure 3.5: (a) Laser excitation power dependent PL spectra for sample A at 10 K. PL peak blue shifts with increasing excitation power.

seems that the simple calculations based on envelop function approximation are inappropriate for InP/GaAs type-II ultrathin QWs. Further, it should also be noted that the QW ground state energy for a thick QW (sample A) is lesser than the band gap (∼1.42 eV) of bulk InP indicating that the band alignment between InP and GaAs is type-II [54,55]. It has been reported that if a QW structure has type-II band alignment then PL peak position blue shifts with the excitation power (P) [100]. We, thus, perform power dependent PL measurements on these ultrathin QWs. Figure 3.5 shows PL spectrum at various laser excitation power for one ultrathin QW sample (sample A) as a representative. We note that the PL peak blue shifts with increase in laser power. Blue shift with laser excitation power can be understood from the QW band diagram. Such a band diagram for low and high laser excitation power has been drawn in Fig. 1.9 of **chapter 1**. We note that the triangular potential well formed at the hetero-interface in the valence band becomes sharper as laser power is increased. Thus, energy of hole confined in the triangular potential well increases

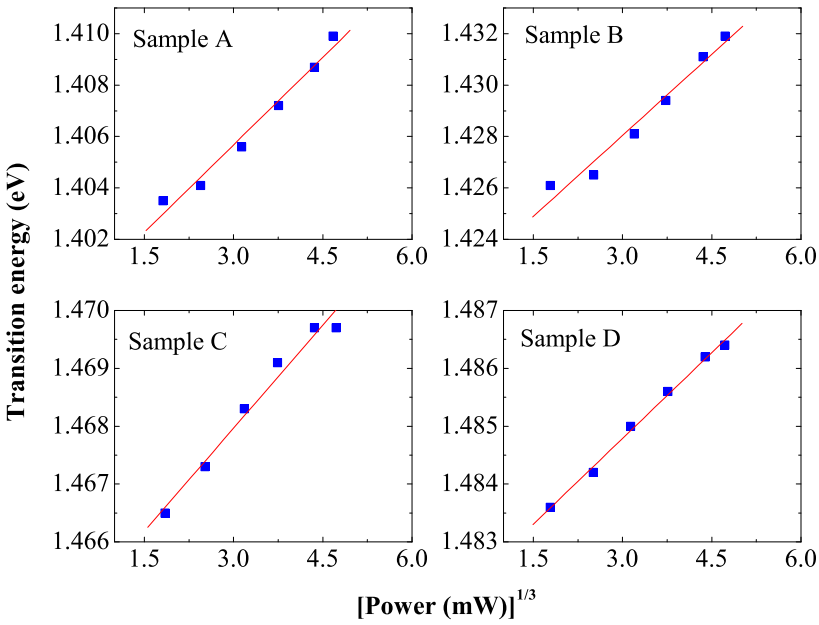

Figure 3.6: Graph between transition energy and cube root of the laser excitation power alongwith the linear fit for all the ultrathin QW samples.

and consequently transition energy in PL measurements blue shifts with increase in the laser excitation power. In addition to this, it has also been shown that the energy of hole confined at the interface increases linearly with the cube root of the laser excitation power ($P^{1/3}$) and ground state (GS) transition energy follows the cube root behavior with laser excitation power. In Fig. 3.6, we plot a graph between the transition energy and $P^{1/3}$ for all the ultrathin QW samples. We find that the PL peak position can be fitted with a straight line for all the samples, which confirms that the band alignment between InP and GaAs is type-II [7, 138]. Slope of the linear fit of the blue shift of transition energy versus $P^{1/3}$ is 2.3±0.2, 2.1±0.2, 1.3±0.1, and 1.0±0.1 meV/mW$^{1/3}$ for samples A, B, C, and D, respectively. Hence, thicker QWs show stronger blue shifts for the same power as compared to the thinner QWs. Similar observations have been made earlier for other type-II QWs [10, 54]. It has

been shown by Baier et al. [10] from theoretical calculations that the band bending induced by photo excited charge carriers leads to the blue shift of transition energy with excitation power. Furthermore, the blue shift is expected to increase with the QW thickness for a type-II QW as mentioned in **chapter 1**. Therefore, a blue shift in transition energy linearly varying with the cube root of laser excitation power which further increases with the QW thickness confirms that the band alignment in InP/GaAs ultrathin QWs is type-II.

3.5 Excitonic nature of photoluminescence from InP/GaAs ultrathin QWs

The nature of recombination process responsible for PL process can also be identified from the excitation intensity dependence of PL measurements. It is shown that the variation of the PL intensity (I_{PL}) can be described as follows [147]

$$I_{PL} \propto {I_{in}}^{\alpha} \tag{3.1}$$

where I_{in} is the excitation intensity and α is a parameter whose value changes depending upon the nature of recombination process [147, 148]. For example, the recombination is considered to be dominated by free excitons for α=1. If α=2, then the recombination is supposed to be dominated by free carriers. For a special case of $1<\alpha<2$, an interplay between excitons and free carriers is expected to determine the recombination process. Figure 3.7 shows a log log plot between integrated PL intensity and excitation power alongwith a linear fit for all the ultrathin QWs at 10 K. The measured value of α is 1.0, 1.1, 1.1 and 1.1 for samples A, B, C, and D, respectively. Thus, it is confirmed that the PL for all the ultrathin QW samples is of excitonic nature.

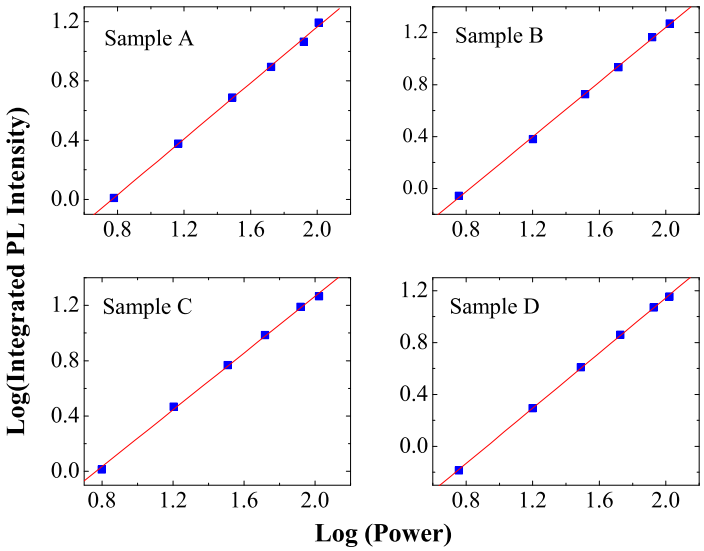

Figure 3.7: Log Log plot of integrated PL intensity versus laser excitation power at 10 K for all the ultrathin QW samples.

3.6 Electronic confinement in the conduction band of InP

C-V measurements are predominantly used to obtain the carrier distribution profiles in thick QWs [140], QDs [52] and even in the ultrathin QWs [13, 139]. Figure 3.8(a) shows the room temperature C-V curves obtained using ECV setup for all the ultrathin QW samples. A weak plateau in 0.8 to 1.5 V of reverse bias region is noted for sample A, while other samples do not show such plateau in the similar region of reverse bias voltage. Corresponding carrier distribution profiles obtained from C-V measurements for all the ultrathin QW samples are shown in Fig. 3.8(b). A strong peak observed at about ∼110 nm confirms carrier accumulation in the QW for sample A, which has the largest QW thickness. The carriers accumulated in the ultrathin QWs are electrons as ascertained from the sign of the slope of C-V curves. The accumulated carriers in the QW come from the surrounding barrier region, because there is a potential well for the carriers in the QW region. A weak signature

of the carrier accumulation in sample B is also noticed (3.8b). However, we do not observe any signature of the carrier accumulation in QWs for samples C and D, which have thicknesses lower than 1 ML. Thus, the carrier accumulation in ultrathin type-II QWs decreases with reduction of the QW thickness. It can be attributed to the interplay between the quantum confinement effect and carrier spillover in ultrathin QWs. When the QW thickness is reduced, the energy levels of electrons are weakly confined in the conduction band of InP ultrathin QW and thus show a large separation from the Fermi level resulting in a reduced electron accumulation in the QW [140]. Other possibility is related to an in-plane carrier diffusion due to sub monolayer thickness of QWs which would open a parallel channel for the carrier transfer. Therefore, room temperature C-V measurements (3.8b) provide a direct evidence for the confinement of electrons in the conduction band of InP in case of

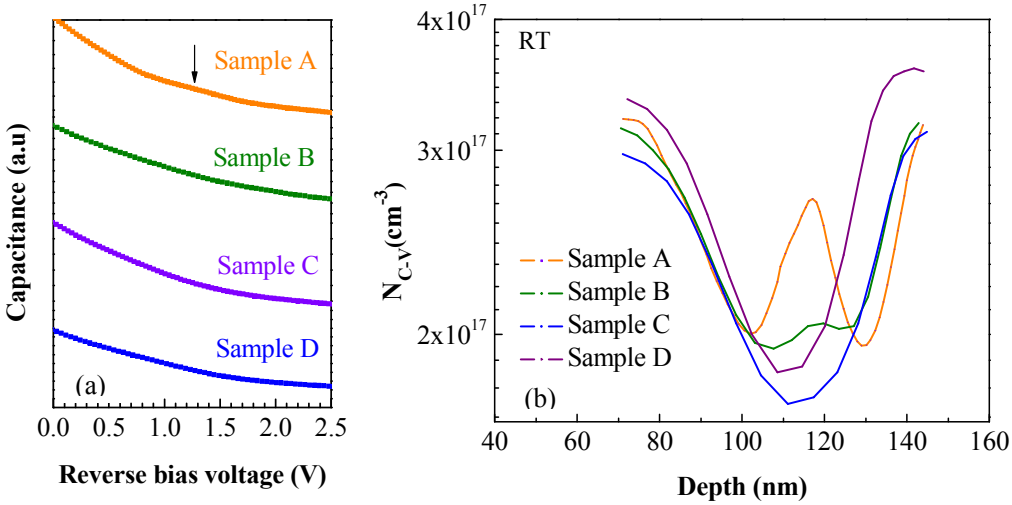

Figure 3.8: (a) Room temperature capacitance-voltage curves measured from the electrochemical capacitance voltage setup for all the ultrathin QWs. A weak plateau in 0.8 to 1.5 V of reverse bias region is noted for sample A. Curves has been shifted in the vertical direction for clarity in viewing. (b) Corresponding carrier distribution profiles derived from the capacitance voltage curves for all the ultrathin QW samples.

InP/GaAs type-II ultrathin QWs. We note that the FWHM of carrier depth profile in Fig. 3.8(b) is much larger than the width of ultrathin QWs. Similar observations have already been made for 1.1 ML thick InAs/GaAs ultrathin QW [13] and also for 10 nm thick InGaAs/GaAs QW [12]. It is understood that the Debye averaging process [12, 13] between two and three dimensional electrons is responsible for an apparent carrier distribution wider than the QW size under ambient conditions.

3.7 Summary

Ultrathin InP/GaAs QWs with excellent crystalline and interfacial quality are grown by MOVPE as confirmed from the cross-sectional TEM, HRXRD and the detailed PL measurements. It is determined that the PL emission from InP/GaAs ultrathin QWs is of excitonic nature. Specific signatures of the radiative recombination in PL measurements especially the cube root dependence of the blue shift on the excitation power, where the magnitude of such a dependence increases with the QW thickness, confirm a type-II band alignment in InP/GaAs heterostructure. A direct evidence of the confinement of electrons in the conduction band of InP QW is provided by the room temperature C-V measurements where the carrier accumulation is seen to decrease with a reduction in QW thickness. This is explained by a weaker confinement of carriers in thin QWs and a possible in-plane diffusion of carriers in ultrathin QWs of samples C and D due to their sub monolayer thickness.

Chapter 4

Quantum states and band offset for InP/GaAs type-II ultrathin QWs probed by capacitance-voltage measurements

4.1 Introduction and background

Carrier distribution characteristics play a very important role in determining the optimum performance of the optoelectronic devices. C-V measurements have been used to obtain the carrier distribution profiles in bulk [149] as well as quantum structures like QDs [52, 150], thick QWs [12, 151, 152] and even ultrathin QWs [13, 139]. Apart from this, temperature dependent C-V measurements have been used to distinguish whether the observed carrier distribution profile is due to the carriers confined in band offset systems or due to doping inhomogeneities [153]. There exist several reports dealing with the optical properties of InP/GaAs type-II QDs [11, 100, 103]. However, there is no report on the electrical properties of InP/GaAs ultrathin QWs. In addition to this, conduction band offset (ΔE_c) for InP/GaAs hetero-junction has not been measured by the C-V method, which has been widely used to determine the band offset of hetero-junctions and QWs [140,149,151,154]. We

have performed room temperature C-V measurements on InP/GaAs type-II ultrathin QWs as discussed in the **chapter 3** (Fig. 3.8(b)), where reduction in the carrier accumulation inside the QW region was noted with the decrease in QW thickness. This was attributed to the quantum size effect in the QW. As mentioned above, temperature dependent C-V measurements provide another way to confirm that the observed carrier accumulation is due to carriers occupying the quantum states formed in the QWs. Therefore, in this chapter we present detailed investigations on the temperature dependent C-V characteristics and also determine ΔE_c for MOVPE grown InP/GaAs ultrathin QWs.

4.2 Experimental procedure

InP/GaAs ultrathin QWs are grown in a horizontal MOVPE reactor (AIX-200) with a rotating substrate holder on nominally (0 0 1) oriented n^+-GaAs substrate at 50 mbar of reactor pressure. The growth process of the InP/GaAs ultrathin QW samples has been described in detail in **chapter 3**.

Current voltage (I-V) and C-V measurements on the ultrathin QWs are performed by making the Schottky contact on the top of n-GaAs cap layer and Ohmic contact on the back side of the n^+-GaAs wafer. Schematic of the sample used for the C-V measurements is shown in Fig. 4.1. Firstly, ultrathin QW samples are degreased by boiling in trichloroethele, acetone, and methanol for about a minute in each chemical sequentially and rinsed with de-ionized water. Then, samples are dipped in a dilute HCl solution (1HCl:10H_2O) to remove the native oxide on the sample's surface, before loading them in the vacuum coating unit for making Schottky and Ohmic contacts. Ohmic contact is fabricated by thermal evaporation of Au-Ge/Ni/Au on the back

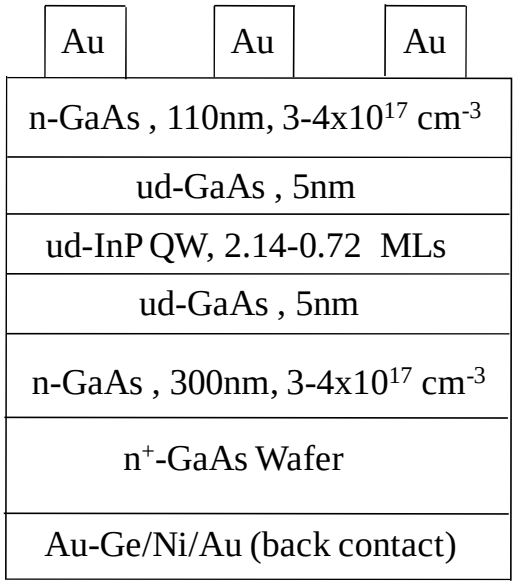

Figure 4.1: Schematic of the sample structure of ultrathin QWs used for C-V measurements. Au dots make Schottaky contact on the top of the GaAs cap layer, while Au-Ge/Ni/Au material combination provides ohmic contact on the backside of the GaAs wafer.

side of n^+-GaAs wafer. The ratio of Au and Ge is ∼88% and ∼12% respectively in the Au-Ge eutectic alloy. The typical thicknesses of Au-Ge, Ni and Au are 10 nm, 10 nm, and 100 nm, respectively. Subsequent to the evaporation of ohmic contact, rapid thermal annealing (RTA) of samples is performed in a home made RTA system at 450^0C for about 50 sec in nitrgogen (N_2) gas environment to reduce the contact resistance. Finally, Schottky contacts of about 100 nm thick are made by thermally evaporating the Au circular dots of about ∼700 μm diameter on top of the n-GaAs cap layer.

I-V measurements are performed to check the rectifying nature of the contacts and to determine the range of reverse bias voltage for the C-V measurements. I-V measurements are carried out with the help of Keithley source measure units with a sensitivity of ∼1 nV and ∼1 pA. C-V measurements are performed using a Keithley

capacitance meter at a frequency of 1 MHz. The ultrathin QW samples are placed into an indigenously developed close cycle refrigerator [155] for the temperature dependent C-V measurements from 50 to 300 K. We have studied the temperature dependent C-V characteristics for two ultrathin QW samples, sample A (∼2.14 MLs thick) and sample B (∼1.43 MLs thick). These two samples have been chosen because they show carrier accumulation at room temperature in the C-V plots as discussed in **chapter 3**.

4.3 Geometrical position of the ultrathin QWs

Geometrical position of the InP ultrathin QWs from the top surface is determined from the cross-sectional TEM measurements. Figure 4.2 shows the cross-sectional TEM micrograph for the two ultrathin QW samples. InP ultrathin QW corresponds to a thin dark line, which is observed at a depth of about 120 nm from the top surface that is in accordance with the planned position in MOVPE growth.

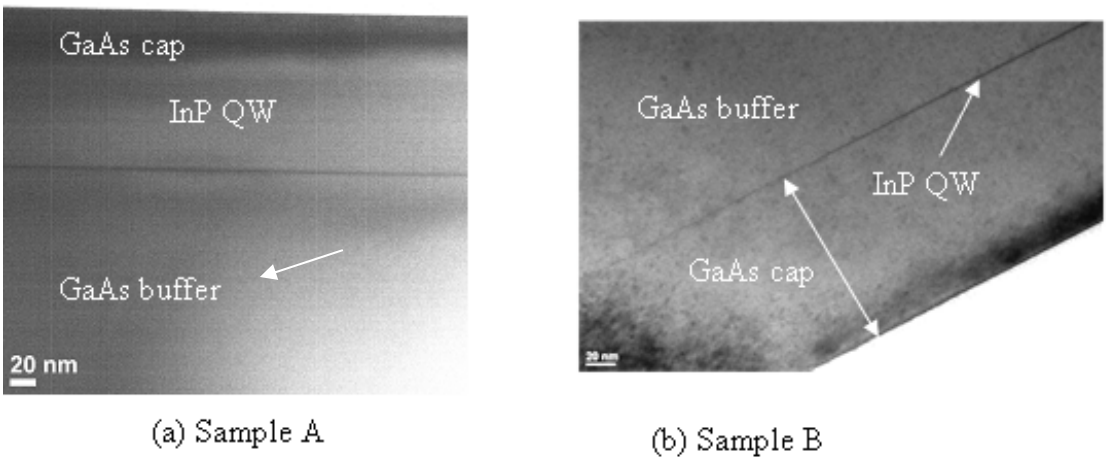

Figure 4.2: Cross-sectional TEM micrograph of ultrathin QW (a) sample A and (b) sample B. InP ultrathin QWs are observed as thin dark lines.

4.4 Probing the quantum states in InP/GaAs ultrathin QWs

Carrier distribution profile in quantum structures obtained from the C-V measurements does not follow the free carrier distribution (FCD) profile. Since FCD changes in a depth scale, which is smaller than the Debye length, this is represented as apparent carrier distribution (ACD) profile. However, useful information about the physical properties like band offset for the quantum structures can still be obtained by analyzing the ACD. ACD profile from the measured C-V characteristics has been derived by using the following relations [134]

$$N_{C-V}(z) = \frac{-2}{\epsilon\epsilon_0 A^2 \frac{\partial(1/C^2)}{\partial V}} \tag{4.1}$$

$$z = \frac{\epsilon\epsilon_0 A}{C} \tag{4.2}$$

where, z represents the distance along the growth direction, V is the applied voltage, C is the measured capacitance, A is the Schottky diode area, ϵ is the dielectric constant, and ϵ_0 is the permittivity of the free space.

Figure 4.3 shows the I-V characteristics of both the ultrathin QW samples at room temperature. We clearly observe the rectifying nature of the contacts deposited for the C-V measurements. It is further noted that the reverse current shows a very little change in the 0 to 2.8 V of reverse bias voltage. Hence, this voltage range of the reverse bias is suitable for the C-V measurements. It is to be noted that current for the 2.14 MLs thick ultrathin QW is more as compared to 1.43 MLs thick ultrathin QW in the reverse bias voltage region, which can be due to the larger number of carriers present in the QW region for 2.14 MLs thick ultrathin QW. Figure 4.4(a) and Fig. 4.4(b) show the temperature dependent C-V characteristics for samples A

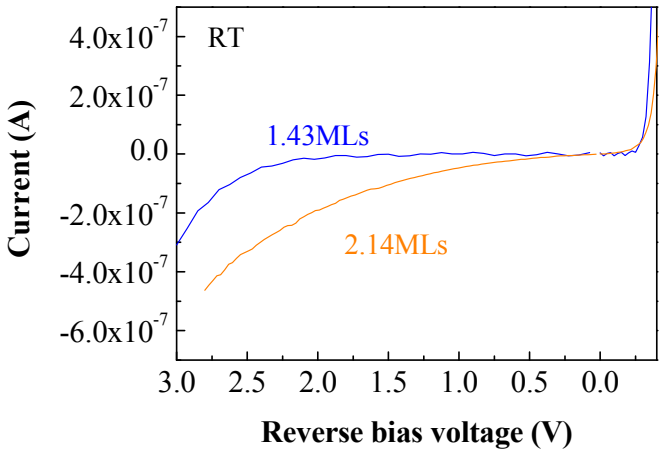

Figure 4.3: Current-voltage characteristic of ultrathin QW samples at room temperature showing the rectifying nature of the contacts.

and B respectively. Corresponding ACD profiles as well as their peak values and widths at various temperatures for both the ultrathin QW samples are depicted in Fig. 4.5(a), Fig. 4.5(b), and Fig. 4.6, respectively.

We observe a well defined plateau region between 0.5 to 1.0 V of reverse bias voltage in the C-V profile (Fig. 4.4(a)) for 2.14 MLs thick ultrathin QW at 50 K, which corresponds to the carrier accumulation (a peak in the ACD profile, Fig. 4.5(a)) at around the geometrical position of the ultrathin QW. The carriers are electrons as confirmed from the sign of the slope of the C-V curve. Presence of the plateau region in C-V profiles is a typical characteristic of a QW structure [140, 154]. Capacitance decreases with increase in reverse bias voltage due to increase in the depletion width of the barrier region having a constant doping density. As the depletion width approaches the QW region with increase in the reverse bias voltage, capacitance varies very slowly because of a large number of carriers present in the QW, which screen the applied electric field effectively. These carriers are the two-dimensional (2D) carriers occupying the quantum states formed in the QW region. When the

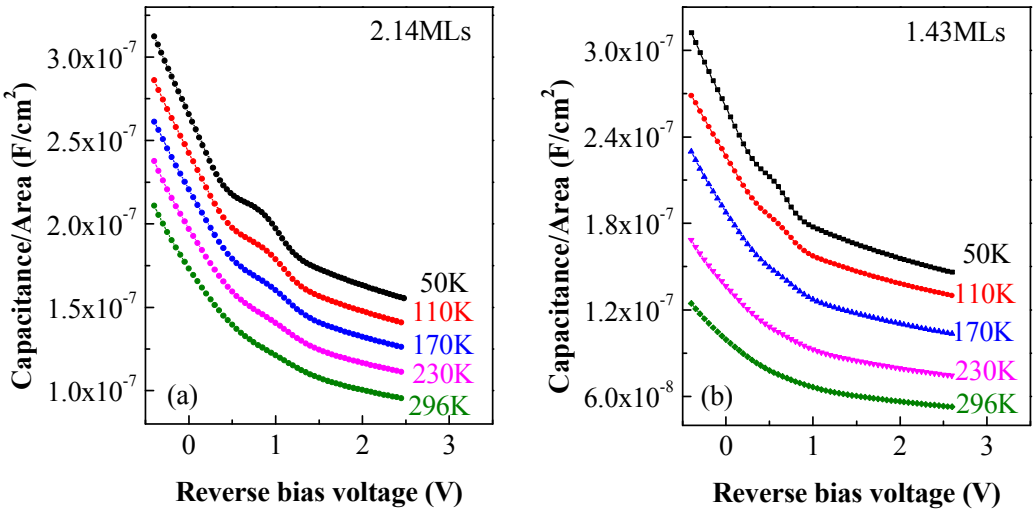

Figure 4.4: Temperature dependent capacitance-voltage curves for InP/GaAs ultrathin QWs: (a) sample A (b) sample B. Curves at different temperatures have been shifted vertically for clarity in viewing.

applied reverse bias voltage is large enough to sweep out all the carriers present in the QW, capacitance again decreases following increase in the depletion width of the barrier region having constant doping density. Thus a plateau region is observed in the C-V profile for a QW structure and its width is a measure of the number of the 2D carriers present in the QW. We also observe a plateau region in the C-V profile for 1.43 MLs thick ultrathin QW sample at 50 K as evident from the Fig. 4.4(b). We note that the plateau region is weaker for 1.43 MLs thick QW as compared to that of 2.14 MLs thick QW at the same temperature. This corresponds to lower peak value of ACD profile for 1.43 MLs thick QW as compared to that for 2.14 MLs thick QW (Fig. 4.5(a), Fig. 4.5(b), and Fig. 4.6).

Thus carrier accumulation in the thinner QW is less than that in thicker QW. Such behavior can be explained in terms of the quantum confinement effects in the QWs. We have noted earlier in **chapter 3** that the transition energy in PL

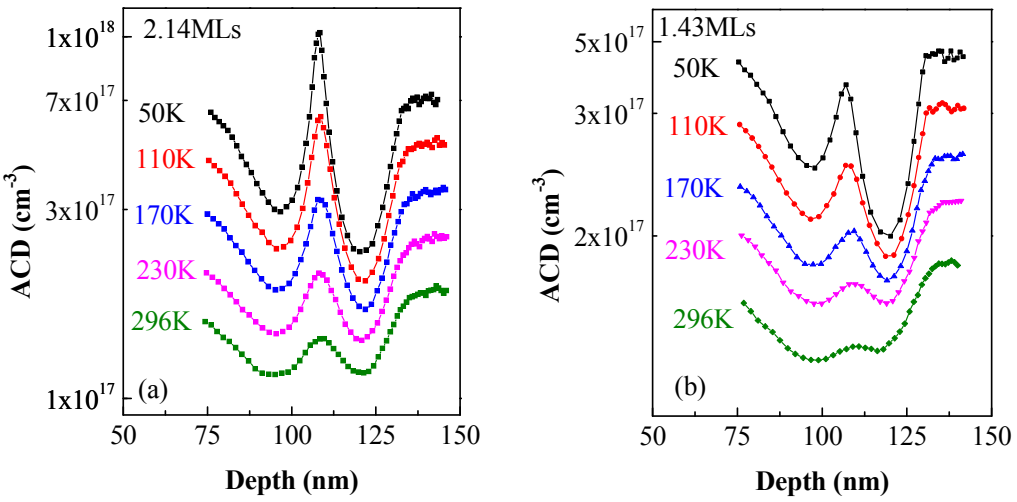

Figure 4.5: Temperature dependent apparent carrier distribution (ACD) profiles as obtained from the capacitance-voltage curves for InP/GaAs ultrathin QWs: (a) sample A (b) sample B. Curves at different temperatures have been shifted vertically for clarity in viewing.

measurements (Fig. 3.4) for thinner QW is higher than that for the thicker one. Hence, confined electronic level in the conduction band of InP QW comes closer to the conduction band of GaAs barrier, when well width is reduced because of the stronger quantum confinement effect in thin QW. Therefore, stronger confinement effect favors lower accumulation of carriers in the thin QW. We note that the plateau region gradually becomes weaker as the temperature is increased for both ultrathin QW as observed from Fig. 4.4(a) and Fig. 4.4(b). Such behavior in C-V profiles results in decrease in the peak value of ACD profile with increase in temperature as is evident from Fig. 4.5 and Fig. 4.6. This is due to the decrease in separation between Fermi level and quantum state (confined electronic level in the QW) as well as increased probability for thermal emission of electrons into the barrier region as a result of increased thermal energy with increasing temperature [152].

Another important observation made from the Fig. 4.5(a), Fig. 4.5(b), and Fig. 4.6

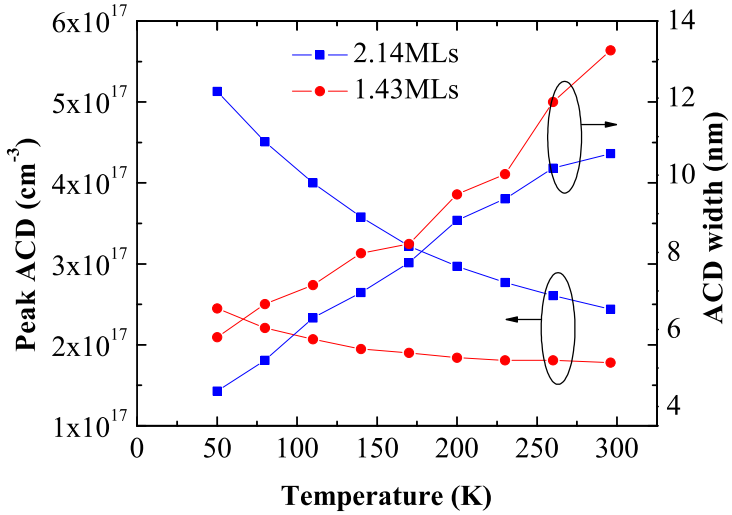

Figure 4.6: Apparent carrier distribution (ACD) peak value and its width as a function of temperature for both the InP/GaAs ultrathin QW samples.

is that the ACD profiles broaden with increase in the temperature for both the ultrathin QWs. Such observation has been noted earlier for the other quantum structures [12, 13]. It has been shown there that the ACD width at low temperatures is mainly decided by the change in position expectation value of 2D electrons, because of the negligible contribution from three dimensional (3D) electrons at low temperatures. Thus, a very small value of change in position expectation value of 2D electrons results in the small value of ACD width at low temperatures [12]. The contribution of 3D electrons increases with increase in temperature. Hence, Debye averaging effect between 2D and 3D electrons becomes very important in determining the width of ACD peak at higher temperatures, which results in the larger values of width of ACD peak at elevated temperatures [12, 13]. It has been reported in the literature that decrease in peak intensity and increase in width of ACD profile with increasing temperature are the typical characteristics of carriers occupying the

quantum states formed in the quantum structures [12, 13]. Therefore, temperature dependent C-V measurements confirm that the peak observed in ACD profile in the vicinity of the ultrathin QWs is due to 2D electrons occupying the quantum states formed in the ultrathin QWs. This is in agreement with our earlier conclusion made in **chapter 3** that the carrier accumulation in InP/GaAs type-II ultrathin QWs is due to the electrons confined in the conduction band of InP in theses QWs, which was drawn on the basis of the room temperature C-V measurements.

Furthermore, it is to be noted from Fig. 4.5(a) and Fig. 4.5(b) that there is no appreciable peak shift within the error of ±2 nm in the ACD profiles with temperature for both the ultrathin QWs. This is in contrast to the reported results in the literature, where large peak shifts in the ACD profiles with temperature have been observed. For example, ACD peak shift of 8 nm in the temperature range of 75-300 K for InGaAs/GaAs QW [152] and about 55 nm in 10-300 K temperature range for InAs/GaAs QDs [150] have been reported. ACD peak shifts with temperature in C-V measurements have been attributed to the change in Debye length with temperature [150]. Qualitative behavior of ACD peak shift as a function of temperature in C-V measurements can be understood from the temperature dependence of the Debye length (L_D), which is given by the following relation [134]

$$L_D = \sqrt{\frac{\epsilon\epsilon_0 k_B T}{e^2 N_d}} \tag{4.3}$$

where, N_d is the doping density in the barrier region, k_B is the Boltzmann constant, T is the temperature, ϵ is the dielectric constant, and ϵ_0 is the permittivity of free space. To provide a simple and qualitative picture, ionization probability of doping density with temperature has not been considered. Fig. 4.7 shows the variation

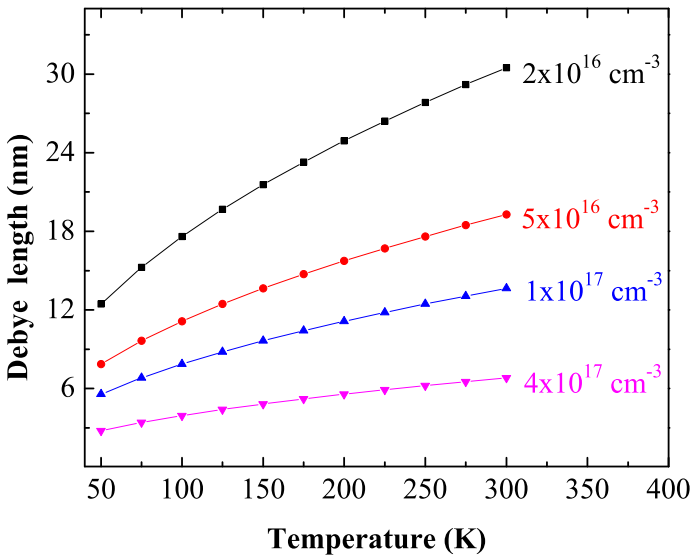

Figure 4.7: Variation of Debye length with temperature as a function of doping density in the barrier region.

of Debye length with temperature as a function of doping density using equation 4.3. We note that the Debye length decreases when temperature is lowered and it is the reason for the ACD peak shift. It is to be noted from Fig. 4.7 that the change in Debye length with temperature is less as doping density in the barrier region is increased. Therefore, ACD peak will show smaller shift with temperature for the higher doping density. We note that the doping density used in the barrier region for InGaAs/GaAs QW [152] and InAs/GaAs QDs [150] is 5×10^{16} cm^{-3} and 2×10^{16} cm^{-3} respectively. Thus higher doping density used in the barrier region of InGaAs/GaAs QW is responsible for smaller peak shift of ACD profile with temperature as compared to InAs/GaAs QDs systems. We have even larger doping density of 3-4$\times10^{17}$ cm^{-3} in the barrier region of our ultrathin QWs. This explains why we do not observe any appreciable ACD peak shift with temperature. Petrovskaya et

al. [152] have reported similar observation that the shift in ACD peak increases with the decrease in doping density by treating the quantum states of the QW as deep centers in the bulk semiconductors.

4.5 Determination of the conduction band offset for InP/GaAs ultrathin QWs

It has been shown in the literature that the band offset values for the QW structures can be determined by simulating the C-V curves [140, 151, 154]. Simulation of the C-V curves has been performed by solving Schrodinger and Poisson equations self-consistently under envelop function approximation (EFA) by taking the band discontinuities (ΔE_c and ΔE_v) as fitting parameters. We have simulated the C-V curve following the procedure as described in the literature [140, 154] and briefly described later in the appendix-A of this thesis. Fig. 4.8 shows the simulated as well as experimental C-V profile for the 2.14 MLs thick ultrathin QW sample. We

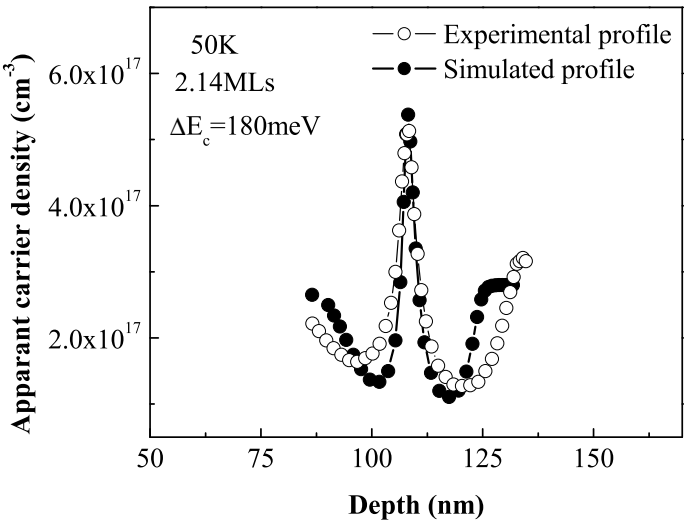

Figure 4.8: Experimental as well as simulated C-V profile at 50 K for 2.14 MLs thick ultrathin QW sample.

observe a reasonable fit for the conduction band discontinuity (ΔE_c) value of 180 meV. We associate an error bar of 30 meV in the value of ΔE_c, which can arise due to the QW thickness uncertainty, doping density in the barrier region as well as other source of errors that are inherently present in the C-V measurements as discussed in the literature [140, 149]. Now, we compare the value of ΔE_c determined in this work with the values reported in the literature. A value of 197±50 meV for the valence band discontinuity (ΔE_v) has been measured by using x-ray photoelectron spectroscopy for the InP/GaAs hetero-junction, which is also in corroboration with the value reported in the literature for the unstrained case [100, 156]. The estimated unstrained value of ΔE_c is 297±50 meV for InP/GaAs type-II system [100] as shown in Fig. 4.9, where a band diagram for unstrained and fully strained (3.8%) cases of the InP/GaAs type-II QW system has been drawn. The effect of strain in shifting the conduction and valence bands of InP has been considered by the following equations reported in the literature [157].

$$\delta E_C = 2a_c \frac{(a_0 - a)}{a} \left[\frac{C_{11} - C_{12}}{C_{11}} \right] \tag{4.4}$$

$$\delta E_{VHH} = 2a_v \frac{(a_0 - a)}{a} \left[\frac{C_{11} - C_{12}}{C_{11}} \right] - b \frac{(a_0 - a)}{a} \left[\frac{C_{11} + 2C_{12}}{C_{11}} \right] \tag{4.5}$$

where, δE_C and δE_{VHH} are the shifts in the conduction band edge and the heavy hole band edge of InP QW respectively. a_c and a_v are the hydrostatic deformation potential for the conduction and valence band respectively, while b is the shear deformation potential for InP material. a_0 and a are the lattice constants of GaAs barrier layer and InP QW respectively. C_{11} and C_{12} are elastic stiffness constants of InP material. The values of these parameters have been taken from the reference [157]. Wang et. al. [100] have also calculated a value of 130±50 meV for ΔE_c of fully strained (3.8%)

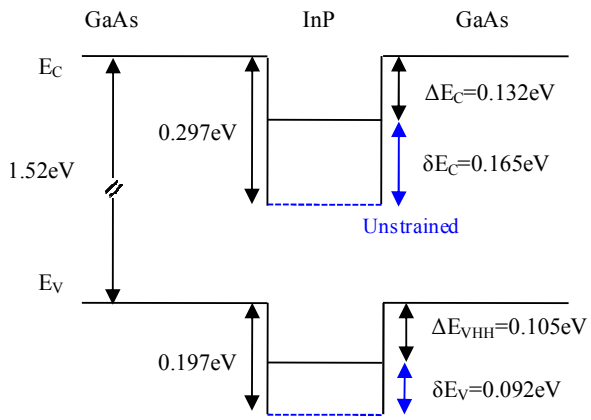

Figure 4.9: Band diagram for InP/GaAs type-II QW. Dashed and solid lines are for the unstrained and fully strained cases of InP QW. All values are given for temperature of 10 K.

InP/GaAs hetero-junction. It is to be noted that the InP/GaAs ultrathin QWs studied in the present work are also fully strained as discussed in **chapter 3**. Therefore, the value of ΔE_c determined by using the C-V method for the InP/GaAs ultrathin QWs is in agreement with the strained value of ΔE_c reported in the literature within the associated error bar. However, it is to be noted that calculations based on EFA have been found limitation in case of ultrathin QWs [8, 142]. In spite of this, such a simple approach is found extremely helpful in explaining the experimental results [8, 142]. Therefore, precise calculations using empirical tight binding [158] or self-consistent pseudo potential [159] method are desirable to obtain very accurate value of band offset for such ultrathin QWs. However, these calculations are beyond the scope of the present thesis.

4.6 Summary

We have carried out temperature dependent C-V measurements on MOVPE grown InP/GaAs ultrathin QWs. Cross-setional TEM and HRXRD measurements

confirm good crystalline and interfacial quality of the grown ultrathin QWs. We observe a plateau region in the C-V characteristics of the ultrathin QWs, which corresponds to a peak in the ACD profile at around the geometrical position of the ultrathin QWs. ACD peak value decreases with the reduction in the QW thickness. This has been attributed to the stronger quantum confinement effect in the thinner QW, which favors less accumulation of 2D electron in thin QW as compared to thicker one. Plateau region becomes weaker as the temperature is increased resulting in a decrease in the ACD peak value. This is due to the decrease in the separation between the confined electronic state and Fermi level as well as increased probability of the thermal emission of electrons in to the barrier regions. ACD width is found to increase with increase in temperature. Debye averaging process between 2D and 3D carriers is responsible for the ACD width at high temperature, while at low temperature ACD width is mainly due to the small value of change in position expectation value of 2D electrons, because of the negligible contribution from 3D electrons at low temperature. Therefore, temperature dependent C-V results confirm that the observed ACD profile is due to the 2D electrons occupying the quantum states formed in the ultrathin QWs. ACD peak does not show appreciable shift with temperature for both the ultrathin QWs. This has been understood in a simple and qualitative way by considering the temperature dependence of Debye length, where we have noted that Debye length is less susceptible to the temperature variation as doping density in the barrier is increased. A value of 180±30 meV of the conduction band discontinuity for the fully strained InP/GaAs hetero-junction has been obtained by simulating the C-V curve for the InP/GaAs ultrathin QW.

Chapter 5

Temperature dependence of the photoluminescence from InP/GaAs type-II ultrathin quantum wells

5.1 Introduction and background

There exist several reports dealing with the optical properties of InP/GaAs type-II QDs, where the signature of InP/GaAs ultrathin QW, known as a wetting layer in the QD structures, has been observed in the low-temperature PL spectra [100, 103]. However, the optical properties of InP/GaAs ultrathin QWs (which means no QDs exist in the same structure) have not been discussed in the literature. Therefore, a study of the optical properties for InP/GaAs ultrathin QWs is essential, which will help in developing better understanding of the optical properties of the InP/GaAs QD structures. Temperature-dependent PL is not only used to investigate the carrier phonon-interaction (as discussed in **chapter 1**) but also to provide useful information about the luminescence loss mechanism, which is very necessary from the point of view of device operation. Temperature dependence of the transition energy from the QW structures has followed the temperature dependence of the band gap variation of the QW material in case of thick QWs [160, 161]. On the other hand, for the

case of ultrathin QWs, temperature dependence of the QW transition energy follows the band gap variation of either the QW material or the barrier material [8, 162]. Additionally, various processes like thermal emission of charge carriers from QW layer to the barrier region, non-radiative recombination at defect centres etc. have been identified in the literature as the PL quenching mechanism with temperature.

We have grown high quality InP/GaAs ultrathin QWs as confirmed from the HRXRD, cross-sectional TEM and low temperature PL measurements which has been described in detail in **chapter 3**. Additionally, type-II band alignment between InP and GaAs hetero-structure has been confirmed from the cube root dependence of the transition energy on the laser excitation power in low temperature PL measurements as presented in **chapter 3**. Thereafter, band offset of InP/GaAs heterojunction and the quantum states formed in these InP/GaAs ultrathin QWs have been analyzed by using temperature dependent C-V measurements in **chapter 4**. In this chapter, we perform temperature dependent PL measurements on these InP/GaAs ultrathin QWs in order to analyze the temperature dependent behavior of the PL transition energy as well as to determine the PL quenching mechanism with temperature.

5.2 Experimental procedure

InP/GaAs ultrathin QWs are grown in a horizontal MOVPE reactor (AIX-200) with a rotating substrate holder on nominally (0 0 1) oriented n^+-GaAs substrate at 50 mbar of reactor pressure as described in **chapter 3**. PL is excited with a diode laser beam (λ= 642 nm), dispersed with a 1/4 m monochromator and detected by a Si photo-diode. The band pass of the monochromator is kept at about 2 nm. For the

temperature-dependent (10-300 K) PL measurements, samples are placed in a close cycle refrigerator. Cross sectional TEM is used to confirm that only QW structures are present and no QD structures are formed. TEM is carried out using Philips CM200 TEM operated at 200 kV.

5.3 Realization of only QW growth and no QD formation

Figure 4.2(b) in **chapter 4** shows the cross-sectional TEM micrograph for a 1.43 MLs thick ultrathin QW sample. We see a thin dark line corresponding to InP ultrathin QW. However, we do not observe any signature of the QD structures in our sample as is evident from the cross-sectional TEM micrograph. Hence, we do not expect any QD formation in a 0.95 MLs thick ultrathin QW sample either, which has even lower thickness than 1.43 MLs ultrathin QW. These observations are expected as the amount of InP in our ultrathin QW samples is lower than that is required to form the QDs at this temperature range [100, 103]. Thus, it is confirmed that only InP ultrathin QWs are present in our samples.

5.4 Temperature dependence of the transition energy for ultrathin QWs

Figure 5.1 shows 10 K PL spectra for the InP/GaAs ultrathin QW samples over a wider energy range. We observe intense PL from the ultrathin QWs in 1.4-1.48 eV energy range that shifts to higher energies with reduction in QW thickness. Apart from this, a broad feature is observed from the GaAs wafer at around 1.34 eV. In addition to this, two features are also observed at energies higher than the QW transitions. Feature at around 1.49 eV is due to recombination of carbon related impurity in MOVPE grown GaAs barrier layers [163], while feature at around 1.52

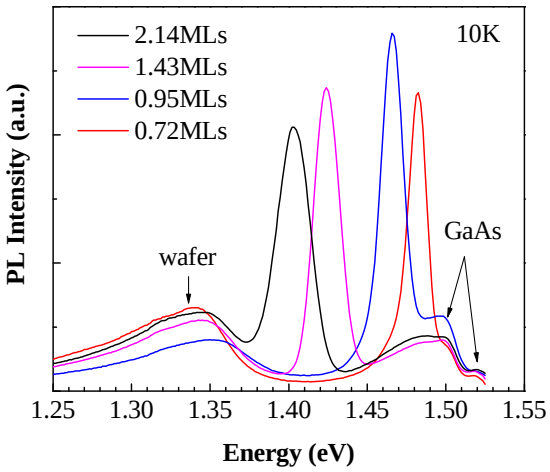

Figure 5.1: 10 K PL spectra for InP/GaAs ultrathin QWs. In addition to intense features related to InP/GaAs ultrathin QWs, features from the GaAs wafer and GaAs barrier layer are marked.

eV originates from the band edge of GaAs. Observed QW related PL transitions are originating from the recombination between the electrons confined in the conduction band of InP ultrathin QW and the holes in the GaAs barrier as discussed in detail in **chapter 3**. Blue shift in the PL peak energy with the reduction in ultrathin QW thickness has been observed earlier for InAs/GaAs, InAs/InP, GaAs/GaAsSb and ZnSTe/ZnTe ultrathin QWs and it has been shown there that this is due to the quantum confinement effect in the ultrathin QWs [54, 164–166] as discussed in **chapter 3**. We observe that the PL peak energy of 2.14 MLs thick ultrathin QW, being relatively nearer to the broad feature from GaAs wafer, merges with it when temperature of PL measurements is increased. Similarly, PL peak of 0.72 MLs thick ultrathin QW, being relatively nearer to the band edge feature from the GaAs barrier layer, merges with the later when the temperature of PL measurements is increased. The energy separation of PL features of 0.95 MLs and 1.43 MLs thick ultrathin QWs

from GaAs features is relatively large. Hence, temperature dependent PL of these two ultrathin QWs (0.95 MLs and 1.43 MLs thick) has been performed and analyzed in depth as discussed below.

Figure 5.2 shows the PL spectra at various temperatures for 1.43 MLs and 0.95 MLs thick ultrathin QWs. Apart from the QW PL (denoted by QW), we observe two features related to the GaAs barrier layer and a broad feature from the GaAs wafer as mentioned earlier. Henceforth, we will mainly concentrate on the temperature dependence of PL from the ultrathin QWs. We note that the PL intensity of the QW feature gradually decreases while that from the GaAs barrier layer increases as the temperature is increased for both ultrathin QW samples. We also observe that

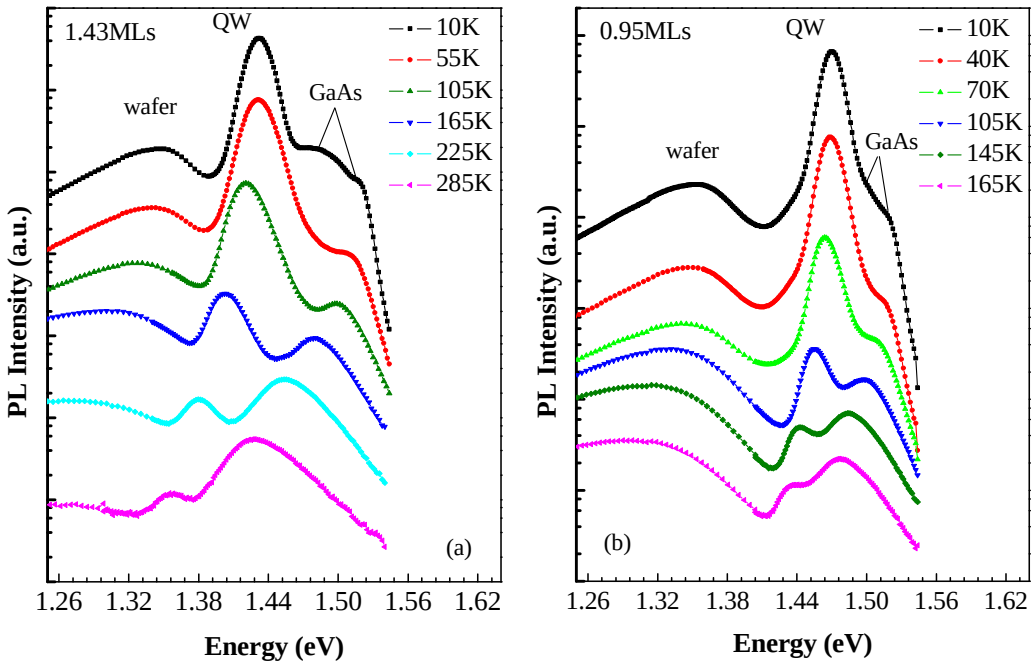

Figure 5.2: Temperature dependent PL spectra for the (a)1.43 MLs and (b) 0.95 MLs thick ultrathin QW. Features from the QW, GaAs barrier layer and GaAs wafer are also marked.

both QW and GaAs related features become broader with increasing temperature and the QW feature finally merges with the GaAs feature due to relatively small energy separation between them. In order to understand such temperature-dependent PL behavior from these ultrathin QWs, we determine transition energy, FWHM and integrated PL intensity as a function of temperature. These parameters have been obtained by the Gaussian fitting of the PL spectra. Figure 5.3 shows the graph between QW transition energy versus temperature for both ultrathin QWs. We see that the transition energy red shifts with an increase in temperature following the usual band gap reduction with an increase in temperature [79]. Temperature dependence of the band gap of bulk semiconductors as well as their quantum structures has been described mostly by Varshni and Bose-Einstein empirical relations [8, 160]. Temperature dependence of the PL peak energy of type-II transitions has already been fitted by using the Varshni relation [167]. However, it has been reported that temperature dependence of the band gap at low temperatures is better described by the Bose-Einstein empirical relation as compared with Varshni relation [88]. Therefore, in view of this, we have also analyzed QW transition energy ($E(T)$) of InP/GaAs type-II ultrathin QWs as a function of temperature (T) by using the Bose-Einstein relation (equation 1.8 in **chapter 1**). There exists a large probability of exciton formation at low temperatures predominantly due to reduced thermal energy. We have also observed excitonic recombination in low-temperature PL measurements for InP/GaAs type-II ultrathin QWs as discussed in **chapter 3**. Recently, a value of $\sim$1.5 meV for exciton binding of InP/GaAs type-II QDs has been reported from the magneto-PL measurements, which is very small as compared to those for type-I systems [11]. We, therefore, believe that the exciton binding energy for InP/GaAs

ultrathin QWs will also be small, because of the type-II band alignment. Thus, QW transition energies shown in Fig. 5.3(a) and Fig. 5.3(b) for the InP/GaAs type-II ultrathin QWs at very low temperatures are essentially for the excitons. However, as the temperature is increased, transition energies correspond to the free carrier recombination as compared to the exciton recombination because of the relatively small exciton binding energy for type-II systems. The solid line in Fig. 5.3(a) and Fig. 5.3(b) is the fitting using the Bose-Einstein empirical relation and the fitting parameters obtained are listed in the Table 5.1.

We find that the values of a_B and θ_{BE} for the InP/GaAs ultrathin QWs are similar to those for InP and GaAs materials [15]. We also note that there is not much difference between the values of a_B and θ_{BE} for InP and GaAs materials as is evident from the Table 5.1. Hence, on the basis of the measured values of a_B and θ_{BE} for ultrathin QWs we can not unambiguously determine whether the temperature dependence of the QW transition energy follows the band gap variation of GaAs

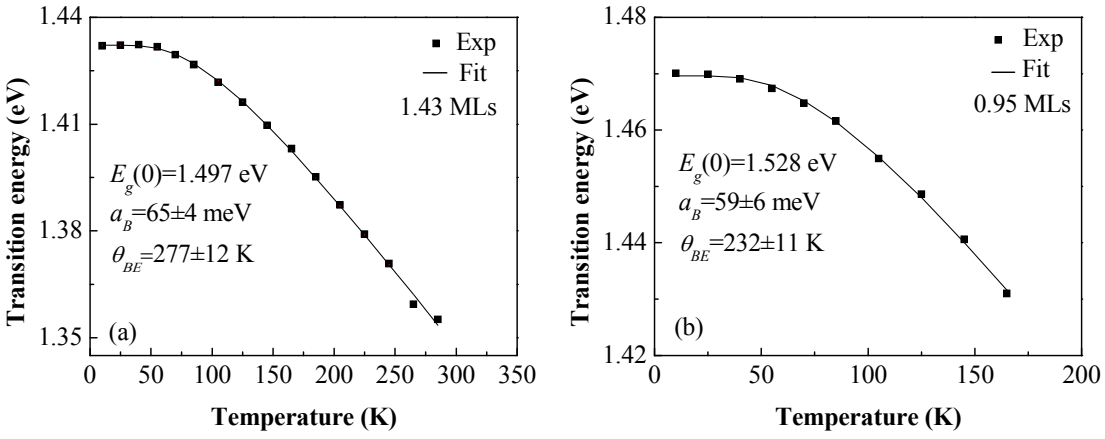

Figure 5.3: Variation of transition energy with temperature for InP/GaAs ultrathin QWs having thicknesses (a) 1.43 MLs and (b) 0.95 MLs. Solid line is the fitting using Bose-Einstein empirical model.

Table 5.1

Sample	a_B (meV)	θ_{BE} (K)	E_A (meV)	$\Delta\,(meV)=$ $E_g\,(GaAs)$ $-PL\,(peak)$
1.43 MLs[a]	65±4	277±12	79±7	87
0.95 MLs[a]	59±6	232±11	44±4	49
GaAs[b]	60	252	-	-
InP[b]	54	274	-	-

Table 5.1: Summary of the temperature dependent PL analysis.[a]This work. [b]From reference [15]. E_A is the activation energy responsible for PL quenching with temperature and Δ is the energy separation between QW and GaAs features.

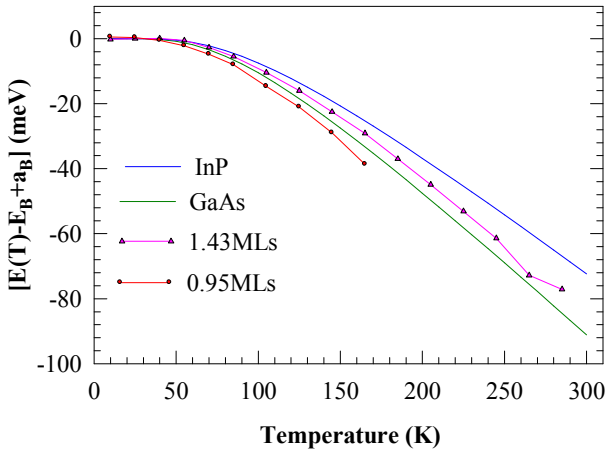

Figure 5.4: Variation of $E(T)-E_B+a_B$ with temperature for InP, GaAs materials as well as InP/GaAs ultrathin QWs.

and/or InP materials. For, unambiguous assignment, the values of $E(T)-E_B+a_B$ for ultrathin QWs, GaAs, and InP materials are plotted as a function of temperature in Fig. 5.4. We clearly note that the temperature dependence of the QW transition energy is similar to that of the GaAs material. This result is consistent with our observation that is made in case of InAs/GaAs ultrathin QW, where temperature dependence of the QW transition energy is found to follow the band gap variation of GaAs barrier material rather than the QW material [8]. FWHM of PL peaks for both ultrathin QWs as a function of temperature are shown in Fig 5.5. We note that

FWHM increases with increase in temperature for both the ultrathin QWs. The observed broadening is due to the electron-phonon scattering. At high temperatures a large error is seen in the FWHM of PL peaks due to its smearing with the band edge peak of the GaAs barrier layer.

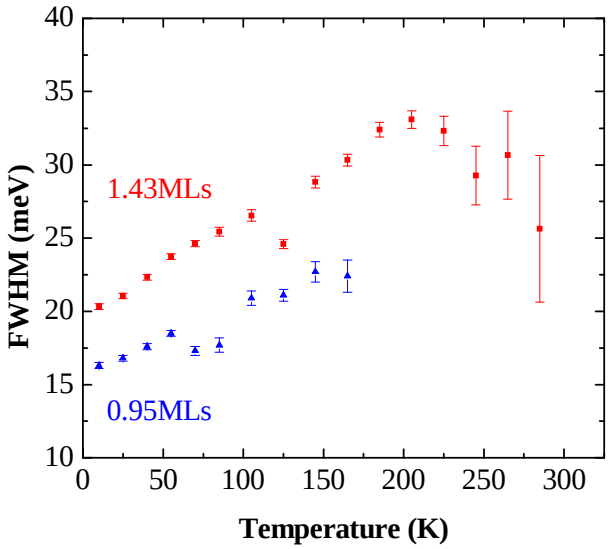

Figure 5.5: FWHM of PL spectra as a function of temperature for both the InP/GaAs ultrathin QWs.

5.5 Identification of the photoluminescence quenching mechanism for the ultrathin QWs

The mechanism, which is responsible for the PL quenching at high temperature, can be determined by knowing the integrated PL intensity as a function of temperature. The variation of PL intensity (I) with temperature (T) can be described by a phenomenological expression [168]

$$I = \frac{I_0}{1 + C exp\,(-E_A/k_B T)} \tag{5.1}$$

where I_0 is the intensity at temperature T = 0 K, C is a constant, k_B is the Boltzmann constant and E_A is the activation energy responsible for the PL quenching

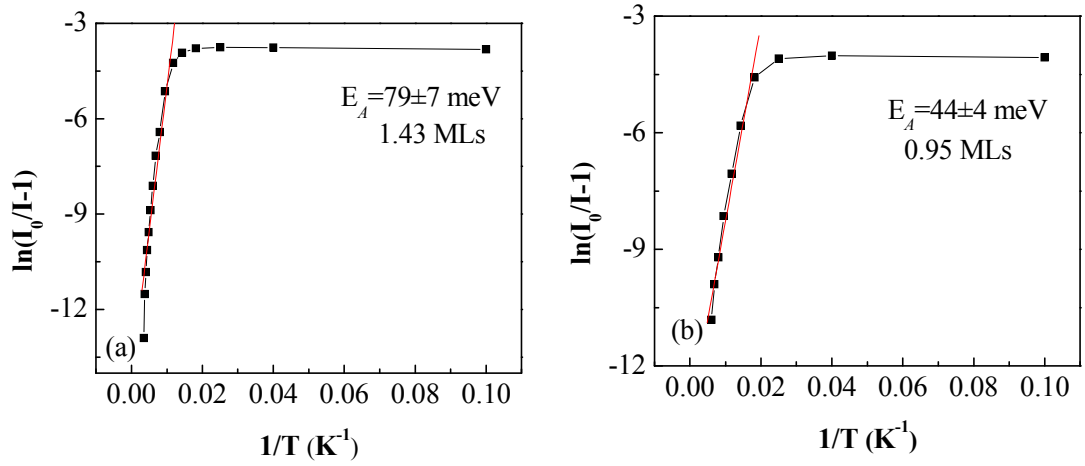

Figure 5.6: Arrhenius like plot of integrated PL intensity for InP/GaAs ultrathin QWs for thicknesses (a) 1.43 MLs and (b) 0.95 MLs.

with temperature. Thus, if we plot $\ln(I_0/I - 1)$ versus $1/T$, then the slope of linear fit gives the activation energy. Such plots for both the ultrathin QWs alongwith the linear fitting have been shown in Fig. 5.6(a) and Fig. 5.6(b). We determine the activation energies as 79±7 meV and 44±4 meV for 1.43 MLs and 0.95 MLs thick ultrathin QWs, respectively and these are listed in Table 5.1. We find that the energy differences between the PL peak energy related to type-II transition and the band gap of the GaAs barrier are 87 meV (Δ_2)and 49 meV (Δ_1) for 1.43 MLs and 0.95 MLs thick ultrathin QWs, respectively as illustrated in Fig. 5.7, where a band diagram for InP/GaAs type-II ultrathin QW is schematically drawn. Situation for thick and thin ultrathin QW is shown by dotted and solid line, respectively. Type-II transitions observed in the PL spectra (Fig. 5.1) of the ultrathin QWs are shown by arrows in Fig. 5.7. As mentioned above, the exciton binding energies for the type-II systems are very small (like 1.5 meV for InP/GaAs QDs). Hence, activation energy determined from the integrated PL intensity versus temperature can not only be related to the dissociation of excitons but there may be other mechanisms which are

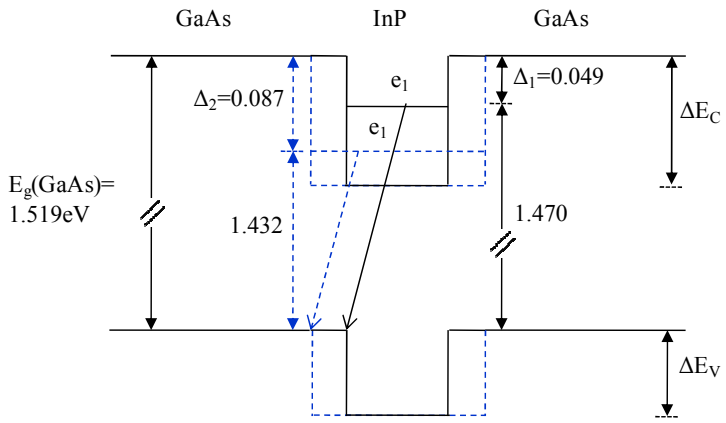

Figure 5.7: Schematic of the type-II band alignment for InP/GaAs ultrathin QWs indicating the confined electronic level in the conduction band of InP. Situations for the thick and thin ultrathin QW cases are shown with the dotted and solid lines respectively. Observed type-II transitions in the PL spectra are shown by arrows. Δ_1 and Δ_2 are the energy separation between the PL peak energy of the QW and the band gap of the GaAs barrier for thin and thick QW. All values given corresponds to low temperature (10 K) and is in the unit of eV.

responsible for the decrease in PL intensity with the temperature. It is interesting to note that the values of activation energies for both ultrathin QWs are close to the energy difference between the PL peak energy and the band gap of the GaAs barrier for the corresponding ultrathin QWs. Therefore, it is determined that the thermal escape of carriers from the QW into the barrier region is the main cause of the PL quenching with temperature for InP/GaAs ultrathin QWs. This fact is also supported by the observations made from Fig. 5.2(a) and Fig. 5.2(b) that the PL intensity related to the GaAs barrier layer gradually increases with increase in temperature.

5.6 Summary

We have analysed the temperature dependence of the PL spectra for MOVPE grown InP/GaAs ultrathin QWs. Cross-sectional TEM imaging for 1.43 MLs thick

ultrathin QW confirms that only ultrathin QW exists in the sample. We observe PL up to near room temperature from the 1.43 MLs thick ultrathin QW, while PL from 0.95 MLs thick ultrathin QW could not be detected above 165 K. The Bose-Einstein empirical relation has been used to analyze the temperature dependence of the PL peak energies of the ultrathin QWs. It has been found that the temperature dependence of the transition energies for the InP/GaAs ultrathin QWs is similar to the temperature dependence of the band gap for GaAs barrier layer. Activation energies obtained from the Arrhenius like plot of integrated PL intensity correspond to the difference between the PL peak energy related to type-II transition and the band gap of the GaAs barrier layer. Thus, the thermal escape of the carriers from the ultrathin QW into the GaAs barrier is mainly responsible for the PL quenching with temperature, which is also supported by the observation that PL intensity related to the GaAs barrier layer increases with increase in temperature.

Chapter 6

Growth and structural characterization of strained and partially relaxed InP/GaAs type-II quantum well superlattices

6.1 Introduction and background

InP/GaAs material system is important because optical transition energy of their quantum structures falls in the technologically important near infrared wavelength region [6,100,103]. Therefore, various quantum structures like ultrathin QWs [169–171] and QDs [11, 100, 103] have been grown and their structural, optical, and electrical properties are studied. In spite of this, we do not find any study dealing with the growth and characterization of superlattice structures for this material combination. There exist extensive reports on the growth and characterization of strained layer superlattice structures based on various material combinations like InAs/GaAs [14], InAs/InP [172], InAs/GaSb [173], and GaP/AlP [174] due to their fundamental properties as well as their applications in the opto-electronic devices. Lattice mismatch between constituent layers plays a very crucial role in determining the strain status of the superlattice structures. It not only puts an upper limit on the thickness, known

as critical layer thickness, of individual layers but also on the total thickness of the pseudomorphically grown superlattice structure. When either of the two exceeds beyond the critical value, the strain is relieved through the formation of misfit dislocations, defects and this leads to poor crystalline quality of the grown structures. In addition to this, surface morphology has been found to have a direct correlation with the strain status of epitaxial structures. Various surface morphologies like three dimensional 3D growth and cross-hatched pattern formation for the partially relaxed epitaxial layers have been reported in the literature [175, 176]. It is to be noted that the InP/GaAs material system has a large lattice mismatch of about 3.8%. Hence, the study of strain status and surface morphology of strained InP/GaAs superlattice structures is essential for the realization of opto-electronic devices based upon this material combination.

In this chapter, the structural properties of superlattice structures of InP/GaAs grown using MOVPE technique are discussed. Strain is easily accommodated in InP ultrathin QWs for larger thickness of GaAs barrier layers, thus demonstrating pseudomorphic growth for superlattice structures. However, superlattice structures show partial relaxation due to the coupling of strain of individual QWs for relatively thin GaAs barrier layer thickness. Thickness undulations in GaAs barrier layers are observed for partially relaxed superlattice structures, which degrade the surface morphology.

6.2 Growth and Experimental details

InP/GaAs superlattice structures are grown in a horizontal MOVPE reactor (AIX-200) with a rotating substrate holder on nominally (0 0 1) oriented n^+-GaAs

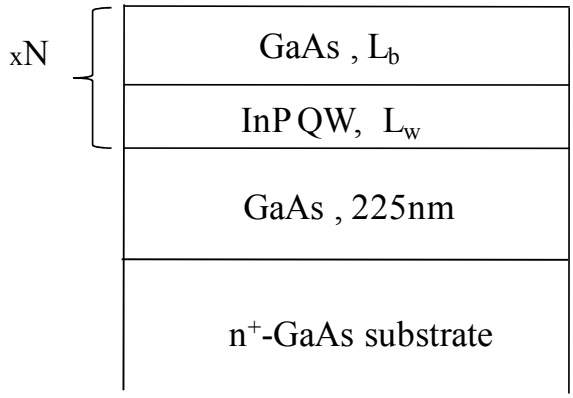

Figure 6.1: Schematic layer structure of the superlattice samples indicating the InP QW, GaAs barrier layer, and the superlattice period. L_w, L_b are the thickness of the QW and barrier layer respectively and N is the superlattice period.

substrate at 50 mbar of reactor pressure. Trimethyl gallium (TMGa) and trimethyl indium (TMIn) are used as the precursors for group-III elements, while 100% arsine (AsH_3) and phosphine (PH_3) are used as the precursors for group-V elements. All the superlattice samples are grown at 600^0C with a V/III ratio of ∼100 for the GaAs layers and ∼250 for the InP QW. The typical layer structure for the superlattice samples is shown in Fig. 6.1, which consists of ∼225 nm thick GaAs buffer layer, InP QW and GaAs barrier layer, N is the superlattice period. Various superlattice samples have been grown by varying InP QW width (L_w), GaAs barrier width (L_b) and N, which are summarized in the Table 6.1.

Crystalline and interfacial quality of grown superlattice samples have been evaluated by using $\omega/2\theta$ scans in HRXRD measurements; $\omega/2\theta$ rocking curves are carried out by using a PANalytical X'Pert Pro MRD diffractometer, equipped with a Hybrid monochromator (PANalytical model Hybrid 4x), with a beam divergence of about 18 arc-second in the scattering plane for CuK_{α_1} x-rays (λ=1.5406 Å). All the $\omega/2\theta$ rocking curve measurements are done with a 0.75^0 open detector parallel to the scattering

Table 6.1

Sample No	t_w (Sec)	t_b (Sec)	N	L_w (Å)	L_b (Å)	Relaxation	Average roughness (Å)
SL1	6	30	7	1.8	45	fully strained	1.0
SL2	8	30	7	2.5	46	fully strained	1.0
SL3	10	30	7	3.3	46	fully strained	1.0
SL4	10	30	11	3.3	45	fully strained	1.0
SL5	10	30	30	3.3	45	fully strained	1.0
SL6	10	10	30	3.3	15	0.6%	5.4
SL7	15	10	50	5.6	15	0.6%	8.6
SL8	18	10	50	6.8	15	5.9%	106.2

Table 6.1: Growth duration of the InP QW (t_w) and the GaAs barrier layer (t_b), superlattice period N; thickness of QW (L_w) and barrier layer (L_b) as well as the magnitude of relaxation determined from HRXRD, and surface roughness evaluated from AFM measurements.

plane. Strain status of the QW layer is examined by performing the RSM in a triple axis geometry, which consists of a hybrid monochromator at the input side and a Ge (2 2 0) two-crystal three-bounce monochromator before the detector. The acceptance angle for the three bounce Ge (2 2 0) monochromator before the detector is about 12 arc-second. RSM is obtained by measuring a series of $\omega/2\theta$ scans each having a different ω offset. Such maps of asymmetric reflection enables us to assess the relaxation in the superlattice structure. Superlattice parameters namely the thickness of QW and barrier layer are measured from the HRXRD measurements by matching the experimental diffraction pattern with simulated ones using the Takaji-Taupin equations implemented in the commercial software:X'pert epitaxy. Cross-sectional TEM measurements are performed to determine the presence of dislocations and 3D growth in partially relaxed superlattice structures. Surface morphology of the superlattice samples is assessed by using AFM technique. AFM measurements are carried out using a multimode scanning probe microscope (NT-MDT, SOLVER-PRO). Sili-

con cantilever tips having a radius of curvature of ∼10 nm, resonant frequency ≥190 KHz and spring constant ∼5.5 N/m were used in non-contact mode for the AFM measurement.

6.3 Structural properties: HRXRD results

Figure 6.2(a), Fig. 6.2(b) and Fig. 6.2(c) show the experimental HRXRD rocking curves for (0 0 4) symmetric reflection from the superlattice samples SL1, SL2, and SL3, respectively. These superlattice samples have been grown by increasing the growth duration for the InP QW, while maintaining a constant flow of TMIn source. This results in the increasing thickness of InP QW for samples SL1, SL2 and SL3. The other parameters of superlattice structure like thickness of the GaAs barrier layer and N have been kept constant as shown in Table 6.1. We observe zeroth order (S_0) satellite peak for all the superlattice structures as can be seen from Fig. 6.2. First order (S_1, S_{-1}) satellite peaks are very weak for superlattice samples SL1 and SL2, while they are clearly observed for superlattice structure SL3 that has the highest QW thickness. These satellite peaks (S_0, S_{-1}, and S_1) originate due to the artificially created periodicity of QW structures along the growth direction as can be seen from Fig. 6.1. Additionally, N-2 interference fringes between superlattice peaks S_0 and S_{-1} are very weak for superlattice structures SL1 and SL2. This is because these samples (SL1 and SL2) consist of InP QWs that are comprised of monolayer high islands for submonolayer coverage (<1 MLs) as discussed in **chapter 3**. Thus, the lateral inhomogeneity caused by the partial surface coverage leads to weak interference fringes in the rocking curves of superlattice structures (SL1 and SL2) as can be noted from the Fig. 6.2(a) and Fig. 6.2(b). On the other hand, N-2 interference fringes are visible

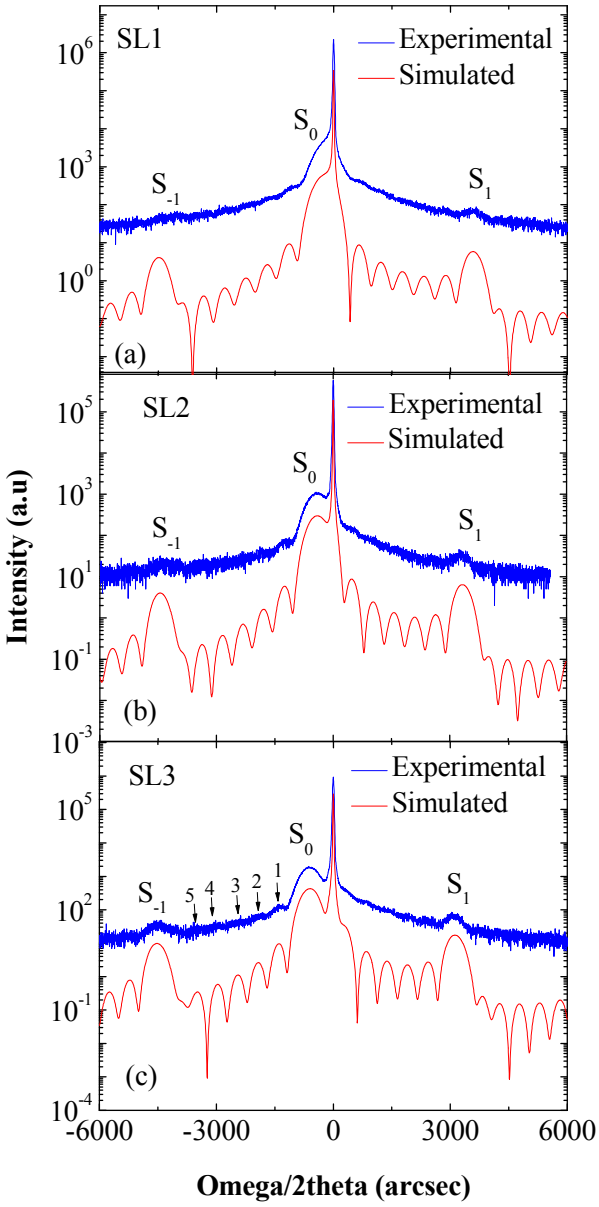

Figure 6.2: Experimental and simulated HRXRD profile for (0 0 4) symmetric reflection of InP/GaAs superlattice structures a) SL1, b) SL2, and c) SL3 having different thickness of InP QW. N-2 interference fringes have been marked for sample SL3. Simulated profiles have been shifted vertically for clarity in viewing.

for superlattice structure SL3 in the rocking curves (Fig. 6.2). Observations of the superlattice peaks (S_0, S_1, S_{-1}) and N-2 interference fringes between them in the experimental HRXRD rocking curves confirm high crystalline and interfacial quality of the grown superlattice samples. We note that the FWHM of the S_0 peak decreases

and its intensity increases with increase in the InP QW thickness, which is consistent with the diffraction theory [177]. Simulated HRXRD profiles for SL1, SL2 and SL3 samples are also shown in Fig. 6.2(a), Fig. 6.2(b), and Fig. 6.2(c), respectively. We observe a nice matching between experimental and simulated HRXRD profiles for the superlattice samples as is evident from Fig. 6.2. The thickness of InP QW obtained from the simulation is 1.8±0.1 Å, 2.5±0.1 Å and 3.3±0.1 Å, while the thicknesses of GaAs barrier layers are 45±2 Å, 46±2 Å, and 46±2 Å for superlattice samples SL1, SL2 and SL3, respectively as shown in Table 6.1. It is to be noted that the QW thickness obtained from the simulation for superlattice samples SL1 and SL2 that have submonolayer QW thickness represents the effective coverage of InP QW, because QWs for sub monolayer (<1ML) coverage of InP are comprised of monolayer high islands with their lateral extent lesser than the exciton radius [143,144]. Growth rate of InP QWs is determined from the measured values of QW thickness and the respective growth duration and is plotted in Fig. 6.3. The experimental data can be nicely fitted with a straight line yielding a growth rate of ∼0.4 Å/sec.

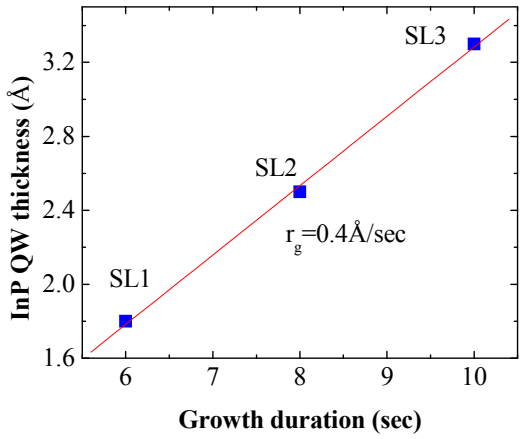

Figure 6.3: Measured values of InP QW thickness as a function of growth duration. r_g denotes the growth rate.

Next, we analyze the structural properties of the superlattice samples by increasing the superlattice period N, while keeping the thicknesses of InP QWs and GaAs barrier layers constant. Figure 6.2(c) and Fig. 6.4 depict the experimental HRXRD rocking curves for the superlattice samples SL3, SL4, and SL5 with a N value of 7, 11, and 30, respectively. Observation of superlattice peaks (S_0, S_1, S_{-1}) and N-2 interference fringes in the HRXRD pattern of sample SL4 indicates the high crystalline and interfacial qualities once again. However, we do not observe the N-2 interference fringes for SL5 which has N=30. This is due to the superposition of interference fringes that can not be resolved due to the experimental limitations. It is also evident from Fig. 6.2(c) and Fig. 6.4 that the intensity of S_0, S_1, S_{-1} peaks is also growing and its FWHM is reducing with increasing N value, which is also consistent with the diffraction theory [177]. These observations indicate that the superlattice samples have maintained their crystalline and interfacial quality up to N=30. The thicknesses of InP QW and GaAs barrier layers obtained from the simulation of HRXRD profiles are listed in Table 6.1. Strain status of these superlattice samples is evaluated from the RSM of (2 2 4) asymmetric reflection. Figure 6.5 shows such a plot for the sample SL5, which has N=30. We note that the S_0 feature from the superlattice structure lies on the vertical line that passes through the GaAs substrate feature along the $Q_\perp$ direction. This observation, as discussed in the section 2.3 of **chapter 2**, confirms that the superlattice sample SL5 is pseudomorphically grown on the GaAs substrate without any signature of relaxation. Hence, it is understood from the rocking curves and RSM results in HRXRD measurements that the superlattice sample SL5 having N=30 is fully strained and has good crystalline and interfacial quality.

Figure 6.6(a), Fig. 6.6(b) and Fig. 6.6(c) show the experimental rocking curves

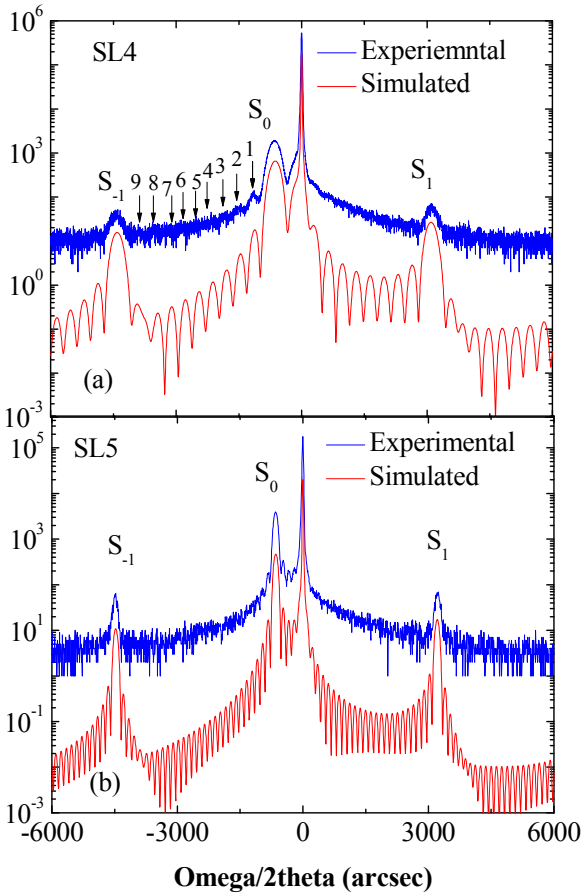

Figure 6.4: Experimental and simulated HRXRD profile for (0 0 4) symmetric reflection of InP/GaAs superlattice structures a) SL4, and b) SL5 having different superlattice periods (N). N-2 interference fringes have been marked for sample SL4. Simulated profiles have been shifted vertically for clarity in viewing.

from (0 0 4) symmetric reflection for the superlattice samples SL6, SL7 and SL8, respectively. Sample SL6 has been grown by keeping InP QW thickness of 3.3 Å, GaAs barrier layer of 15 Å and superlattice period of N=30. It is noted that the S_0 peak of SL6 sample is quite broad and also the interference fringes around the S_0 peak are not clearly visible. These observations indicate that the interfacial quality of the superlattice sample SL6 is poor. It is also reflected from Fig. 6.6(a), when the simulated curve is compared to the experimental rocking curve. We do not find a reasonable match between experimental and simulated profile for the estimated thickness of InP QW (3.3 Å) and GaAs barrier layer (15 Å) as clearly shown in

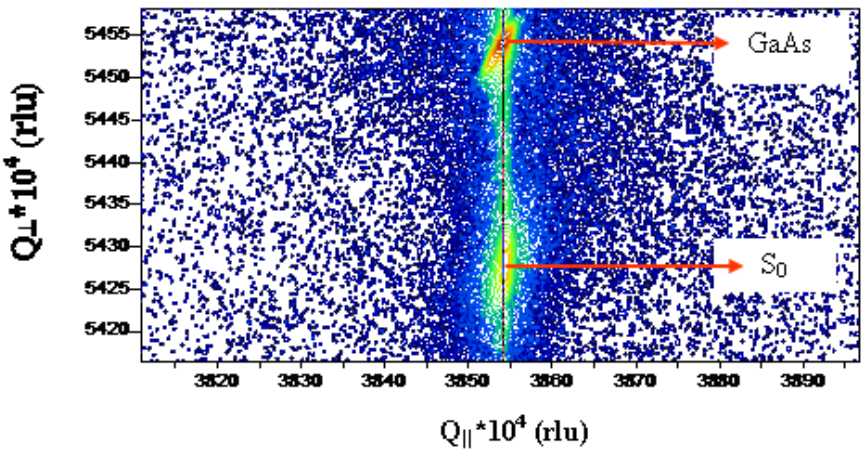

Figure 6.5: Reciprocal space map of SL5 structure from (2 2 4) asymmetric reflection. Features from GaAs and superlattice structure are marked as GaAs and S_0 respectively. "rlu" denotes reciprocal lattice unit.

Fig. 6.6(a). However, a nice match is observed for a value of 2.8 Å for the InP QW and 15 Å for the GaAs barrier layer. The measured thickness of InP QW is lower than the estimated value obtained from the QW growth rate shown in Fig. 6.3. We make similar observations for the other two samples SL7 (InP QW=5.6 Å, GaAs barrier=15 Å) and SL8 (InP QW=6.8 Å, GaAs barrier=15 Å) as evident from Fig. 6.6(b) and Fig. 6.6(c). For both the samples, we do not find a nice agreement between the experimental profile and the simulated one with the superlattice parameters obtained using the growth rate. Thus, the rocking curve measurements indicate that the crystalline and interfacial quality of the superlattice samples SL6, SL7, and SL8 is poor. Now, it becomes essential to evaluate their strain status. For this purpose, we have performed RSM measurements of (2 2 4) asymmetric reflection for SL6, SL7, and SL8 superlattice samples. We note that the S_0 feature of the superlattice sample, SL6, does not appear on the vertical line passing through the GaAs substrate feature in the $Q_\perp$ direction but it is slightly shifted to left hand side as shown in

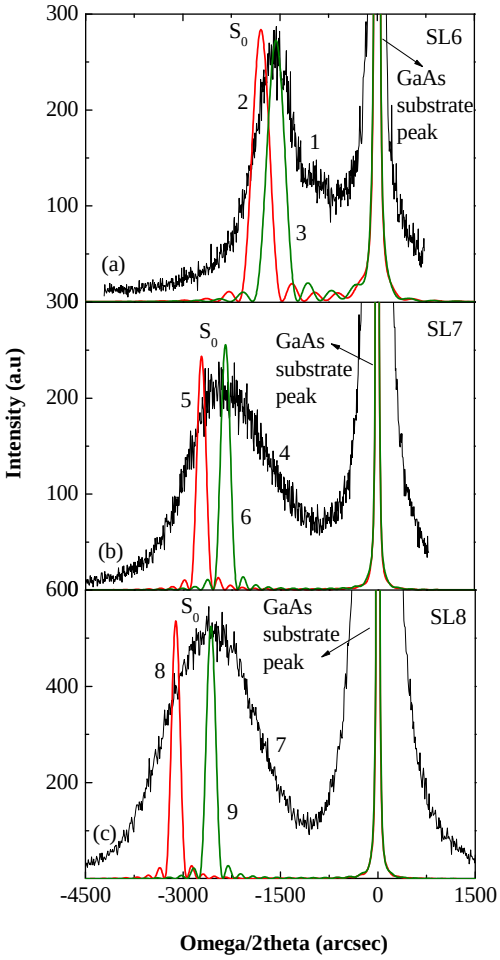

Figure 6.6: HRXRD rocking curves for (004) symmetric reflection of partially relaxed superlattice samples a) SL6, b) SL7, and c) SL8; 1, 4 and 7 denote the experimental HRXRD profile for SL6, SL7 and SL8 superlattice structures, 2 and 3 denote the simulated profiles with L_w=3.3 Å, L_b=15 Å and L_w=2.8 Å, L_b=15 Å, 5 and 6 denote the simulated profiles with L_w=5.6 Å, L_b=15 Å and L_w=4.6 Å, L_b=15 Å, and 8 and 9 denote the simulated profiles with L_w=6.8 Å, L_b=15 Å and L_w=5.2 Å, L_b=15 Å, respectively. Intensity axis for all the graphs has been enlarged for clarity in viewing the superlattice peak (S_0).

Fig. 6.7(a). The RSM plot for sample SL7 is similar to that of SL6 (not shown here), while it is very different for sample SL8 as shown in Fig. 6.7(b). The S_0 feature for SL8 is clearly shifted with respect to the GaAs feature. This observation shows that these superlattice samples are not fully strained but possess some relaxation, which degrades their crystalline and interfacial quality that is also indicated in the rocking

curve measurements. It is also observed that the deviation of S_0 peak from the vertical line for samples SL6 and SL7 is very small indicating onset of the relaxation process leading to very small relaxation values for these samples, while it is relatively large for sample SL8 confirming a clear relaxation of grown superlattice structure. The procedure of determination of relaxation from the RSM plot has been very well described in the literature [178,179]. First, parallel mismatch ($\epsilon_{||}$) and perpendicular mismatch ($\epsilon_{\perp}$) are determined from RSM plot and then the relaxation is defined as the ratio of parallel mismatch to the bulk mismatch. Using this procedure, the relaxation values for samples SL6, SL7, and SL8 are determined to be 0.6 %, 0.6 %, and 5.9 %, respectively within the error bar of ±0.3 %.

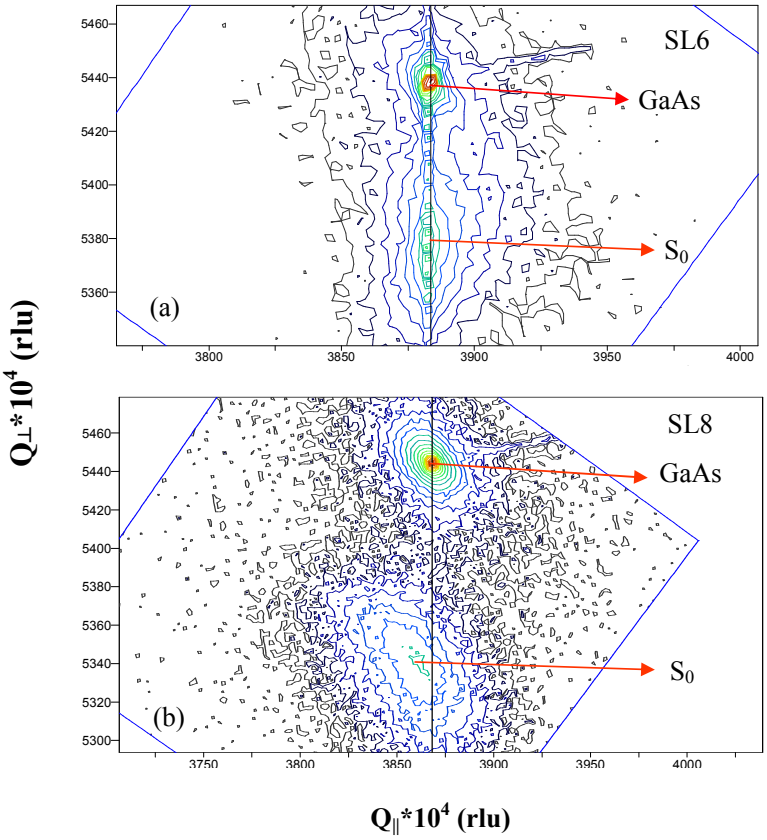

Figure 6.7: Reciprocal space map from (2 2 4) asymmetric reflection for a) SL6, b) SL8 superlattice structures. Features from GaAs and superlattice structure are marked as GaAs and S_0 respectively. "rlu" denotes reciprocal lattice unit.

6.4 Cross-sectional TEM results

Crystalline and interfacial qualities are assessed by using cross-sectional TEM measurements. Figure 6.8 shows such TEM micrographs of the fully strained (SL5) and the partially relaxed (SL6 and SL8) superlattice structures. Low resolution micrograph of fully strained superlattice structure (SL5) shows InP QWs as black thin lines separated by GaAs barrier layers as white bands in Fig. 6.8(a). The period thickness (L_w+L_b) as obtained from this TEM micrograph is about 50 Å, which corroborates with the value that obtained from the HRXRD measurements for this sample as shown in Table 6.1. Figure 6.8(b) shows the high resolution image of the same superlattice sample displaying the atomic arrangement of GaAs barrier layers. However, we are unable to see any contrast change corresponding to highly strained InP QWs, that are only one monolayer thick, because of the instrumental resolution. Apart from this, no dislocations are observed for the superlattice structure SL5, which is expected because this sample is fully strained as is observed from the RSM of (2 2 4) symmetric reflection of this sample (Fig. 6.5). Figure 6.8(c) shows the low resolution image from the partially relaxed superlattice sample SL6, where InP QWs (marked by arrows) separated by GaAs barrier layers are observed. It is to be noted that this sample has same thickness of the InP QW as that of sample SL5. But thickness of GaAs barrier layer (15 Å) is lower than that of sample SL5. The determined period thickness for this superlattice structure is about 18 Å, which is again in agreement with that determined by the HRXRD as can be noted from the Table 6.1. Surface of the superlattice sample shows thickness undulations as observed from the low resolution TEM micrograph shown in the encircled area of

Fig. 6.8(c). It is further noted that signature of InP QWs can be observed with a feeble contrast in the high resolution TEM image as shown in Fig. 6.8(d) and are marked by arrows. However, we do not observe any signature of dislocations in the superlattice structure although HRXRD indicated a partial relaxation as confirmed from the RSM measurements for this sample. Low resolution TEM micrograph for sample SL8 is depicted in Fig. 6.8(e), where individual InP QWs separated by GaAs barrier layers are clearly observed. This superlattice structure has the highest thickness of InP QW, which leads to the larger relaxation (5.9 %). The surface of this sample also shows the thickness undulations similar to the sample SL6, which are very clearly shown in the encircled area in the inset of Fig. 6.8(e). InP ultrathin QWs separated by GaAs barrier layers are clearly observed with larger contrast in the high resolution TEM image as depicted in Fig. 6.8(f). The period thickness evaluated from the high resolution image is about 20 Å, which is closely matching with the value obtained from the HRXRD. It is interesting to note that the thickness of GaAs barrier layer has fluctuations as indicated by the arrows at several places in the high resolution image. This is important in view of the fact that no QD strcutures have really been grown. We do not observe dislocations for this superlattice structure also, although this sample shows the largest relaxation among the superlattice structures. Thus it is confirmed that these InP/GaAs superlattice structures show initial stages of relaxation process without introducing appreciable dislocations and formation of 3D islands. It is also important to note from the high resolution cross-sectional TEM image shown in Fig. 6.8(f) that the InP ultrathin QWs have sharp interfaces.

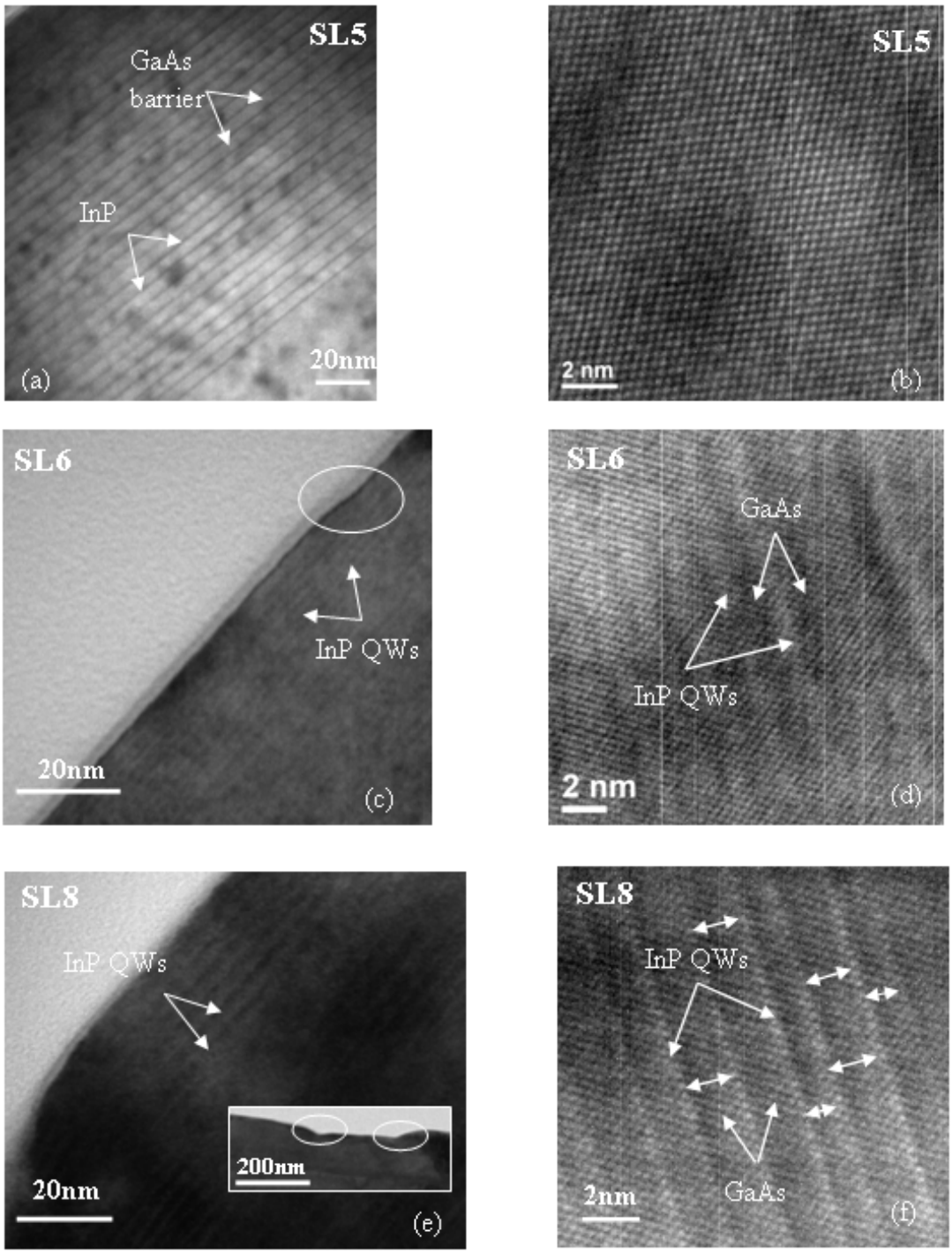

Figure 6.8: Cross-sectional low resolution TEM micrographs for superlattice structures a) SL5, c) SL6 and e) SL8. Corresponding high resolution images for superlattice samples b) SL5, d) SL6 and f) SL8. Inset shows the low resolution image for sample SL8 indicating surface undulations. Thickness undulations in GaAs barrier layer in high resolution image for sample SL8 are marked by arrows.

6.5 Surface morphology

We noticed strain driven larger thickness undulations in TEM micrographs for samples SL6 and SL8. It has been observed in literature that the lattice relaxation process may introduce undulations in the surface morphology of epitaxial structures. Further, HRXRD measurements revealed that the superlattice structures SL6, SL7, and SL8 are partially relaxed. However, AFM technique is preferred to investigate the surfaces morphology. We, therefore, carried out the AFM measurements on all the superlattice samples. Surfaces of all fully strained superlattice samples (SL1, SL2, SL3, SL4, and SL5) are atomically smooth as indicated by the value of thier average roughness listed in the Table 6.1. Figure 6.9 shows the 2D surface topography of the four representative superlattice samples SL5 (fully strained) and partially relaxed (SL6, SL7, and SL8). We note that the surface morphology is atomically smooth for sample SL5, which is fully strained. However, the surface morphologies for the partially relaxed superlattice samples SL6, SL7, and SL8 are significantly different when compared with the sample SL5. Surfaces of these samples show undulations and the surface roughness is continuously increasing with the QW thickness (samples SL6, SL7, and SL8). It is interesting to note that the surface morphology is quite distinct for superlattice samples SL6 and SL7, although the relaxation value for these samples is very small (0.6 %) and no clearly dinstiguishable change is seen in the RSM measurements. This observation indicates that the surface morphology is very sensitive to the strain status of the superlattice structure, where the surface roughness seems to accelerate with the degree of relaxation.

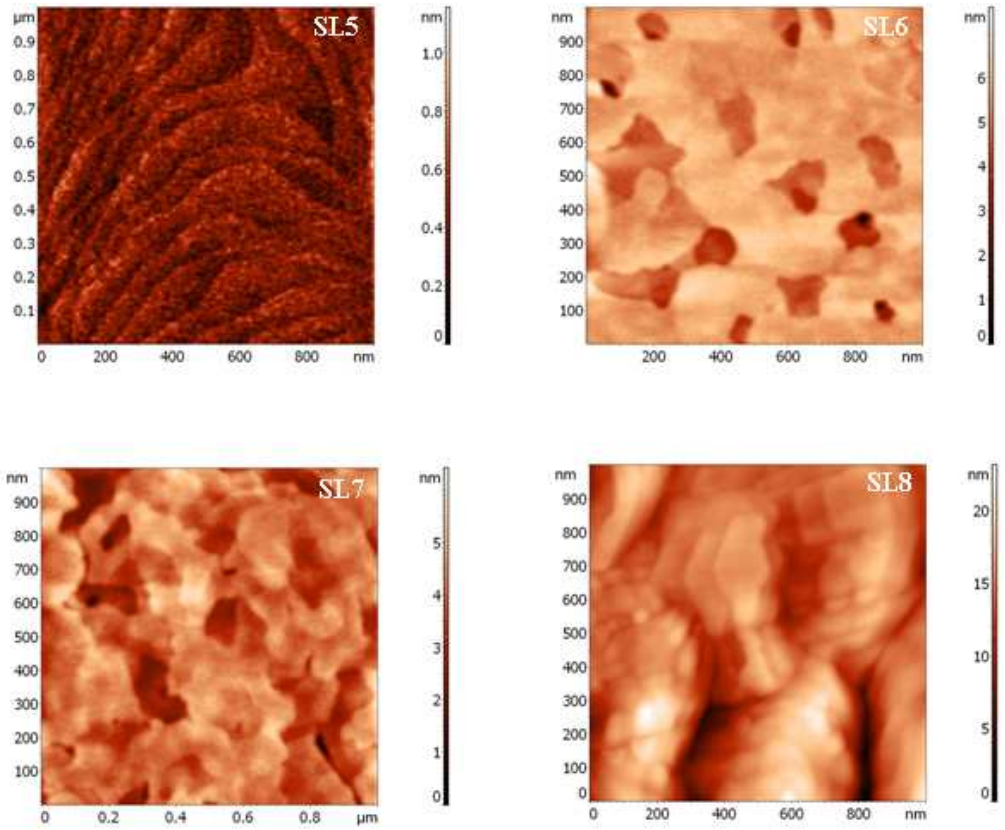

Figure 6.9: Surface morphology for the strained (SL5) and partially relaxed (SL6, SL7, and SL8) superlattice samples obtained from the AFM measurements.

6.6 Discussion

The strain energy is easily accommodated in the InP QW layer for the thick barrier layers of GaAs and the resulting superlattice structures SL1, SL2, SL3, SL4, and SL5 are fully strained and their surfaces are atomically flat despite a large lattice mismatch of about 3.8 % between InP and GaAs. However, when the GaAs barrier layer thickness is decreased from 45 Å (sample SL5) to 15 Å (sample SL6) for the same thickness of the InP QW, the strain fields in the adjacent InP QWs are coupled and lead to an onset for the relaxation process as observed in the HRXRD measurements. Additionally, coupling of strain field of individual InP QW induces undulations in the GaAs barrier layer thickness, which degrades the surface morphology without

forming QD structures as observed in cross-sectional TEM and supported by AFM measurements. The strain energy in InP QW increases with increase in InP QW thickness from 3.3 Å (sample SL6) to 6.8 Å (sample SL8) and strain field of the QWs couples efficiently for reduced GaAs barrier layer thickness of 15 Å that leads to increase in the undulations in the GaAs barrier layers as clearly noted in the high resolution image for sample SL8 (Fig. 6.8(f)). Large undulations in the thickness of GaAs barrier layers introduced by the higher InP QW thickness result in an increased surface roughness of the partially relaxed superlattice structures as observed in the AFM measurements.

6.7 Summary

InP/GaAs QW superlattice structures are grown by MOVPE technique and their structural and surface morphology have been analyzed by using HRXRD, TEM and AFM measurements. Crystalline and interfacial quality of superlattice structures is nice for thick barrier layers of GaAs, thus confirming the pseudomorphic growth. However, for thin GaAs barrier layers, the interfacial and crystalline quality of the superlattice samples is poor, which show partial relaxation without introducing any appreciable dislocations in the structures. Strain induced undulations in the GaAs barrier layers are observed for superlattice structures with relatively thicker InP QWs and thinner GaAs barrier layers. Such undulations seem to propagate upto the surface of the superlattice structures and degrade the surface morphology of the partially relaxed superlattice structures.

Chapter 7

Optical properties of InP/GaAs type-II quantum well superlattice structures

7.1 Introduction and background

Various QW and QD superlattice structures have been investigated in the literature for the detector and solar cell applications [180–183]. Keeping this in mind, we have grown fully strained and partially relaxed InP/GaAs type-II QW superlattice structures by MOVPE technique. Their structural properties and surface morphology have been studied in detail as discussed in **chapter 6**. In this chapter, optical properties of InP/GaAs type-II QW superlattice structures are discussed. A systematic study of optical properties is essential for the realization of optoelectronic devices like near infrared laser diodes, infrared photo detectors and solar cells based on this material combination.

Apart from this, temperature dependence of the band gap (GS transition energy) for bulk semiconductors (quantum structures) provides important information about the electron phonon interaction [79]. It has been seen that the GS transition energy for thick QWs follows the temperature dependence of the band gap of relevant bulk

material [160,161]. On the other hand, temperature dependence of the GS transition energy is considerably modified by the temperature dependence of the confinement potential and follows the band gap variation of barrier material in case of ultrathin QWs [8]. We have found that the temperature dependence of transition energy of InP/GaAs type-II ultrathin QWs follows the band gap variation of GaAs barrier material [170], which was indicated by the PL measurements as discussed in **chapter 5**. However, modulation spectroscopy (PR and ER) is a more powerful technique, which has been extensively used to accurately measure the transition energy of thick QWs [85,179], QDs [184,185] and even ultrathin QWs [8]. SPS is another technique available in the literature, which is also based on optical absorption measurements similar to modulation spectroscopic technique. Recently, SPS is applied to study the optical properties of InP/GaAs type-II multiple QDs, where features related to wetting layer and QDs are found at 73 K [186]. However, there is no report of PR, ER and SPS characterization of InP/GaAs type-II quantum structures at room temperature. Therefore, in this chapter, InP/GaAs superlattice structures are characterized by using PR, ER and SPV techniques, where superlattice related excitonic transition is observed in all the strained samples. A thermally active trap level behavior is found in temperature dependent PR measurements. Broadening parameter of superlattice feature in the high temperature region is governed by the scattering of electrons with the LO phonons. It is interesting to note that the built-in electric field in superlattice structure considerably modifies the temperature dependence of superlattice transition energy. For smaller values of electric field, transition energy follows the temperature dependence of band gap of GaAs barrier layer, while it decreases at a faster rate than that of the GaAs material for larger values of built-in

Table 7.1

Sample No	L_w (Å)	L_b (Å)	N	Transition energy (eV)	Broadening parameter (meV)
SL1	1.8	45	7	1.501±1	7.6±1
SL2	2.5	46	7	1.489±1	17.3±1
SL3	3.3	46	7	1.473±1	9.5±1
SL4	3.3	45	11	1.470±1	17.0±1
SL5	3.3	45	30	1.471±1	14.3±1

Table 7.1: Structural parameters like superlattice period N, thicknesses of InP QWs (L_w) and GaAs barrier layer thickness (L_b) of fully strained superlattice structures. Transition energy and broadening parameter of the superlattice feature as determined from the low temperature (10 K) PR measurements.

electric field.

7.2 Experimental procedure

InP/GaAs superlattice structures were grown in a horizontal MOVPE reactor (AIX-200) with a rotating substrate holder on nominally (0 0 1) oriented n^+-GaAs substrate at 50 mbar of reactor pressure as discussed in chapter 6. The structural parameters of studied superlattice structures like InP QW thickness (L_w), GaAs barrier layer thickness (L_b), and the superlattice period (N) are listed in the Table 7.1.

For PR measurements, light from a 100 W quartz tungsten halogen (QTH) lamp dispersed by a 1/4 m monochromator with a 4 nm band pass was used as the probe beam. The chopped laser beam of a He-Ne laser (pump beam) was used to modulate the built in surface electric field of the sample. Change in the reflectivity (ΔR) due to the modulation as a function of wavelength of probe beam was measured by using a lock-in amplifier at the chopping frequency of the pump beam (330 Hz). The dc part of signal from Si photodiode, which is proportional to the reflectivity (R), was also extracted, and the final spectrum ΔR/R was obtained by dividing the

ac signal by dc signal. ER measurements were carried out in soft-contact mode by sandwiching the sample between a flat copper electrode and a transparent conducting glass (TCG) coated with indium-tin-oxide, which acts as the second electrode. The surface electric field was modulated by applying an ac voltage of 1.0 V at a frequency of 180 Hz. Source of probe beam was same as it was for the PR measurements. SPS measurements were performed in the chopped light geometry under soft contact mode [132]. Periodic excess carrier generation and subsequent redistribution changes the surface potential, which was picked up by a TCG electrode. A 100 W quartz-tungsten-halogen lamp along with a 1/4 m SCIENCETECH monochromator was used as the light source. The ac photovoltage signal was measured with a lock-in amplifier.

7.3 Low temperature photoreflectance spectroscopy

Optical properties of fully strained superlattice structures are investigated by carrying out PR measurements at low temperatures (10 K). Energy and broadening parameter of the observed transitions are determined by fitting the experimental PR data by Aspens's line shape function of the following form [187]

$$\frac{\Delta R}{R} = Re\left[Ae^{i\theta}/\left(E - E_0 - i\Gamma\right)^m\right] \tag{7.1}$$

where, A is the amplitude, θ is the phase angle, E is the energy, E_0 is the critical point energy, Γ is the broadening parameter, and m is a fitting parameter, which depends on the nature of critical point. For example, for m=2 Aspens's line shape function is known as a first derivative of Lorentzian line shape (FDLL) which is used to fit the experimental PR data of excitonic transitions [188]. Figure 7.1 depicts

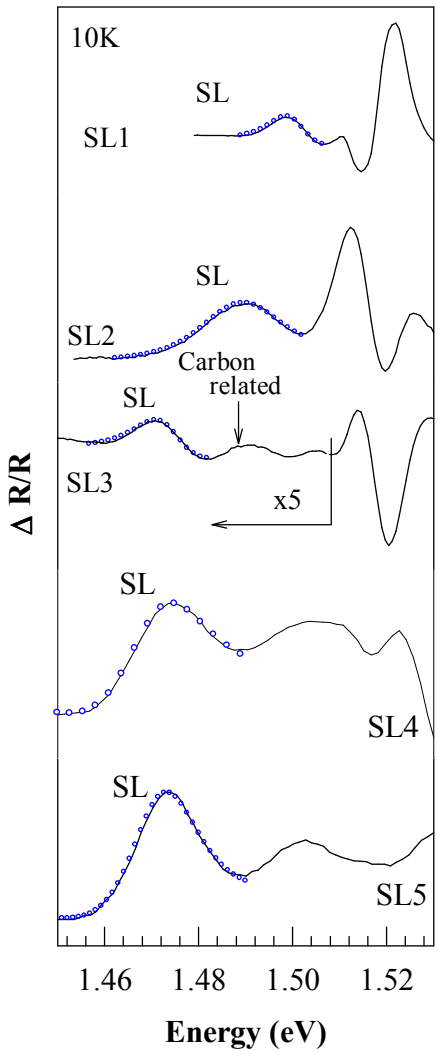

Figure 7.1: The 10 K PR spectra for the fully strained superlattice samples. Data with symbols show the Aspnes line shape fitting. The feature from the superlattice structure is marked as SL.

10 K PR spectra for all the strained superlattice samples showing the well defined superlattice feature marked as SL towards the lower energy side of the GaAs feature seen at ∼1.52 eV. Experimental PR data of the superlattice related features are nicely fitted by FDLL (solid symbols in Fig. 7.1), which indicates that the observed transition is of excitonic nature for all the superlattice samples. Measured excitonic transition energies (broadening parameter) for the superlattice samples SL1, SL2,

SL3, SL4 and SL5 are 1.501 eV (7.6 meV), 1.489 eV (17.3 meV), 1.473 eV (9.5 meV), 1.470 eV (17.0 meV) and 1.471 eV (14.3 meV), respectively as listed in Table 7.1. It is to be noted that the superlattice feature red shifts from 1.501 eV to 1.473 eV with increase in the InP QW thickness from 1.8 Å to 3.3 Å, which is due to the reduced quantum confinement effect in the superlattice structures. This confirms that the observed transition in 10 K PR data is originating from the superlattice structure marked as SL in Fig. 7.2, where band diagram of InP/GaAs type-II superlattice structure has been drawn. Dotted line indicates the situation for the unstrained InP QW, while solid line presents the band line up for the fully strained InP QW. Strained value of 180 meV for the ΔE_C has been reported by us from the C-V measurements on single InP/GaAs type-II QWs [171], which is in agreement with the reported value of ΔE_C by x-ray photoelectron spectroscopy [100, 156]. Unstrained values of band offsets and strained band gaps of heavy and light holes calculated by using the equations reported in the literature [157] are also indicated in the Fig. 7.2. It is found that the measured values of transition energy of the superlattice structure are consistent with the band diagram of the InP/GaAs type-II superlattice structure (Fig. 7.2). It is also noted that the thickness (1.8-3.3 Å) of InP QW has smaller effect on the transition energy of superlattice feature, which may be attributed to smaller values of band offsets in InP/GaAs type-II system as observed from Fig. 7.2. We observe another feature at ∼1.49 eV (marked by an arrow) between superlattice and GaAs features in the PR spectrum of sample SL3. It may either be a higher energy transition from the superlattice structure or a carbon related feature from the MOVPE grown GaAs layers [163]. An overlap of superlattice feature with this peak in sample SL2 might be the reason for its relatively large width seen in PR

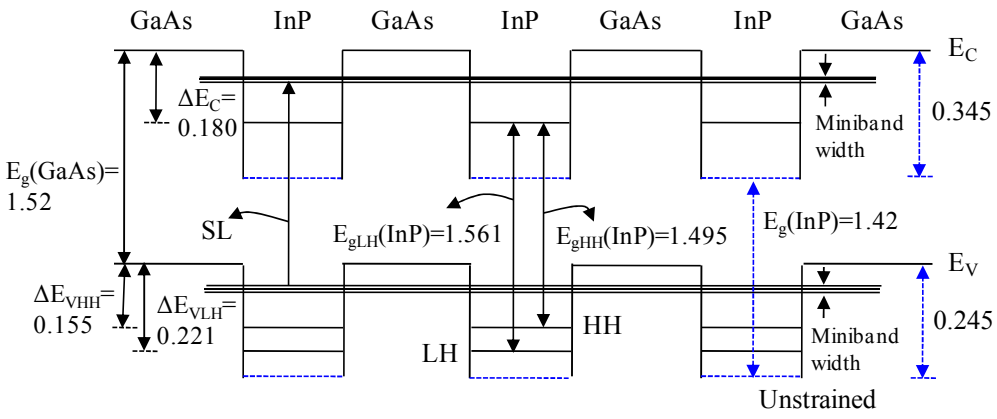

Figure 7.2: Band diagram of InP/GaAs type-II superlattice structure for unstrained and strained InP QWs, shown by dotted and solid lines, respectively. The superlattice feature observed in the PR spectra is marked as SL. Miniband width for both electrons and holes are indicated. All values (at 10 K) are shown in the unit of eV.

spectrum. Superlattice feature from sample SL4 is relatively broad as compared to that of sample SL3 and SL5. It is noted that these superlattice structures have same thickness of InP QW and GaAs barrier layers. But, superlattice period (N) is different and is 7, 11, 30 for SL3, SL4 and SL5, respectively. Hence, larger value of the broadening parameter for SL5 as compared to SL3 is understandable and is due to the larger number of interfaces present in SL5 resulting from the higher number of superlattice period. But the broadening parameter for SL4 having superlattice period value between that of SL3 and SL5 is largest among the superlattice samples. We note that the feature related to GaAs wafer are significantly broadened as compared to sample SL3. Hence, larger broadening parameter of superlattice feature seen in the PR spectrum of SL4 may be attributed to poor quality of the GaAs substrate.

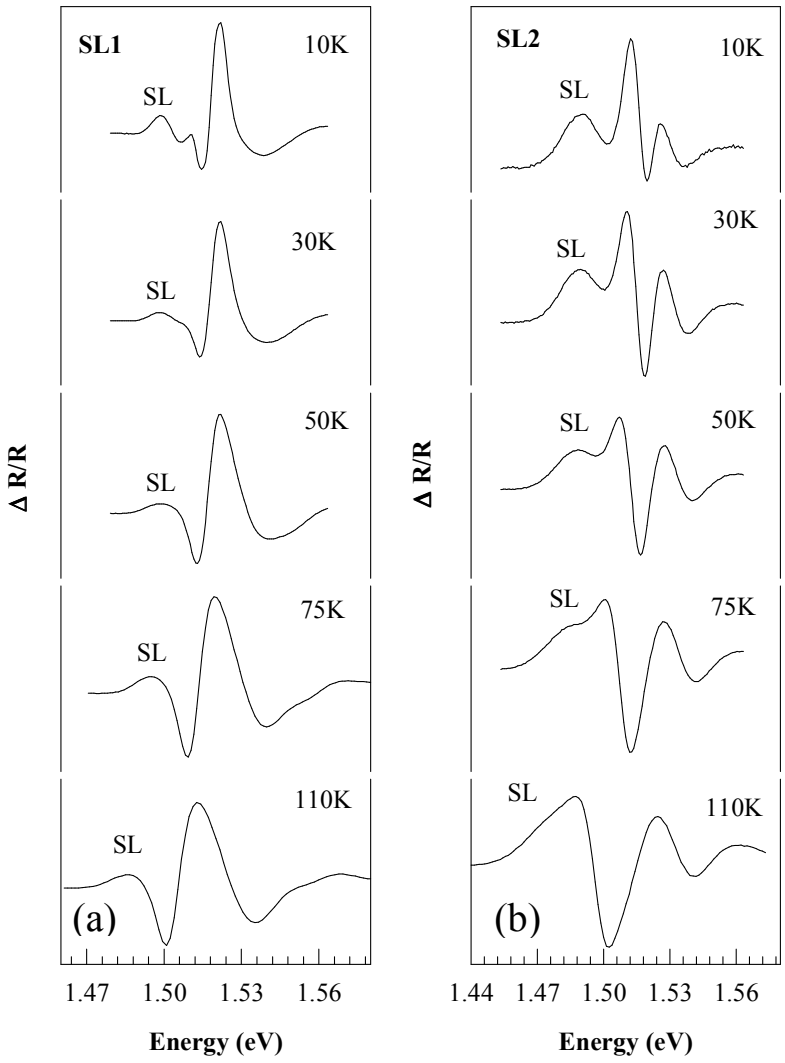

Figure 7.3: Temperature dependence of PR spectra for superlattice structures: (a) SL1 and (b) SL2. Superlattice feature is marked by SL.

7.4 Effect of built-in electric field on temperature dependence of superlattice transition energy

In order to obtain the information about the electron-phonon interaction, we have carried out PR measurements at various temperatures between 10 to 300 K. We note that the superlattice peak is merged with the main GaAs feature when temperature is increased from 10 to 110 K for samples SL1 and SL2 as depicted in Fig. 7.3. Thus

for these two superlattice structures (SL1 and SL2), the information about electron-phonon interaction is difficult to obtain. Therefore, we choose samples SL3 and SL5 to perform the temperature dependent PR measurements, because energy separation between superlattice and GaAs features is relatively large. Temperature dependent PR spectra for samples SL3, and SL5 are shown in Fig. 7.4(a) and Fig. 7.4(b), respectively. We observe the excitonic transition right from low temperature (10 K) upto room temperature (300 K) as is evident from the fitting of PR data with FDLL shown in Fig. 7.4. It is interesting to note from Fig. 7.4(a) that the intensity of the superlattice feature for SL3 relative to GaAs feature is continuously decreasing as the temperature is raised from 10 to 40 K and is not measurable in the 50-130 K temperature range. Thereafter, superlattice feature is again observed from 150 to 300 K and its intensity relative to GaAs feature is monotonically increasing in this temperature range. Such behavior can be understood if some thermally active trap states, introduced due to large strain in the superlattice structure, are considered. These states are frozen at very low temperature (10 K) and starts capturing the photogenerated carriers as the temperature is increased from 10-40 K, hence the corresponding intensity of superlattice feature in this temperature range is found to decrease and finally the superlattice feature disappears in 50-130 K temperature range. As the temperature is further raised from 150 to 300 K, the trapped carriers acquire thermal energy sufficient to overcome the barrier produced by the trap levels that leads to the appearance of superlattice feature again and its intensity starts growing with temperature. However, sample SL5 does not show such kind of a behavior and the superlattice related feature is clearly observed from 10 to 300 K, which will be discussed in the later part of the chapter.

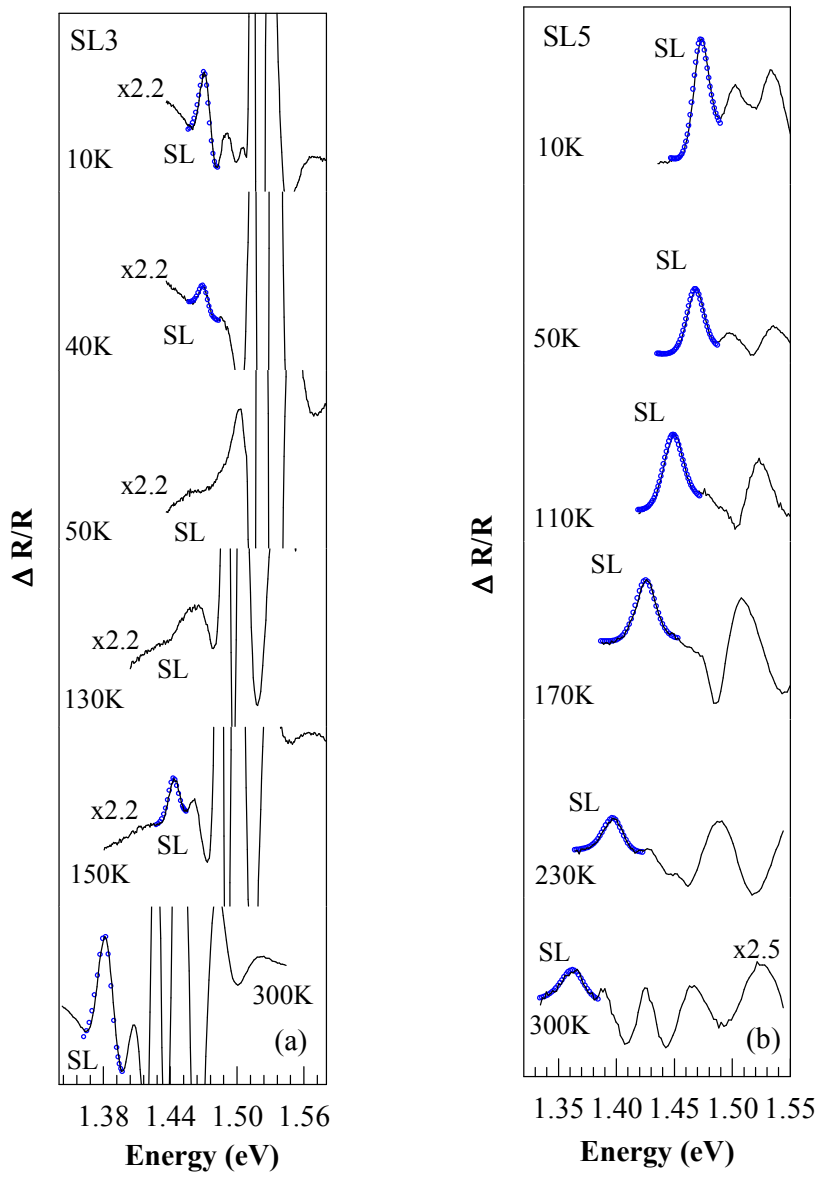

Figure 7.4: Temperature dependence of PR spectra for superlattice structures: (a) SL3 and (b) SL4. Superlattice feature is marked by SL.

Figure 7.5(a) depicts the variation of broadening parameter (Γ) for both the superlattice samples (SL3 and SL5) with $[exp\,(E_{LO}/k_BT) - 1]^{-1}$, which is the LO phonon population density [85]. E_{LO} is the LO phonon energy. Broadening parameter is known to have two components where inhomogeneous broadening is independent of temperature, whereas homogeneous broadening increases with the tempera-

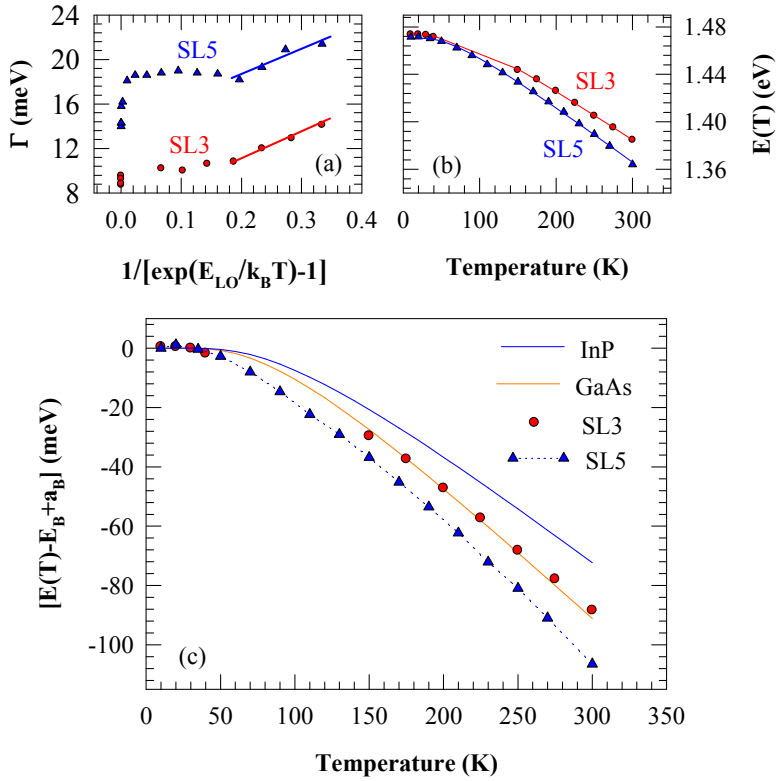

Figure 7.5: (a) Variation of the broadening parameter of superlattice features with the LO phonon population density. (b) Behavior of transition energies of superlattice features with respect to temperature along with the Bose-Einstein fitting. (c) Variation of $E(T) - E_B + a_B$ for superlattices, GaAs, and InP materials as a function of temperature.

ture [185]. It is seen that the inhomogeneous broadening dominates between 10-200 K, while above 200 K the temperature dependent homogeneous broadening governs the width of the superlattice feature. E_{LO} is equal to 36 meV and 43 meV for the GaAs and InP materials, respectively. There is not much difference between the values of E_{LO} for GaAs and InP, thus E_{LO}=36 meV has been taken. Behavior of the broadening parameter for both superlattice structures is similar and it increases linearly with the LO phonon density in the higher temperature region as shown by the line (guide to eye) in Fig. 7.5(a). This indicates that the increase in broadening parameter with temperature is governed by the scattering of electrons with LO

phonons present in the InP/GaAs superlattice. Finally, the temperature dependence of superlattice transition energy has been analyzed by using Bose-Einstein empirical relation (equation 1.8 in **chapter 1**). Figure 7.5(b) depicts the transition energy as a function of temperature for the two superlattice structures. We observe that the transition energy is reasonably fitted by the Bose-Einstein empirical relation and the values of the fitting parameters like E_B, a_B, and θ_{BE} are 1.521 eV, 0.048 eV, 220 K; and 1.513 eV, 0.042 eV, 178 K for SL3 and SL5, respectively. The reported values of a_B, and θ_{BE} for GaAs (InP) materials are 0.060 eV (0.054 eV) and 252 K (274 K) respectively [15]. We find that there is not much difference between the values of a_B, and θ_{BE} for GaAs and InP materials and on the basis of the measured values for superlattice structures we can not unambiguously assign whether the temperature dependence of the superlattice transition energy follows the band gap variation of GaAs or InP. For unambiguous assignment similar to that is performed for single InP ultrathin QW cases in **chapter 5**, the values of $E(T) - E_B + a_B$ for the superlattice samples SL3, SL5, GaAs and InP are plotted as a function of temperature as shown in Fig. 7.5(c). We clearly note that the temperature dependence of the transition energy for the superlattice structure SL3 follows the band gap variation of GaAs. This is expected because GaAs material is present in larger amount than InP in this sample and thus carriers spend most of their time in the GaAs portion of the superlattice structure. This explains the observed temperature dependence of transition energy of superlattice structure, SL3. It is also consistent with our earlier observations [8, 170] made on InP/GaAs and InAs/GaAs ultrathin QWs where the temperature dependence of the GS excitonic transition energy for ultrathin QWs was found to follow the band gap variation of GaAs barrier material. In contrast, the

behavior of transition energy for the superlattice structure SL5 is quite different than that of SL3 as observed from Fig. 7.5(c). It decreases at a faster rate compared to SL3 and GaAs. Further, the energy separation is gradually increasing with temperature that is ∼20 meV at room temperature as noted from Fig. 7.5(c). It is noted that both the superlattice structures have identical thickness of InP QW and GaAs barrier layer. The only difference between the two samples is the different number of superlattice period, N. To find out the reason of such different temperature dependent behavior, room temperature PR spectra from both the samples are shown in the broad energy range in Fig. 7.6, where distinct difference is noted in terms of Franz-Keldysh Oscillations (FKOs) [189, 190], which are observed in the above band gap region of GaAs. The FKOs are much more prominent in SL5 as compared to SL3 indicating that the built-in electric field should be large in magnitude for superlattice structure SL5. The procedure of determining the built-in electric field from the FKOs is very well described in the literature [189, 190]. The extremum of FKOs with the built-in electric field can be expressed as

$$n\pi = \phi + \frac{4}{3}\left[\left(E_n - E_g\right) / \left(\hbar\theta\right)\right]^{3/2} \tag{7.2}$$

where, n is the index of n^{th} extremum, E_n is the energy of n^{th} extremum, E_g is the band gap energy. $\hbar\theta$ is the characteristic energy, which is given by

$$\left(\hbar\theta\right)^{3/2} = \frac{qF\hbar}{\sqrt{2\mu}} \tag{7.3}$$

where, q is the electronic charge, μ is the reduced mass, and F is the built-in electric field. Thus, if we plot $4/3\pi\left[E_n - E_g\right]^{3/2}$ as a function of n, then the slope of straight line is proportional to the electric field. Such a plot for both the samples is shown in the inset of Fig. 7.6. Data are nicely fitted with a straight line yielding the electric

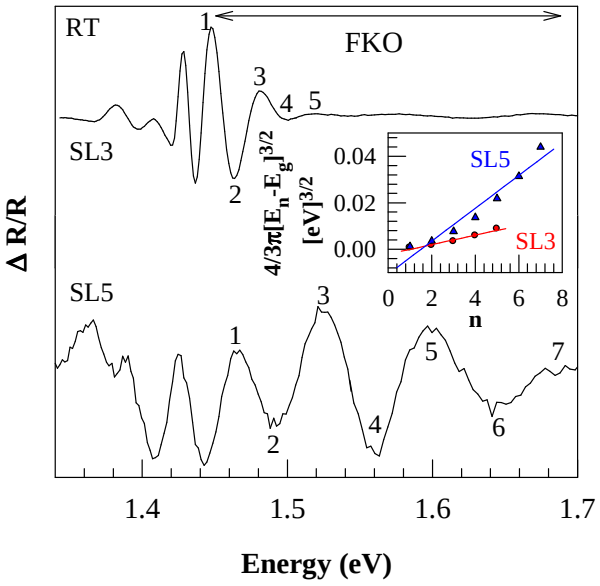

Figure 7.6: Room temperature PR spectra from superlattice structures SL3 and SL5 indicating the FKOs. Inset depicts the graph between $4/3\pi\,[E_n - E_g]^{3/2}$ and n for both superlattices.

field values of 24±2 kV/cm and 90±5 kV/cm for samples SL3 and SL5 respectively at room temperature. It is interesting to note that the built-in electric field increases with the superlattice period. The built-in electric field may be related to the point defects, which trap only one type of carrier. The number of point defects are expected to increase with the superlattice period, which may therefore increase the built-in electric field. Absence of measurable PL signal from most of the superlattice structures also indicate the presence of some defects. However, no information about the point defects is available in TEM measurements because of the instrumental resolution (**chapter 6**). HRXRD also supports a pseudomorphic growth of these superlattice structures. However, presence of point defects can not be ruled out even in HRXRD measurements. Further, it has been reported in an earlier study that the built-in electric field in a GaAs layer decreases with lowering temperature [190]. We also note that the built-in electric field at 10 K in the superlattice structures

SL3 and SL5 is calculated to be 15±2 kV/cm and 71±5 kV/cm respectively. Thus, the built-in electric field in our superlattice structures is found to increase with temperature. It is to be noted that the superlattice structure SL5 has larger electric field as compared to SL3, which is also reflected in the transition energy of sample SL5 at 10 K that is red shifted by ∼2 meV when compared with SL3 as noted from Table. 7.1. The magnitude of the built-in electric field for sample SL3 is too small to provide any detectable red shift even at room temperature and this is the reason that temperature dependence of transition energy for this sample follows the band gap variation of GaAs material. On the other hand, larger magnitude of built-in electric field for sample SL5 and its increase with temperature is responsible for the faster decrease in the transition energy with rise in temperature. As mentioned earlier that the superlattice feature is observed right from 10 to 300 K for sample SL5, while superlattice feature for SL3 shows some localization behavior (Fig. 7.4). It is argued here that although some trap states may be present in the sample SL5 and the photogenerated carriers get trapped in it, the trapped photogenerated carriers can be pulled out from these states due to large built-in electric field present in the sample and these carriers are able to modulate the surface electric field resulting in the observation of superlattice feature in the whole temperature range. Some indication on the presence of trap states in sample SL5 can be made from the Fig. 7.5(a), which shows that the variation of broadening parameters with temperature for both the superlattice feature is similar. Further, it is noted from Fig. 7.4(b) that the intensity of the superlattice feature for SL5 is decreasing with temperature although the built-in electric field is relatively large. This can be related to the presence of large number of non-radiative recombination centres generated by large residual

Table 7.2

Sample No	L_w (Å)	L_b (Å)	N	Transition energy, PR (eV)	Transition energy, ER (eV)
SL5	3.3	45	30	1.365±3	1.368±3
SL6	3.3	15	30	-	1.345±3
SL7	5.6	15	50	-	1.255±3
SL8	6.8	15	50	-	1.235±3

Table 7.2: Structural parameters like superlattice period N, thicknesses of InP QWs (L_w) and GaAs barrier layer thickness (L_b) of fully strained (SL5) and partially relaxed (SL6, SL7, and SL8) superlattice structures. Transition energy of the superlattice feature determined from the room temperature photoreflectance and electroreflectance measurements.

strain due to increased superlattice period. The photogenerated carriers recombine at these non-radiative recombination centers at elevated temperatures, thus reducing the intensity of the superlattice feature.

7.5 Room temperature photoreflectance and electroreflectance spectroscopy

It has been noticed in the previous section that the room temperature PR spectra of the superlattice structures SL3 and SL5 have indicated the presence of superlattice feature alongwith the FKOs in PR spectra at room temperature. Thus, it becomes interesting to perform the room temperature PR and ER measurements of all the superlattice structures in a broad energy range. It is found that the superlattice feature is not observed in the room temperature PR spectra for the samples SL1 and SL2, because it merged with the GaAs feature with rise in temperature as shown in Fig. 7.3. However, superlattice feature is observed in room temperature PR spectra for sample SL3 and SL5 as shown in Fig. 7.4. Transition energy of the superlattice feature at room temperature for samples SL3 and SL5 is 1.385 eV

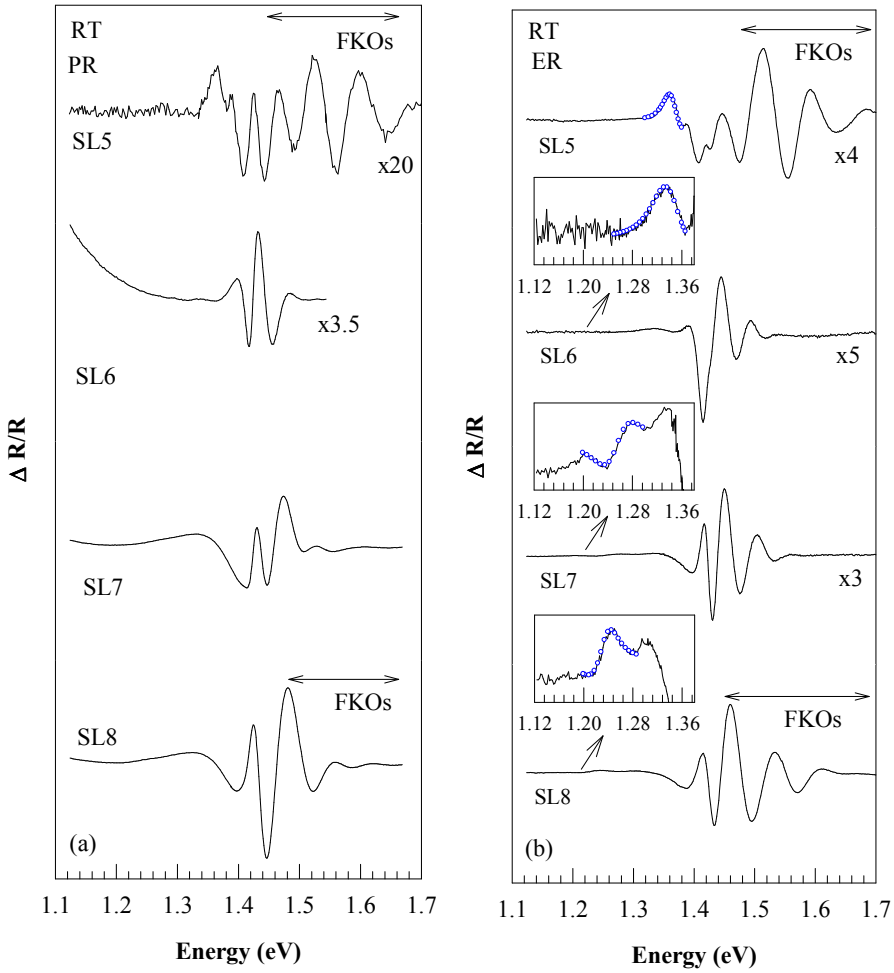

Figure 7.7: Room temperature (a) PR (b) ER spectra of strained (SL5) and partially relaxed (SL6, SL7 and SL8) InP/GaAs type-II QW superlattice structures. Inset shows the ER spectra of the corresponding partially relaxed superlattice structures in an enhanced energy range. Symbols correspond to the Aspens's line shape fitting.

and 1.365 eV respectively. Fig. 7.7(a) shows PR spectra for the strained (SL5) and partially relaxed (SL6, SL7 and SL8) superlattice structures. We do not observe the superlattice features from the partially relaxed superlattice structures. However, GaAs feature at ∼1.42 eV and FKOs in the higher energy region as clearly seen in the PR spectra. Hence, to find out the superlattice feature, ER measurements are performed. ER spectra of the strained superlattice structures are similar to PR spectra of the corresponding superlattice sample. On the other hand, ER spectra of

the partially relaxed superalttice structures are quite different in the lower energy range (<1.424 eV), where superlattice feature is clearly observed in Fig. 7.7(b). The energy positions of the superlattice features are determined by using Aspens's line shape fitting as discussed earlier in this chapter and are listed in Table 7.2. The transition energy of superlattice feature for samples SL5 and SL6 is 1.368 eV and 1.345 eV respectively. Thus, superlattice transition energy red shifts from 1.368 eV to 1.345 eV, when barrier layer thickness of GaAs is decreased from 45 Å to 15 Å. However, it is expected that it should blue shift because quantized hole energy should increase with decrease in the barrier layer thickness as noted from the Fig. 7.2. But, the width of the miniband formed in the conduction and valence bands increases because of the increased overlap of the wave functions of electrons and holes with reduced barrier layer thickness, which effectively decreases the superlattice transition energy. Superlattice transition energy decreases further from 1.345 eV to 1.255 eV with increase of InP QW thickness from 3.3 Å to 5.6 Å and superlattice period from 30 to 50 at constant GaAs barrier layer thickness. The red shift of about 90 meV can be considered as the combined effect of reduced quantum confined effect resulting from increased thickness of InP QW and increased width of the miniband of electrons and holes due to increased superlattice period. The superlattice transition energy decreases from 1.255 eV to 1.235 eV with further increase in the InP QW thickness from 5.6 Å to 6.8 Å. The small red shift of about 20 meV is resulting from the decreased quantum confined effect with increase of InP QW thickness and a small contribution of relaxation (5.9 %) for this superlattice structure. All these results suggest that the observed feature is related to the superlattice structure. Thus, ER measurements provide clear information about the superlattice feature even for

the partially relaxed superlattice structures, where no information can be obtained from PR measurements. The basic difference between PR and ER measurements is that the built-in surface electric field is modulated in an indirect manner by the re-distribution of the electron and hole pairs generated by the application of laser light in the PR measurements. On the other hand, in ER measurements, the built-in surface electric field is directly modulated by applying the external electric field. Hence, it seems that the carriers generated in the partially relaxed superlattice structures by laser light in PR measurements are not able to modulate the surface electric field, because these carriers are captured by the defects and/or traps centers created by the relaxation. Direct modulation of the electric field is more effective in modulating the built-in electric field in case of partially relaxed superlattice structures as compared to indirect modulation technique used in PR measurements.

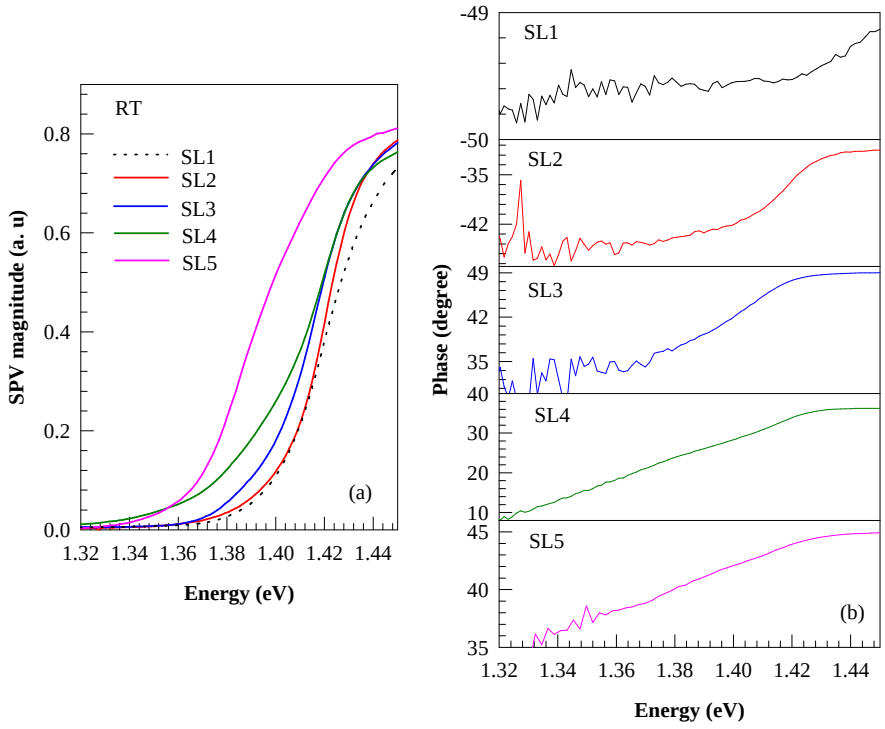

Figure 7.8: Room temperature (a) SPS magnitude (b) its phase for the strained superlattice structures (SL1, SL2, SL3, SL4, and SL5).

7.6 Room temperature surface photo-voltage spectroscopy

SPS is another powerful technique, which is very sensitive for the measurement of very small values of absorption co-efficient for quantum structure like QWs, QDs and even ultrathin QWs. Figure 7.8(a) and Fig. 7.8(b) show room temperature SPS magnitude and its phase at 1 kHz of frequency for all the strained superlattice structures, respectively. The SPS magnitude has been normalized at ∼1.54 eV for the sake of comparison, which is greater than the band gap energy of GaAs (∼1.42 eV). Only GaAs feature at around 1.42eV is observed in the SPS magnitude spectra of samples SL1 and SL2, while there is no feature related to the InP/GaAs superlattice structure in the lower energy range (<1.42 eV). This observation is consistent with the room temperature PR and ER data. However, SPS magnitude starts to increase at about 1.38 eV for sample SL3 indicating that superlattice feature is contributing in the SPS magnitude in addition to the GaAs feature. The energy position of superlattice feature for sample SL3 is in agreement with the room temperature PR data as shown in Fig. 7.6. SPS magnitude starts increasing at lower energy (at around 1.37 eV) for samples SL4 and SL5 that have larger superlattice period as compared to sample SL3, which is also consistent with the room temperature PR and ER data for these superlattice structures. Phase of SPS spectra for sample SL1 shows change around the GaAs feature (1.42 eV) indicating the presence of GaAs feature only and there is no phase change corresponding to superlattice related feature in the lower energy range (<1.42 eV). However, appreciable phase change is occurring from 1.40 eV for sample SL2 indicating that some other process is also occurring alongwith the absorption in GaAs. This may be related to the superlattice

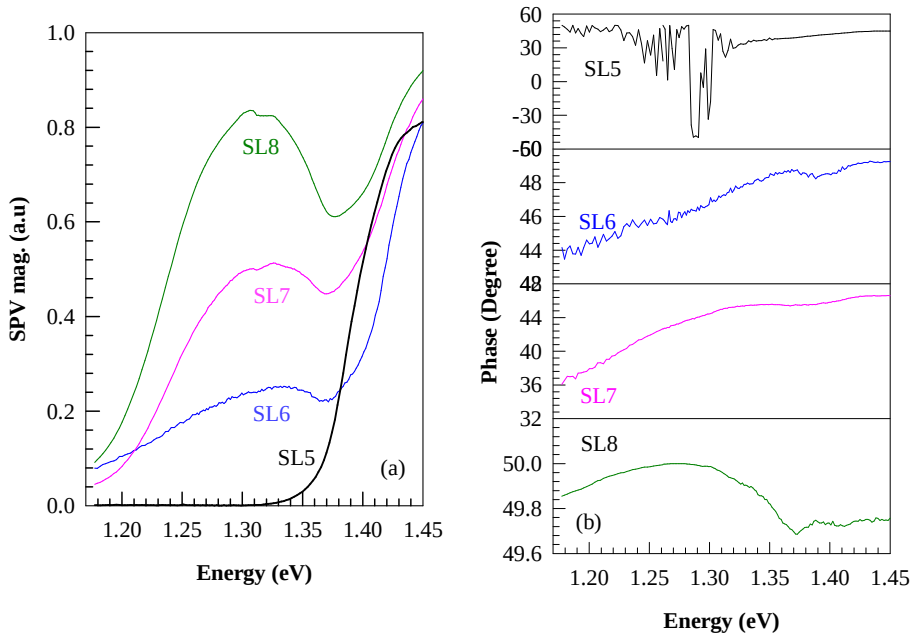

Figure 7.9: Room temperature (a) SPS magnitude (b) its phase for the strained (SL5) and partially relaxed (SL6, SL7 and SL8) superlattice structures.

structure, although we do not observe the signature of superlattice feature in the SPS magnitude spectra. The phase change starts at lower energies; 1.38 eV for SL3 and 1.36 eV for samples SL4 and SL5, which is consistent with the rise in SPS magnitude for samples SL3, SL4 and SL5. Thus, information extracted from the SPS spectra corroborates with that obtained from the room temperature PR and ER data of the strained superlattice structures. Figure 7.9(a) and Fig. 7.9(b) show the SPS magnitude and its phase for strained (SL5) and partially relaxed (SL6, SL7 and SL8) superlattice structures, respectively. SPS magnitude and phase spectra of partially relaxed superlattice structures are quite different in the lower energy range (<1.42 eV) as compared to the strained superlattice structure. Sufficient absorption in the lower energy region (1.18-1.35 eV) for the partially relaxed superlattice structures is seen as compared to the strained superlattice structure. This is consistent with the transition energies of the partially relaxed superlattice structures as determined

from the ER data listed in the Table 7.2.

7.7 Summary

Excitonic transitions are observed even up to room temperature for all the strained superlattice samples. The excitonic transition energy in low temperature PR data red shifts with increasing InP QW thickness, confirming that the observed transition originates from the superlattice structure. Temperature dependent PR data show the presence of some thermally active trap states. The variation of the broadening parameter with temperature in the high temperature region is governed by the scattering of electrons from LO phonons. It has been found that built-in electric field considerably modifies the temperature dependence of the transition energy for the superlattice structure. It is unambiguously determined that the temperature dependence of the superlattice transition energy for a superlattice structure with a low electric field follows the band gap variation of the GaAs barrier material. It has been observed that indirect way of modulation of surface built-in electric field in PR measurements is not helpful in obtaining the information about the superlattice features of the partially relaxed structures. However, direct modulation of electric field in ER measurements is more powerful in providing the signature of the partially relaxed superlattice structures. Appreciable changes in SPS magnitude and phase in the lower energy region of the GaAs band gap for the partially relaxed superlattice structures have been assigned due to the absorption in the energy bands corresponding to the superlattice features.

Chapter 8

Conclusion and Future work

8.1 Summary of the obtained results

This thesis presented MOVPE growth of quantum structures like ultrathin QWs and superlattice structures based on InP/GaAs type-II band alignment material system and detailed studies of their structural, optical and electrical properties. We have grown high quality InP ultrathin QWs of varying well width from ∼0.72-2.14 MLs with GaAs barrier layers by using MOVPE technique. In addition, a MQW sample with 15 numbers of InP QWs is also grown to estimate the QW thickness. Presence of Pendellösung fringes around the GaAs substrate peak in HRXRD pattern for ultrathin QW samples and observation of satellite peaks upto seventh order in the HRXRD profile of the MQW structure confirm high crystalline and interfacial qualities of grown ultrathin QW structures. Determined period thickness of the MQW sample through simulation of HRXRD profile corroborates with that obtained from the cross-sectional TEM measurement on the same sample. Both, HRXRD and cross-sectional TEM, measurements confirm the pseudomorphic nature of the grown ultrathin QWs despite a large lattice mismatch of ∼3.8% between InP and GaAs materials. Further, it is noted from the cross-sectional TEM measurements

that only untrathin QWs are realized without forming the QDs. Intense PL from such InP/GaAs ultrathin QWs are observed at low temperature, which blue shifts with decrease in the QW thickness confirming that observed PL is related to the recombination of carriers in the ultrathin QWs. Observed PL from the QWs is of excitonic nature as determined from power dependent PL measurements. PL peak position (QW transition energy) blue shifts as laser excitation power in PL measurements is increased and the transition energy follows the cube root behavior with laser excitation power. Both these observations confirm that the observed PL originates from the recombination of spatially separated electrons and holes leading to the type-II band alignment of InP and GaAs hetero-junction. Further, a direct evidence of electron confinement in the conduction band of InP is provided by the C-V measurements, where a well defined peak in the carrier depth profile for the ultrathin QW having largest well width is observed at around the geometrical position of the QWs.

Furthermore, temperature dependent C-V measurements are performed to determine the nature of peak observed in the carrier depth profile in room temperature C-V measurements. Peak value of carrier depth profile decreases with rise in temperature. This has been understood in terms of decrease in the separation between Fermi level and confined electronic level in the QW as well as increased probability for thermal emission of electrons into the barrier region. Width of the carrier depth profile increases with increase in temperature, which is related to the Debye averaging process between 2D and 3D carriers at high temperature. At low temperature, width is mainly due to the small value of change in position expectation value of 2D electrons, because of the negligible contribution from 3D electrons at low tem-

perature. Temperature dependent behavior of peak value and width of the carrier depth profile confirms that the observed peak in the carrier depth profile at around the geometrical position of ultrathin QWs is related to the electrons occupying the quantum states formed in the ultrathin QWs. Conduction band offset for InP/GaAs hetero-junction has been obtained by simulating the C-V profile of ultrathin QW through self-consistent solution of Schrodinger and Poisson equations. Determined value of conduction band offset is in agreement with the one obtained by the x-ray photoelectron spectroscopy reported in the literature. Temperature dependent PL from these ultrathin QWs has been extensively studied to determine the behavior of transition energy and luminescence loss mechanism. PL intensity of the ultrathin QWs decreases and that of the GaAs barrier layer increases with increase in temperature. Near room temperature ($\sim$285 K) PL from one of the ultrathin QW is observed. Temperature dependence of GS transition energy has been analyzed by using Bose-Einstein empirical relation and its fitting parameters show that the temperature dependence of transition energy is similar to the band gap variation of GaAs barrier layer material. It is also determined from the Arrhenius-like plot of integrated PL intensity that thermal emission of carriers from ultrathin QWs to GaAs barrier layer are responsible for the PL quenching with temperature.

InP/GaAs type-II QW superlattice structures of varying well width, barrier layer thickness and different number of period are also grown by MOVPE technique. Period thickness for the superlattice structures determined from the HRXRD measurements corroborates with that obtained from the cross-sectional TEM measurements. Crystalline and interfacial quality of superlattice structures is reasonable for thick barrier layers of GaAs as determined from the observation of satellite peaks and inter-

ference fringes between them. Pseudomorphic growth for such superlattice structures has been confirmed from the RSM measurements for (2 2 4) asymmetric reflection. However, interfacial and crystalline quality of the superlattice structures is poor for reduced GaAs barrier layer thickness, which is noted from the increased broadening of the zeroth order satellite peaks as well as disappearance of the interference fringes in the HRXRD rocking curve data. RSM measurements of these superlattice structures for (2 2 4) reflection show partial relaxation, which increases with the QW thickness. Cross-sectional TEM measurements on partially relaxed superlattice structures do not show formation of QDs as well as any dislocations in the structures. On the other hand, it shows undulations in the GaAs barrier layers for partially relaxed superlattice structure having largest InP QW thickness for thinner GaAs barrier layers. Such undulations seem to propagate upto the surface of the superlattice structures and degrade the surface morphology of the partially relaxed superlattice structures. Surfaces of fully strained superlattice structures are atomically flat as determined from the AFM measurements. Surface of the partially relaxed structures, on the other hand, show undulations and the surface roughness increases with the QW thickness for thinner GaAs barrier layers.

Optical properties of fully strained and partially relaxed InP/GaAs superlattice structures have been studied in detail by using PR, ER, and SPS techniques. Superlattice related excitonic feature is observed in low temperature PR measurement, which red shifts with the increase in InP QW thickness confirming that it originates from the superlattice structure. It has been found that the built-in electric field considerably modifies the temperature dependence of GS transition energy of the superlattice structure in PR measurements. For smaller values of electric filed, tem-

perature dependence of superlattice transition energy follows the band gap variation of GaAs barrier layer material. On the other hand, GS transition energy decreases at a faster rate than that of the GaAs material for larger values of built-in electric field. The variation of the broadening parameter with temperature in the high temperature region is governed by the scattering of electrons from LO phonons. It has been found that indirect modulation of built-in electric field in PR measurements is not able to provide the information of superlattice feature for partially relaxed superlattice structures at room temperature. However, direct modulation of built-in electric field in ER measurements is effective in providing the information about the partially relaxed superlattice structures at room temperature. Apart from the strong feature of GaAs barrier layer, a relatively weak feature associated with the superlattice structure is also noted in the room temperature SPS data of the fully strained superlattice samples. This feature gradually becomes stronger as the superalttice period is increased. A broad feature in the ∼1.18-1.35 eV energy range is observed in the SPV data for the partially relaxed superlattice structures, which is consistent with the room temperature ER data.

In conclusion, a detailed characterization of InP/GaAs ultrathin QWs and short period superlattice structures have been performed by several complementary techniques. A few novel physical phenomenon have been observed for this interesting material system based on type-II band alignment architecture.

8.2 Suggested future work

MOVPE growth of InP/GaAs based type-II ultrathin QWs and superlattice structures have been optimized. Structural, optical and electrical properties of these

quantum structures have shown their high crystalline and optical qualities. Type-II systems have already found potential applications in several optoelectronic devices like photodetectors and solar cells. For the future work, it is proposed to grow device structures like photodetector and solar cell based on quantum structures of InP/GaAs type-II system and to study device performance.

APPENDIX

APPENDIX A

Simulation of C-V profiles for a QW structure has been performed by solving Schrodinger and Poisson equations in a self-consistent manner under envelop function approximation using finite difference approach [140, 191]. We have followed the procedure as described in the literature [140,151,154] which is described in brief here. One dimensional Schrodinger equation can be written as

$$-\frac{\hbar^2}{2}\frac{\partial}{\partial z}\left(\frac{1}{m^*(z)}\frac{\partial}{\partial z}\right)\psi(z)+V(z)\psi(z)=E\psi(z), \tag{A.1}$$

where, z is the coordinate along the growth direction. ψ and E are the wave-function and the energy of electron respectively. $m^*(z)$ is the position dependent effective mass of the electron. $V(z)$ is the potential energy given by the following relation

$$V(z)=-e\phi(z)+\Delta E_C, \tag{A.2}$$

where, e is the electronic charge, ΔE_C is the conduction band discontinuity and $\phi(z)$ is the electrostatic potential which satisfy the Poisson equation given by

$$\frac{\partial}{\partial z}\left(\epsilon_0\epsilon(z)\frac{\partial}{\partial z}\right)\phi(z)=-e\left[N_d^+(z)-n(z)\right], \tag{A.3}$$

where, ϵ_0 is the permittivity of free space, $\epsilon(z)$ is the dielectric constant and N_d^+ is the ionized donor density. $n(z)$ is the the free electron density in conduction band. Hence, $n(z)$ is nothing but FCD, which is a sum of 2D electron density (n_{2D}(z)) in the QW and 3D electron density ($n_{3D}(z)$) in the barrier region, which can be written as

$$n\left(z\right) = n_{2D}\left(z\right) + n_{3D}\left(z\right), \tag{A.4}$$

where, 2D electron density in the QW is given through the following relation

$$n_{2D}\left(z\right) = \frac{m^*\left(z\right)k_BT}{\pi\hbar^2}\sum_i ln\left[1 + exp\left\{\frac{E_F - E_i}{k_BT}\right\}\right]\left|\psi_i\left(z\right)\right|^2, \tag{A.5}$$

where, E_F is the Fermi level position, E_i is the energy of confined electronic level and $\left|\psi\left(z\right)\right|^2$ is the normalized wave function of confined electrons. 3D electron density in the barrier region using Maxwell-Boltzmann statistics can be written as

$$n_{3D}\left(z\right) = N_C exp\left[-\frac{E_C - E_F}{k_BT}\right], \tag{A.6}$$

where, E_C is the position of the conduction band of the barrier material.

C-V curve is calculated in the following manner. Bound state eigen energies and eigen functions are calculated from the Schrodinger equation A.1 by taking a rectangular potential profile of the QW structure for the first iteration. Then, $n_{2D}(z)$ for the QW is extracted from the equation A.5. After this, Poisson equation A.3 is solved to get the potential profile ($\phi(z)$), which is again used to get new potential energy through equation A.2 for the solution of Schrodinger equation for next iteration. This iteration process is repeated for in a self-consistent manner until the difference between the values of potential energy in $(k-1)^{th}$ and k^{th} iteration is less than $1{\times}10^{-8}$ eV. The boundary conditions for the potential are as follows: Sum

of the barrier height and the applied voltage is the value of potential at z = 0 (at the surface), and $\phi(z) = 0$ at a point deep inside the structures, where the charge neutrality holds. Thereafter, the total charge stored in the structure is calculated by using the Gauss theorem i.e. $Q = \epsilon_0 \epsilon A E$, where E is the electric field at the surface and is given by $\frac{\partial \phi}{\partial z}$. The capacitance is then given by the first derivative of the stored charge i.e. $\frac{\Delta Q}{\Delta V}$, where ΔQ denotes the total charge variation caused by the reverse bias change (ΔV) around the fixed reverse bias voltage (V). In this manner, capacitance as a function of applied reverse bias voltage is calculated and afterwards the ACD is profile obtained by using the following relations

$$N_{C-V} = -\frac{2}{e\epsilon_0 \epsilon A^2 \left(\frac{dC^{-2}}{dV}\right)}, \tag{A.7}$$

and

$$W = \frac{\epsilon_0 \epsilon A}{C}. \tag{A.8}$$

References

[1] N. Chand, E. E. Becker, J. P. van der Ziel, S. N. G. Chu, and N. K. Dutta, *Appl. Phys. Lett.*, 1991, **58**, 1704.

[2] R. Dingle, H. L. Stormer, A. C. Gossard, and W. Wiegmann, *Appl. Phys. Lett.*, 1978, **33**, 665.

[3] T. Mimura, S. Hiyamizu, T. Fujii, and K. Nanbu, *Jpn. J. Appl. Phys.*, 1980, **19**, L225.

[4] S. Raghavan, D. Forman, P. Hill, N. R. Weisse-Bernstein, G. von Winckel, P. Rotella, S. Krishna, S. W. Kennerly, and J. W. Little, *J. Appl. Phys.*, 2004, **96**, 1036.

[5] P. Chen, Q. Gong, C. F. Cao, S. G. Li, Y. Wang, Q. B. Liu, L. Yue, Y. G. Zhang, S. L. Feng, C. H. Ma, and H. L. Wang, *Appl. Phys. Lett.*, 2011, **98**, 121102.

[6] E. Ribeiro, A. O. Govorov, W. C. Jr., and G. Medeiros-Ribeiro, *Phys. Rev. Lett.*, 2001, **92**, 126402.

[7] D. Alonso-Alvarez, B. Alen, J. M. Garcia, and J. M. Ripalda, *Appl. Phys. Lett.*, 2007, **91**, 263103.

[8] S. D. Singh, S. Porwal, T. K. Sharma, and K. C. Rustagi, *J. Appl. Phys.*, 2006, **99**, 063517.

[9] M. Gerling, M. E. Pistol, and W. Seifert, *Physica E*, 1998, **2**, 794.

[10] T. Baier, U. Mantz, K. Thonke, R. Sauer, F. Schaffier, and H. J. Herzog, *Phys. Rev. B*, 1994, **50**, 15191.

[11] B. Bansal, S. Godefroo, M. Hayne, G. Medeiros-Ribeiro, and V. V. Moshchalkov, *Phys. Rev. B*, 2009, **80**, 205317.

[12] C. R. Moon, B. D. Choe, S. D. Kwon, and H. Lim, *Appl. Phys. Lett.*, 1998, **72**, 1196.

[13] J. S. Wang, J. F. Chen, J. L. Huang, P. Y. Wang, and X. J. Guo, *Appl. Phys. Lett.*, 2000, **77**, 3027.

[14] G. Scamarcio, O. Brandt, L. Tapfer, D. J. Mowbray, M. Cardona, and K. Ploog, *J. Appl. Phys.*, 1991, **69**, 786.

[15] R. Passler, *Phys. Rev. B*, 2002, **66**, 085201.

[16] M. Fox, *Optical Properties of Solids*, Oxford University Press, 2001.

[17] J. Singh, *Electronic and optoelectronic properties of semiconductor structures*, Cambridge University Press, 2003.

[18] S. Gerhard, V. Baumann, S. Hofling, and A. Forchel, *Nanotechnology*, 2009, **20**, 434016.

[19] S. Gerhard, S. Kremling, S. Hofling, L. Worschech, and A. Forchel, *Nanotechnology*, 2011, **22**, 415604.

[20] F. Hatami, W. T. Masselink, L. Schrottke, J. W. Tomm, V. Talalaev, C. Kristukat, and A. R. Goni, *Phys. Rev. B*, 2003, **67**, 085306.

[21] T. S. Shamirzaev, D. S. Abramkin, A. K. Gutakovskii, and M. A. Putyato, *Appl. Phys. Lett.*, 2010, **97**, 023108.

[22] T. N. Thanh, C. Robert, C. Cornet, M. Perrin, J. M. Jancu, N. Bertru, J. Even, N. Chevalier, H. Folliot, O. Durand, and A. L. Corre, *Appl. Phys. Lett.*, 2011, **99**, 143123.

[23] J. H. Ryou, R. D. Dupuis, D. T. Mathes, R. Hull, C. V. Reddy, and V. Narayanamurti, *Appl. Phys. Lett.*, 2001, **78**, 3526.

[24] M. Strauss, S. Hofling, and A. Forchel, *Nanotechnology*, 2009, **20**, 505601.

[25] V. M. Ustinov, A. E. Zhukov, A. R. Kovsh, N. A. Maleev, A. F. T. S. S. Mikhrin, M. V. Maximov, B. V. Volovik, D. A. Bedarev, P. S. Kop'ev, Z. I. Alferov, L. E. Vorob'ev, D. A. Firsov, A. A. Suvorov, I. P. Soshnikov, P. Werner, N. N. Ledentsov, and D. Bimberg, *Microelectronics Journal*, 2000, **31**, 1.

[26] D. L. Huffaker, G. Park, Z. Zou, O. B. Shchekin, and D. Deppe, *Appl. Phys. Lett.*, 1998, **73**, 2564.

[27] N. N. Ledentsov, A. R. Kovsh, A. E. Zhukov, N. A. Maleev, S. S. Mikhrin, A. P. Vasil'ev, E. S. Semenova, M. V. Maximov, Y. M. Shernyakov, N. V. Kryzhanovskaya, V. M. Ustinov, and D. Bimberg, *Electron. Lett.*, 2003, **39**, 1126.

[28] M. V. Maximov, A. F. TsatsulŠnikov, B. V. Volovik, D. A. Bedarev, A. Y. Egorov, A. E. Zhukov, A. R. Kovsh, N. A. Bert, V. M. Ustinov, P. S. KopŠev,

Z. I. Alferov, N. N. Ledentsov, D. Bimberg, I. P. Soshnikov, and P. Werner, *Appl. Phys. Lett.*, 1999, **75**, 2347.

[29] W. M. Schulz, R. Robbach, M. Reischle, G. J. Beirne, M. Bommer, M. Jetter, and P. Michler, *Phys. Rev. B*, 2009, **79**, 035329.

[30] S. Barik, H. H. Tan, and C. Jagadish, *Nanotechnology*, 2006, **17**, 1867.

[31] C. Paranthoen, C. Platz, G. Moreau, N. Bertru, O. Dehaese, A. L. Corre, P. Miska, J. Even, H. Folliot, C. Labbe, G. Patriarche, J. C. Simon, and S. Loualiche, *J. Crystal Growth*, 2003, **251**, 230.

[32] Y. Qiu and D. Uhl, *Appl. Phys. Lett.*, 2004, **84**, 1510.

[33] D. Bimberg, M. Grundmann, and N. N. Ledentsov, *Quantum Dot Heterostructures*, John Wiley and Sons, New York, 1999.

[34] P. Y. Yu and M. Cardona, *Fundamentals of Semiconductors*, Springer, 2001.

[35] P. K. Basu, *Theory of optical processes in semiconductors: Bulk and Microstructures*, Clarendon press, Oxford, 1997.

[36] G. Bastard, *Wave mechanics applied to semiconductor heterostructures*, Les Editions de Physique, France, 1988.

[37] A. Y. Cho and J. R. Arthur, *Prog. Solid Stat. Chem.*, 1975, **10**, 157.

[38] M. B. Panish, *Science*, 1980, **208**, 916.

[39] B. A. Joyce, *Rep. Prog. Phys.*, 1985, **48**, 1637.

[40] H. M. Manasevit, *J. Crystal Growth*, 1972, **13/14**, 306.

[41] T. F. Kuech, *Mater. Sci. Reports*, 1987, **2**, 1.

[42] R. D. Dupuis, *Science*, 1984, **226**, 623.

[43] G. B. Stringfellow, *Organometallic Vapor-Phase Epitaxy, Theory and Practice*, Academic Press, Inc., 1989.

[44] O. Brandt, L. Tapfer, R. Cingolani, K. Ploog, M. Hohenstein, and F. Phillipp, *Phys. Rev. B*, 1990, **41**, 12599.

[45] A. R. Goni, M. Stroh, C. Thomsen, F. Heinrichsdorff, V. Türck, and D. Bimberg, *Appl. Phys. Lett.*, 1998, **72**, 1433.

[46] J. A. Gupta, S. P. Watkins, E. D. Crozier, J. C. Woicik, D. A. Harrison, D. T. Jiang, I. J. Pickering, and B. A. Karlin, *Phys. Rev. B*, 2000, **61**, 2073.

[47] B. Liu, Q. Li, Z. Xu, and W. K. Ge, *J. Phys.: Condens. Matter*, 2001, **13**, 3923.

[48] Z. Sun, Z. Y. Xu, Y. Ji, B. Q. Sun, B. R. Wang, S. S. Huang, and H. Q. Ni, *Appl. Phys. Lett.*, 2007, **90**, 071907.

[49] C. Yang, X. Cui, S. Q. Shen, Z. Xu, and W. Ge, *Phys. Rev. B*, 2009, **80**, 035313.

[50] T. Li, X. H. Zhang, Y. G. Zhu, X. Huang, L. F. Han, X. J. Shang, H. Q. Ni, and Z. C. Niu, *Physica E*, 2010, **42**, 1597.

[51] N. Tansu, J. Y. Yeh, and L. J. Mawst, *IEEE. J. Select. Topics Quantum Electron.*, 2003, **9**, 1220.

[52] M. Geller, C. Kapteyn, L. Muller-Kirsch, R. Heitz, and D. Bimberg, *Appl. Phys. Lett.*, 2003, **82**, 2706.

[53] R. B. Laghumavarapu, A. Moscho, A. Khoshakhlagh, M. El-Emawy, L. F. Lester, and D. L. Huffaker, *Appl. Phys. Lett.*, 2007, **90**, 173125.

[54] J. H. Bahng, S. J. Moon, K. H. Lee, J. C. Choi, K. Jeong, and H. L. Park, *Appl. Phys. Lett.*, 2004, **84**, 3870.

[55] B. R. Bennett and B. V. Shanabrook in *Thin Films: Heteroepitaxial systems*, ed. W. K. Liu and M. B. Santos; World Scientific, Singapore, 1999; p. 413.

[56] Y. S. Chiu, M. H. Ya, W. S. Su, and Y. F. Chen, *J. Appl. Phys.*, 2002, **92**, 5810.

[57] C. Y. Jin, H. Y. Liu, S. Y. Zhang, Q. Jiang, S. L. Liew, M. Hopkinson, T. J. Badcock, E. Nabavi, and D. J. Mowbray, *Appl. Phys. Lett.*, 2007, **91**, 021102.

[58] C. M. Lin and Y. F. Chen, *Appl. Phys. Lett.*, 2004, **85**, 2544.

[59] Y. Aharanov and D. Bohm, *Phys. Rev.*, 1959, **115**, 485.

[60] A. Tonomura, N. Osakabe, T. Matsuda, T. Kawasaki, J. Endo, S. Yano, and H. Yamada, *Phys. Rev. Lett.*, 1986, **56**, 792.

[61] W. X. Gao, K. Ismail, K. Y. Lee, J. O. Chu, and S. Washburn, *Appl. Phys. Lett.*, 1994, **65**, 3114.

[62] A. Fuher, S. Luscher, T. Ihn, K. Ensslin, W. Wegscheider, and M. Bichler, *Nature (London)*, 2001, **413**, 822.

[63] K. L. Janssens, B. Partoens, and F. M. Peeters, *Phys. Rev. B*, 2001, **64**, 155324.

[64] M. Bayer, M. Korkusinski, P. Hawrylak, T. Gutbrod, M. Michel, and A. Forchel, *Phys. Rev. Lett.*, 2003, **90**, 186801.

[65] K. Tsumura, S. Nomura, P. Mohan, J. Motohisa, and T. Fukui, *Jpn. J. Appl. Phys.*, 2007, **46**, L440.

[66] I. L. Kuskovsky, W. MacDonald, A. O. Govorov, L. Mourokh, X. Wei, M. C. Tamargo, M. Tadic, and F. M. Peeters, *Phys. Rev. B*, 2007, **76**, 035342.

[67] S. Miyamoto, O. Moutanabbir, T. Ishikawa, M. Eto, E. E. Haller, K. Sawano, Y. Shiraki, and K. M. Itoh, *Phys. Rev. B*, 2010, **82**, 073306.

[68] J. R. Meyer, C. A. Hoffman, F. J. Bartoli, and L. R. Ram-Mohan, *Appl. Phys. Lett.*, 1995, **67**, 757.

[69] W. W. Bewley, C. L. Canedy, C. S. Kim, I. Vurgaftman, M. Kim, and J. R. Meyer, *Physica E*, 2004, **20**, 466.

[70] P. Dowd, W. Braun, D. J. Smith, C. M. Ryu, C. Z. Guo, S. L. Chen, U. Koelle, S. R. Johnson, and Y. H. Zhang, *Appl. Phys. Lett.*, 1999, **75**, 1267.

[71] N. Tansu and L. J. Mawst, *IEEE J. Quantum Electron.*, 2003, **39**, 1205.

[72] I. Vurgaftman, J. R. Meyer, N. Tansu, and L. J. Mawst, *Appl. Phys. Lett.*, 2003, **83**, 2742.

[73] J. Y. Yeh, L. J. Mawst, A. A. Khandekar, T. F. Kuech, I. Vurgaftman, J. R. Meyer, and N. Tansu, *Appl. Phys. Lett.*, 2006, **88**, 051115.

[74] L. J. Mawst, J. Y. Huang, D. P. Xu, J. Yeh, G. Tsvid, T. F. Kuech, and N. Tansu, *IEEE J. Sel. Topics Quantum Electron.*, 2008, **14**, 979.

[75] I. Vurgaftman, J. R. Meyer, N. Tansu, and L. J. Mawst, *J. Appl. Phys.*, 2004, **96**, 4653.

[76] R. A. Arif, H. Zhao, and N. Tansu, *Appl. Phys. Lett.*, 2008, **92**, 011104.

[77] H. Zhao, R. A. Arif, and N. Tansu, *J. Appl. Phys.*, 2008, **104**, 043104.

[78] S. H. Park, D. Ahn, B. H. Koo, and J. E. Oh, *Appl. Phys. Lett.*, 2010, **96**, 051106.

[79] P. B. Allen and M. Cardona, *Phys. Rev. B*, 1981, **23**, 1495.

[80] H. Y. Fan, *Phys. Rev.*, 1951, **82**, 900.

[81] B. Bansal ,*Construction of a 17 tesla pulsed magnet and effects of arsenic alloying and heteroepitaxy on transport and optical properties of indium antimonide,* PhD thesis, Indian Institute of Science, 2004.

[82] Y. P. Varshni, *Physica*, 1967, **34**, 149.

[83] P. Lautenschlager, M. Garriga, and M. Cardona, *Phys. Rev. B*, 1987, **36**, 4813.

[84] D. S. Chemla, D. A. B. Miller, P. W. Smith, A. C. Gossard, and W. Wiegmann, *IEEE J. Quantum Electron.*, 1984, **20**, 265.

[85] W. S. Chi, D. Y. Lin, Y. S. Huang, H. Qiang, F. H. Pollak, D. L. Mathine, and G. N. Maracas, *Semicond. Sci. Technol.*, 1996, **11**, 345.

[86] S. Guha, Q. Cai, M. Chandrasekhar, H. R. Chandrasekhar, H. Kim, A. D. Alvarenga, R. Vogelgesang, A. K. Ramdas, and M. R. Melloch, *Phys. Rev. B*, 1998, **58**, 7222.

[87] L. Malikova, F. H. Pollak, R. A. Masut, P. Desjardins, and L. G. Mourokh, *J. Appl. Phys.*, 2003, **94**, 4995.

[88] B. Bansal, V. K. Dixit, V. Venkatraman, and H. L. Bhat, *Appl. Phys. Lett.*, 2003, **82**, 4720.

[89] S. J. Xu, L. X. Zheng, S. H. Cheung, M. H. Xie, S. Y. Tong, and H. Yang, *Appl. Phy. Lett.*, 2002, **81**, 4389.

[90] H. Zhao, S. Wachter, and H. Kalt, *Phys. Rev. B*, 2002, **66**, 085337.

[91] D. Gammon, S. Rudin, T. L. Reineeke, D. S. Katzer, and S. S. Kyono, *Phys. Rev. B*, 1995, **51**, 16785.

[92] P. Misra, T. K. Sharma, and L. M. Kukreja, *Superlattice and Microstructure*, 2007, **42**, 212.

[93] D. Gershoni, H. Temkin, J. M. Vandenberg, S. N. G. Chu, R. A. Hamm, and M. B. Panish, *Phys. Rev. Lett.*, 1988, **60**, 448.

[94] D. Gershoni, H. Temkin, M. B. Panish, and R. A. Hamm, *Phys. Rev. B*, 1989, **39**, 5531.

[95] M. E. P. A. Gustafsson, M. Gerling, L. Samuelson, and H. Titze, *J. Crystal Growth*, 1991, **107**, 458.

[96] M. Gerling, M. E. Pistol, L. Samuelson, W. Seifert, J. O. Fornell, and L. Ledebo, *Appl. Phys. Lett.*, 1991, **59**, 806.

[97] M. Gerling, M. E. Pistol, and W. Seifert, *Physica E*, 1998, **2**, 794.

[98] D. Hessman, M. E. Pistol, J. Olajos, and L. Samuelson, *Phys. Rev. B*, 1994, **49**, 17118.

[99] M. E. Pistol, M. Gerling, D. Hessman, and L. Samuelson, *Phys. Rev. B*, 1992, **45**, 3628.

[100] B. Wang and S. J. Chua, *Appl. Phys. Lett.*, 2001, **78**, 628.

[101] M. K. K. Nakaema, F. Iikawa, M. J. S. P. Brasil, E. Ribeiro, G. Medeiros-Ribeiro, W. C. Jr., M. Z. Maialle, and M. H. Degani, *Appl. Phys. Lett.*, 2002, **81**, 2743.

[102] M. P. F. de Godoy, P. F. Gomes, M. K. K. Nakaema, F. Iikawa, M. J. S. P. Brasil, R. A. Caetano, J. R. Madureira, J. R. R. Bortoleto, M. A. Cotta, E. Ribeiro, G. E. Marques, and A. C. R. Bittencourt, *Phys. Rev. B*, 2006, **73**, 033309.

[103] M. P. F. Godoy, M. K. K. Nakaema, F. Iikawa, M. J. S. P. Brasil, J. M. Lopes, J. R. R. Bortoleto, M. A. Cotta, R. Magalhaes-Paniago, M. J. Morschbacher, and P. F. P. Fichtner, *J. Appl. Phys.*, 2007, **101**, 073508.

[104] J. R. Madureira, M. P. F. de Godoy, M. J. S. P. Brasil, and F. Iikawa, *Appl. Phys. Lett.*, 2007, **90**, 212105.

[105] A. B. Veloso, M. K. K. Nakaema, M. P. F. de Godoy, J. M. J. Lopes, F. Iikawa, M. J. S. P. Brasil, J. R. R. Bortoleto, M. A. Cotta, P. F. P. Fichtner, M. Morschbacher, and J. R. Madureira, *Appl. Phys. Lett.*, 2007, **91**, 121917.

[106] P. F. Gomes, M. P. F. Godoy, A. B. Veloso, M. K. K. Nakaema, F. Iikawa, M. J. S. P. Brasil, J. R. R. Bortoleto, M. A. Cotta, and J. R. Madureira, *Phys. Stat. Sol. (c)*, 2007, **4**, 385.

[107] L. N. Coelho, R. Magalhaes-Paniago, A. Malachias, J. G. Zelcovit, and M. A. Cotta, *Appl. Phys. Lett.*, 2008, **92**, 021903.

[108] P. F. Gomes, M. P. F. de Godoy, G. O. Dias, F. Iikawa, M. J. S. P. Brasil, M. A. Cotta, and J. R. Madureira, *J. Phys. D : Appl. Phys.*, 2010, **43**, 045303.

[109] F. Iikawa, V. Donchev, T. Ivanov, G. O. Dias, L. H. G. Tizei, R. Lang, E. Heredia, P. F. Gomes, M. J. S. P. Brasil, M. A. Cotta, D. Ugarte, J. P. M. Pastor, M. M. de Lima Jr, and A. Cantarero, *Nanotechnology*, 2011, **22**, 065703.

[110] N. Nelson, *RCA Review*, 1963, **24**, 603.

[111] V. K. Dixit, B. Bansal, V. Venkataraman, G. N. Subbanna, K. S. Chandrasekharan, B. M. Arora, and H. L. Bhat, *Appl. Phys. Lett.*, 2002, **80**, 2102.

[112] F. J. Grunthaner, M. Y. Yen, R. Fernandez, T. C. Lee, A. Madhukar, and B. F. Lewis, *Appl. Phys. Lett.*, 1985, **46**, 983.

[113] J. M. Gerard and J. Y. Marzin, *Appl. Phys. Lett.*, 1988, **53**, 568.

[114] G. Huang, J. Yang, P. Bhattacharya, G. Ariyawansa, and A. G. U. Perera, *Appl. Phys. Lett.*, 2008, **92**, 011117.

[115] A. Knauer, F. Brunner, T. Kolbe, V. Kuller, H. Rodriguez, S. Einfeldt, M. Weyers, and M. Kneissl, *Proc. of SPIE*, 2009, **7321**, 72310G.

[116] T. K. Sharma, M. Zorn, F. Bugge, R. Hulsewede, G. Erbert, and M. Weyers, *IEEE Photonics Techno. Lett.*, 2002, **14**, 887.

[117] B. M. Arora, A. Majumdar, A. P. Shah, M. R. Gokhale, S. Ghosh, A. Bhattacharya, and D. Sengupta, *Infrared Physics and Technology*, 2007, **50**, 206.

[118] R. Schwabe, F. Pietag, M. Faulkner, S. Lassen, V. Gottschalch, R. Franzheld, A. Bitz, and J. L. Staehli, *J. Appl. Phys.*, 1995, **77**, 6295.

[119] F. P. Schneider and B. W. Wessels, *J. Appl. Phys.*, 1991, **70**, 405.

[120] K. Taira, H. Kawai, I. Hase, K. Kaneko, and N. Watanabe, *Appl. Phys. Lett.*, 1988, **53**, 495.

[121] C. A. Tran, R. A. Ares, V. A. Karasyuk, S. P. Watkins, G. Letourneau, and R. Leonelli, *Phys. Rev. B*, 1997, **55**, 4633.

[122] O. J. Pitts *Growth and characterization of ultrathin InAs/GaAs and GaAs/GaSb quantum wells,* PhD thesis, Simon Fraser University, 2004.

[123] C. Agert, F. Dimroth, U. Schubert, A. W. Bett, S. Leu, and W. Stolz, *Solar Energy Materials and Solar Cells*, 2001, **66**, 637.

[124] M. Longoa, R. Magnanini, A. Parisini, L. Tarricone, A. Carbognani, C. Bocchi, and E. Gombia, *J. Crystal Growth*, 2003, **248**, 119.

[125] P. Velling, M. Agethen, W. Prost, and F. J. Tegude, *J. Crystal Growth*, 2000, **221**, 722.

[126] E. J. Skogen, Jonathon, S. Barton, J. W. Raring, L. A. Coldren, and S. P. Denbaars, *J. Crystal Growth*, 2004, **272**, 564.

[127] P. F. Fewster, *X-Ray scattering from Semiconductors*, Imperial College Press, London, 2000.

[128] V. L. Mirnov, *Fundamentals of scanning probe microscopy*, Russian academy of sciences, Institute of Physics of Microstructures, 2004.

[129] G. D. Gilland, *Mater. Sci. Eng. R.*, 1997, **18**, 99.

[130] O. J. Glembocki and B. V. Shanabrook, *Semiconductors and Semimetals*, Vol. 36, Academic, San Diego, CA, 1992.

[131] S. Datta, S. Ghosh, and B. M. Arora, *Rev. Sci. Instrum.*, 2001, **72**, 177.

[132] T. K. Sharma, S. Porwal, R. Kumar, and S. Kumar, *Rev. Sci. Inst.*, 2002, **73**, 1835.

[133] T. K. Sharma *Metal organic vapour phase epitaxial growth of III-V semiconductors,* PhD thesis, Devi Ahilya Vishvavidyalaya, Indore, 2002.

[134] P. Blood and J. W. Orton, *The electrical characterization of semiconductors: majority carriers and electron states*, Academic Press, London, 1992.

[135] C. Kapteyn *Carrier emission and electronic properties of self-organized semiconductor quantum dots,* PhD thesis, Technical University, Berlin, 2001.

[136] S. K. Khamari, Characterization of MOVPE grown GaAs based p-i-n diodes, Master's thesis, Homi Bhabha National Institute, Mumbai, 2009.

[137] D. K. Sengupta, S. L. Jackson, D. Ahmari, H. C. Kuo, J. I. Malin, S. Thomas, M. Feng, G. E. Stillman, Y. C. Chang, L. Li, and H. C. Liu, *Appl. Phys. Lett.*, 1996, **69**, 3209.

[138] C. M. Lin and Y. F. Chen, *Appl. Phys. Lett.*, 2004, **85**, 2544.

[139] Z. Horvath, L. Dozsa, V. V. Tuyen, B. Podoor, A. Nemcsics, P. Frigeri, E. Gombia, R. Mosca, and S. Franchi, *Thin Solid Films*, 2000, **367**, 89.

[140] V. I. Zubkov, M. A. Melnik, A. V. Solomonov, E. O. Tsvelev, F. Bugge, M. Weyers, and G. Tränkle, *Phys. Rev. B*, 2004, **70**, 075312.

[141] R. Cingolani, O. Brandt, L. Tapfer, G. Scamarcio, G. C. L. Rocca, and K. H. Ploog, *Phys. Rev. B*, 1990, **42**, 3209.

[142] J. Brübach, A. Y. Silov, J. E. M. Haverkort, W. V. D. Vleuten, and J. H. Wolter, *Phys. Rev. B*, 1999, **59**, 10315.

[143] R. Leonelli, C. A. Tran, J. L. Brebner, J. T. Graham, R. Tabti, R. A. Masut, and S. Charbonneau, *Phys. Rev. B*, 1993, **48**, 11135.

[144] C. A. Tran, R. A. Ares, V. A. Karasyuk, S. P. Wattkins, G. Letourneau, and R. Leonelli, *Phys. Rev. B*, 1997, **55**, 4633.

[145] D. Z. Y. Ting, S. V. Bandara, S. D. Gunapala, J. M. Mumolo, S. A. Keo, C. J. Hill, J. K. Liu, E. R. Blazejewski, S. B. Rafol, and Y. C. Chang, *Appl. Phys. Lett.*, 2009, **94**, 111107.

[146] A. A. Martinez and I. Calderon, *Microelectronics*, 2008, **39**, 594.

[147] J. E. Fouquet and A. E. Siegman, *Appl. Phys. Lett.*, 1985, **46**, 280.

[148] J. Tignon, O. Heller, P. Roussignol, J. Martinez-Pastor, P. Lelong, and G. Bastard, *Phys. Rev. B*, 1998, **58**, 7076.

[149] H. Kroemer, W.-Y. Chien, J. S. Harris, and D. D. Edwall, *Appl. Phys. Lett.*, 1980, **36**, 295.

[150] A. J. Chiquito and M. G. D. Souza, *Physica E (Amsterdem)*, 2005, **25**, 613.

[151] S. Subramanian, B. M. Arora, A. K. Srivastava, G. Fernandes, and S. Banerjee, *J. Appl. Phys.*, 1993, **74**, 7618.

[152] A. N. Petrovskaya and V. I. Zubkov, *Semiconductors*, 2009, **43**, 1328.

[153] K. Tittelbach-Helmrich, *Semicond. Sci. Technol.*, 1993, **8**, 1372.

[154] C. R. Moon, B. D. Choe, S. D. Kwon, H. K. Shin, and H. Lim, *J. Appl. Phys.*, 1998, **84**, 2673.

[155] P. K. Kush, R. C. Sharma, R. S. Doohan, A. K. Sagar, C. L. Choudhary, and M. S. Ansari, *in Proceedings of National Seminar and Conference on Cryogenics*, 2005.

[156] J. R. Waldrop, R. W. Grant, and E. A. Kraut, *Appl. Phys. Lett.*, 1989, **54**, 1878.

[157] S. L. Chuang, *Physics of Optoelectronic Devices*, John Wiely and Sons. Inc., 1995.

[158] M. D. Ventra and K. A. Mader, *Phys. Rev. B*, 1997, **55**, 13148.

[159] K. Shiraishi and E. Yamaguchi, *Phys. Rev. B*, 1990, **42**, 3064.

[160] A. Kangarlu, H. R. Chandrasekhar, M. Chandrasekhar, Y. M. Kapoor, F. A. Chambers, B. A. Vojak, and J. M. Meese, *Phys. Rev. B*, 1988, **37**, 1035.

[161] W. S. Chi, Y. S. Huang, H. Qiang, F. H. Pollak, D. G. Pettit, and J. M. Woodall, *Jpn. J. Appl. Phys. Part 1*, 1994, **33**, 966.

[162] Z. Y. Xu, Z. D. Lu, X. P. Yang, Z. L. Yuan, B. Z. Zheng, J. Z. Xu, W. K. Ge, Y. Wang, J. Wang, and L. L. Chang, *Phys. Rev. B*, 1996, **54**, 11528.

[163] M. K. Hudait, P. Modak, S. Hardikar, and S. B. Krupanidhi, *J. Appl. Phys.*, 1998, **83**, 4454.

[164] R. Pickenhain, H. Schmidt, and V. Gottschach, *J. Appl. Phys.*, 2000, **88**, 948.

[165] A. Lanacer, J. F. Chabot, M. Cote, R. Leonelli, D. Frankland, and R. A. Masut, *Phys. Rev. B*, 2005, **72**, 075349.

[166] A. A. Toropov, O. G. Lyublinskaya, B. Y. Meltser, V. A. SolovŠev, A. A. Sitnikova, M. O. Nestoklon, O. V. Rykhova, S. V. Ivanov, K. Thonke, and R. Sauer, *Phys. Rev. B*, 2004, **70**, 205314.

[167] W. H. Chang, Y. A. Liao, W. T. Hsu, M. C. Lee, P. C. Chiu, and J. I. Chyi, *Appl. Phys. Lett.*, 2008, **93**, 033107.

[168] R. J. Potter and N. Balkan, *J. Phys.: Condens. Matter*, 2004, **16**, S3387.

[169] S. D. Singh, V. K. Dixit, S. Porwal, R. Kumar, A. K. Srivastava, T. Ganguli, T. K. Sharma, and S. M. Oak, *Appl. Phys. Lett.*, 2010, **97**, 111912.

[170] S. D. Singh, S. Porwal, A. Khaka, V. K. Dixit, A. K. Srivastava, and S. M. Oak, *J. Phys. D: Appl. Phys.*, 2010, **43**, 455410.

[171] S. D. Singh, V. K. Dixit, S. K. Khamari, R. Kumar, A. K. Srivastava, T. Ganguli, and S. M. Oak, *J. Appl. Phys.*, 2011, **109**, 073702.

[172] C. A. Tran, R. A. Masut, J. L. Brebner, and M. Jouanne, *J. Appl. Phys.*, 1994, **75**, 2398.

[173] Y. Wei, A. Gin, M. Razeghi, and G. J. Brown, *Appl. Phys. Lett.*, 2002, **81**, 3675.

[174] H. Asahi, K. Asami, T. Watanabe, S. J. Yu, T. Kaneko, S. Emura, and S. Gonda, *Appl. Phys. Lett.*, 1991, **58**, 1407.

[175] O. Yastrubchak, J. Bak-Misiuk, E. Lusakowska, J. Kaniewski, J. Z. Domagala, T. Wosinski, A. Shalimov, K. Reginski, and A. Kudla, *Physica B*, 2003, **340-342**, 1082.

[176] A. L. Gray, A. Stintz, K. J. Malloy, T. C. Newell, and L. F. Lester, *J. Crystal Growth*, 2001, **222**, 726.

[177] C. A. Wang, S. H. Groves, J. H. Reinold, and D. R. Calawa, *Journal of Electronic Materials*, 1993, **22**, 1365.

[178] T. K. Koo, O. Byungsung, Y. M. Yu, D. J. Kim, Y. D. Choi, J. W. Lee, M. Y. Yoon, P. Y. Yu, and T. W. Kang, *J. Appl. Phys.*, 2010, **108**, 113508.

[179] T. K. Sharma, R. Jangir, S. Porwal, R. Kumar, T. Ganguli, M. Zorn, U. Zeimer, F. Bugge, M. Weyers, and S. M. Oak, *Phy. Rev. B*, 2009, **80**, 165403.

[180] K. M. S. V. Bandara, J. W. Choe, M. H. Francombe, A. G. U. Perera, and Y. F. Lin, *Appl. Phys. Lett.*, 1992, **60**, 3022.

[181] B. F. Levine, *J. Appl. Phys.*, 1993, **74**, R1.

[182] D. Pan, E. Towe, and S. Kennerly, *Appl. Phys. Lett.*, 1998, **73**, 3706.

[183] H. J. Haugan, K. Mahalingam, G. J. Brown, W. C. Mitchel, B. Ullrich, L. Grazulis, S. Elhamri, J. C. Wickett, and D. W. Stokes, *J. Appl. Phys.*, 2006, **100**, 123110.

[184] P. Poloczek, G. Sek, J. Misiewicz, A. Löffler, J. P. Reithmaier, and A. Forchel, *J. Appl. Phys.*, 2006, **100**, 013503.

[185] T. K. Sharma, T. J. C. Hosea, S. J. Sweeney, and X. Tang, *J. Appl. Phys.*, 2008, **104**, 083109.

[186] T. Ivanov, V. Donchev, K. Germanova, P. F. Gomes, F. Iikawa, M. J. S. P. Brasil, and M. A. Cotta, *J. Appl. Phys.*, 2011, **110**, 064302.

[187] D. E. Aspens, *Handbook on Semiconductors*, Vol. 2, North-Holland, New York, 1980.

[188] Y. S. Huang, H. Qiang, F. H. Pollak, G. D. Pettit, P. D. Kirchner, J. M. Woodall, H. Stragier, and L. B. Sorensen, *J. Appl. Phys.*, 1991, **70**, 7537.

[189] A. Aierken, J. Riikonen, J. Sormunen, M. Sopanen, and H. Lipsanen, *Appl. Phys. Lett.*, 2006, **88**, 221112.

[190] C. R. Lu, J. R. Anderson, D. R. Stone, W. T. Beard, R. A. Wilson, T. F. Kuech, and S. L. Wright, *Phys. Rev. B*, 1991, **43**, 11791.

[191] I. H. Tan, G. L. Snider, L. D. Chang, and E. L. Hu, *J. Appl. Phys.*, 1990, **68**, 4071.